Induction heating of asphalt aggregate

Towards electrified industry and CO_2-neutral asphalt production

Induction heating of asphalt aggregate

Towards electrified industry and CO_2-neutral asphalt production

Dissertation

for the purpose of obtaining the degree of Master of Science in Sustainable Energy Technology
at Delft University of Technology
to be defended publicly on
Monday 16 September 2024 at 09:00

by

Herbert Van Even

Bachelor of Science in Mechanical Engineering, Delft University of Technology, The Netherlands
born in Turnhout, Belgium

CONTENTS

ABSTRACT

Heavy industry is responsible for about a third of global emissions but lags behind in its effort to become carbon neutral. The electrification of industrial processes is a necessary step to achieve this goal. The asphalt industry is a good candidate for decarbonisation, as it currently relies on burning fossil fuels to heat and dry the aggregate used in asphalt production. Instead, aggregates could be heated electrically by using induction heating.

This thesis will investigate the design of an aggregate induction drum heater. A COMSOL model will be developed to aid the design process and predict the heater behaviour. The heater will be powered by a resonant converter, which is modelled in Simulink. A test setup is built to serve as a proof-of-concept for the design and to experimentally verify the models.

The analysis of the simulation and test results show that the model quality is dependent on the description of the material properties. The COMSOL model predicts the temperature of the middle of the heater with reasonable accuracy while the Simulink model is able to simulate the coil current and converter voltage waveforms with little error. The design of the aggregate induction heater could be improved by thermally insulating the outside surface and increasing the contact area between the aggregate and the heater.

Acknowledgements

This research is based on earlier work by my supervisors Jianning Dong and Panos Apostolidis. Without their support and insight, this thesis would not have been possible.

In the construction and operation of the test setup, I was helped by Bart Roodenburg, whose enthusiasm and knowledge are much appreciated. Furthermore, I'd like to thank Hitesh Dialani and Guangyao Yu for their aid in making the PCBs and operating the lab equipment.

Finally, I'd like to thank my parents and sister for their unrelenting support, as well as Alvaro Detailleur, Amber van Groenestijn, Emma Steurs, Jef Winant and Tom Hendrix.

NOMENCLATURE

The next list describes several symbols that will be later used within the body of the document

δ	Skin depth
ϵ	Electric permittivity
ϵ_0	Electric permittivity of a vacuum
ϵ_r	Relative electric permittivity
η_h	Heater efficiency
η_{coil}	Coil efficiency
η_{con}	Power converter efficiency
$\hat{H}_e$	Amplitude of an alternating magnetic field
$\hat{I}$	Amplitude of alternating current
λ	Flux linkage
μ	Magnetic permeability
μ_0	Magnetic permeability of a vacuum
μ_r	Relative magnetic permeability
$\nabla\cdot$	Divergence
$\nabla\times$	Curl
∇T	Temperature gradient
∇	Gradient
ω	Angular frequency
∂	Partial derivative
Φ	Magnetic flux
ρ	Resistivity
θ	Volume charge density

$\vec{E}$	Electric field
$\vec{H}$	Magnetic field strength
$\vec{J}$	Displacement current density
$\vec{q}$	Heat flux by conduction
$\vec{u}$	Velocity of fluid flow
ξ	Ratio between wire diameter and skin depth
a	Diameter of tube heated by coil
A_L	Cross sectional area of an inductor
A_R	Cross sectional area of a conductor
B_{max}	Maximum magnetic flux density
bei_V	Imaginary part of Vth order Kelvin function
ber_V	Real part of Vth order Kelvin function
C_p	Specific heat capacity of a material
d	Wire diameter
d_a	Diameter of a strand of Litz wire
d_i	Diameter of a strand of Litz wire
f	Frequency
F_R	Parameter that represents the influence of the skin depth on skin effect losses
$F_{R,i}$	Parameter that represents the influence of the skin depth on skin effect losses based on the diameter of a strand of Litz wire
G_R	Parameter that represents the influence of the skin depth on proximity effect losses
$G_{R,i}$	Parameter that represents the influence of the skin depth on proximity effect losses in Litz wire
I	Current
I_c	Current in induction coil
I_e	Eddy current
j	Imaginary number
K	Empirically determined constant that is linearly proportional to the energy density of an object which is subject to hysteresis losses

k	Conduction coefficient of a material
K_{R2}	Correction factor to calculate equivalent resistance
L	Inductance
l_L	Length of an inductor
l_R	Length of a conductor
L_{air}	Inductance of an air core inductor
L_{iron}	Inductance of an iron core inductor
m	Empirically determined constant to calculate the energy density of an object which is subject to hysteresis losses
N	Number of turns of a coil
n	Number of strands in a Litz wire
P_c	Resistance losses in induction coil
P_P	Power generated by proximity effect losses
P_s	Power generated by skin effect losses
$P_{P,L,e}$	Power generated by proximity effect losses related to the external magnetic field in a Litz wire
$P_{P,L,i}$	Power generated by proximity effect losses related to the internal magnetic field in a Litz wire
$P_{P,L}$	Power generated by proximity effect losses in Litz wire
$P_{s,L}$	Power generated by skin effect losses in Litz wire
Q_E	Heat from eddy current losses
Q_E	Heat generated by eddy current losses
Q_M	Heat from hysteresis losses
Q_{net}	Net heat transfer per unit of volume
R	Resistance
R_c	Resistance of induction coil
R_w	Electrical resistance of a workpiece
$R_{DC,i}$	Resistance to direct current of a strand of Litz wire per unit length
R_{DC}	Resistance to direct current of the wire per unit length

R_{eq}	Equivalent resistance of induction heater
T	Temperature
V	Voltage
V_m	Volume of a magnetized object which is subject to hysteresis losses
w	Width of tube heated by coil
W_h	Energy density in a magnetized object which is subject to hysteresis losses

1

INTRODUCTION

Well, we can enjoy the view — as long as it lasts.

J. Robbert Oppenheimer

1.1. ELECTRIFICATION OF INDUSTRIAL PROCESSES

Man-made climate change will have disastrous consequences if it continues without interruption. The release of greenhouse gasses into the atmosphere from burning fossil fuels is the primary driver of climate change and therefore fossil fuels need to be replaced by renewable energy sources. This process is called the energy transition. There are three sectors which each constitute about a third of the total carbon emissions: electricity generation, transportation and industrial processes. The decarbonization of electricity generation and transportation have been the focus of the energy transition up to this point while decarbonization of industry has not received much attention. This reluctance to act poses a problem, since high capital costs in industry lead to a long lifetime for installed infrastructure, thereby enabling the *lock-in* of fossil fuel-based technologies for the coming 30 to 40 years [1]. However, the European Union (EU) and the current United States of America (US) presidential administration have created regulations, such as the EU Carbon pricing scheme, and frameworks, such as the European Green Deal and the Inflation Reduction Act, which have driven academics and industry players to accelerate the development of decarbonized industrial processes [2]. To this end, the U.S. Department of Energy has identified four technological pillars for industrial decarbonization [3]:

1. **Energy efficiency**; reducing the amount of energy needed for a certain industrial process.
2. **Low-carbon fuels, feedstocks, and energy sources**; Using low-carbon fuels and feedstocks reduces emissions from combustion in industrial processes.
3. **Carbon capture, utilization, and storage**; capturing carbon dioxide created by industrial processes and either re-using or storing it.

4. **Industrial electrification**; replacing fossil fuel heat sources with electrical alternatives, which can use sustainably generated electricity.

Industrial electrification shows strong potential because electrical heating covers the whole temperature and power spectrum that is required for industrial processes [1] [4]. Furthermore, electrification could reduce up to 78% of CO_2 emissions from EU industry [1]. However, electrification faces the challenges of unknown costs of electrical heating technologies relative to fossil fuel alternatives, high electricity costs and heterogeneous applications [4] [5]. Therefore, further research into electrical heating technologies for specific applications is required.

1.2. ASPHALT PRODUCTION

An application ripe for electrification is asphalt production. Asphalt is a ubiquitous building material used for roads, runways and parking lots. It is made from a mixture of aggregate, small pieces of hard and inert material such as rock, binder, often in the form of aggregate dust, and bitumen, a hydrocarbon that is an elastic solid at room temperature but becomes a very viscous liquid at higher temperatures. Bitumen is often referred to as asphalt, while the building material asphalt is also known as asphalt cement. In this thesis, however, the building material will always be referred to as asphalt and the hydrocarbon will be referred to as bitumen.

There exist two types of asphalt production plants: batch mix plants and drum mix plants.

The structure of a batch mix plant is shown in Figure 1.1. Bitumen is stored in tanks where it is heated to keep it in a liquid state. The aggregate is stored in well-constructed stockpiles, sometimes kept under a roof to protect it from moisture and often separated into coarse and fine variants. First, the aggregate is dried and heated in a drum, a long rotating metal drum that stands under a slight incline. Aggregate is dropped in at the highest end, making its way down the barrel while it is being lifted and dropped by flights, thin metal fins that longitudinally stretch the inside wall of the drum. A gas- or oil-fired burner blasts hot air up the tunnel, drying and heating the aggregate. In a parallel flow dryer, the burner is placed at the entrance of the drum and fires in the movement direction of the aggregate. In the more thermodynamically efficient counterflow dryer, the burner is placed at the outlet, blasting against the travel direction of the aggregate. Some of the aggregate dust is blown loose by the high-velocity combustion gasses. To ensure the fine dust particulates and toxic combustion products do not contaminate the plant and its environment, a fan is used to draw the dust, combustion gasses and water vapour into a filter. If too much dust is lost through filtration, the operators add more binder to the aggregate after the heating and drying are complete. Secondly, the dried and heated aggregate is then transported to the top of a mixing tower. Thirdly, the aggregate is dropped through a series of grids with shrinking holes, thereby separated into different grades and stored accordingly in tanks at the bottom of the tower. Finally, a certain composition of aggregate grades can be chosen and mixed

with the heated bitumen to get the desired asphalt mix. The hot asphalt is either transported directly to the work site or stored in heated silos at the plant.

A drum mix plant has the same first stage for drying and heating the aggregate. However, the drum dryer is extended to include a mixing compartment behind the burner. Here, hot bitumen is injected into the drum where it mixes with the heated aggregate. The separation of aggregate into different grades is done beforehand.

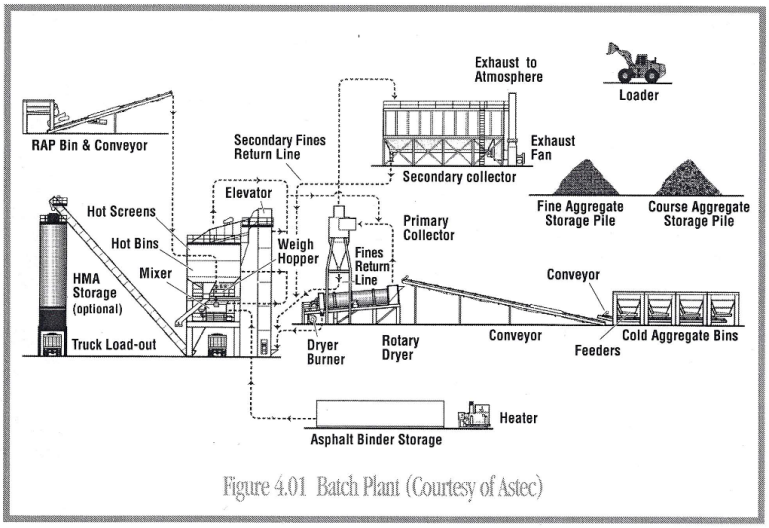

Figure 1.1: Schematic representation of asphalt production batch plant [6].

Batch plants are more common in Europe because they give more flexibility to change between different mix recipes [7]. On the other hand, drum mix plants have a smaller footprint, which is why they are often used for mobile asphalt production [6].

According to research by TNO and the Netherlands Environmental Assessment Agency, the three most energy-intensive production steps are heating the bitumen tanks, heating and drying the aggregate and heating the asphalt storage silos [7]. As can be seen in Table 1.1, heating and drying the asphalt consumes by far the most energy of these three steps at 71.39 kWh per tonne of asphalt produced. At the same time, this is the only step that can not yet be performed electrically. Therefore, there is an opening to replace the fossil fuel-fired drum dryer with an alternative that uses an electrical heat source.

Aggregate drying and heating is done to minimize the moisture content in the aggregate since the presence of water will prevent the stones from binding with the bitumen. Furthermore, a higher aggregate temperature will ensure the bitumen stays highly viscous, improving the mixing quality.

Electrifying the aggregate drying and heating process presents an opportunity to

1

Table 1.1: Average energy consumption (kWh/tonne asphalt mix) for the production of standard asphalt mix [7].

Process step	**Energy (kWh/tonne)**
Bitumen heating (electricity)	2.69
Drum heating and drying (fossil fuel)	71.39
Heated asphalt storage (electricity)	10.78
Total	84.86

alleviate design issues related to the burner. For starters, the hot combustion gasses may damage the filtering system which is needed to prevent the dust particulates of the aggregate from entering the air in great numbers [8]. Furthermore, if the bitumen is exposed to the burner exhaust gasses or the steam generated by the drying process, it can release smoke and volatile organic components which need to be filtered as well [9].

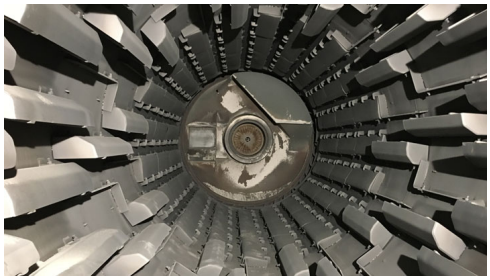

Figure 1.2: The inside of an aggregate drum heater and dryer. Note the flights along the drum wall which scoop up and drop the aggregate [10].

1.3. PROBLEM STATEMENT

The electrification of industrial processes is an important aspect of climate change mitigation. Processes that are ripe for this change need to be identified and specific techniques to electrify them need to be developed. Asphalt production presents an opportunity where electrifying the step of drying and heating the asphalt would result in near decarbonisation of the whole process. Therefore, the problem statement of this thesis is as follows:

> Developing a mechanical and electrical system to electrically dry and heat the aggregate used in the asphalt production process.

1.4. ELECTRICAL HEATING FOR INDUSTRIAL APPLICATIONS

This thesis concerns the use of induction heating for heating and drying asphalt aggregate. To substantiate the choice for induction heating, the most commonly used electrical heating techniques for industrial applications (resistance heating, microwave heating, infrared heating and induction heating) will be described briefly and the reasons for choosing induction heating will be highlighted. Each of these techniques is pictured in Figure 1.3 to provide a reference.

RESISTANCE HEATING

Resistance heating is the most basic electrical heating technique used in industry.

It is based on the fact that when electrical current runs through a wire, the power which is used to overcome the electrical resistance of the wire is converted into heat. When a conductor is specifically designed to generate heat through resistance losses, it is called a resistance heating element.

Different types of heaters can be designed by using this basic principle. A resistance furnace is a closed and thermally isolated chamber with heating resistors placed along the walls. The heat is transferred to the workpiece through convection and radiation. Some resistance furnaces are tunnels with a conveyor belt running through them, these are used to heat a continuous stream of feedstock [11]. An immersion heater consists of a heating element which is placed in a container for a liquid. The container is filled until the fluid completely submerges the heating elements. When the heater is turned on, the fluid fill starts to be heated through conduction and then begins to circulate as a consequence of convection, allowing all of the liquid to be heated. Electric water kettles use this design, as well as heated tanks for bitumen. [12] Contact heaters consist of a long strand of electrical wire which is flexible enough to be wrapped around objects which need to be heated. This technique is used to deice oil pipelines in cold regions. [13] Finally, direct resistance heaters are used to heat metal workpieces. A high electrical current is run through the workpiece and heat is generated in the object by overcoming its resistance, thereby heating it directly. This technique is often used for metalworking. [11]

Resistance heating profits from being simple and robust. Due to its straightforward underlying mathematics, it is easy to control. However, the conductor carrying the current must be large enough so it does not burn out when producing the heat. Other disadvantages are that resistance heating does not create a uniform heat distribution and that it can be inefficient because objects are often not heated directly.

Resistance heating is not well-suited for heating aggregates. Immersion heating and direct heating are not applicable since they concern different material types. Furthermore, heating aggregate in a continuous electrical furnace is possible, but this technology is designed for much higher temperatures than are required here. Finally, resistive contact heating could be used to heat a drum or container which carries the aggregates. However, this same design can be executed more efficiently through conduction.

MICROWAVE HEATING

Polar molecules are particles which are arranged in such a way that their ends have an opposite electric charge. When an electric field is present, the molecules will try to align themselves with it according to their polarity. By rapidly changing the direction of the electric field, one can cause the polar molecules to vibrate, constantly aligning and realigning themselves with the varying field. Through this mechanism, electromagnetic energy is converted into the kinetic energy of the particles, causing the object which the particles make up to increase in temperature.

The advantages of microwave heating are the high efficiency of energy conversion and the ease of control. Additionally, it can achieve high-temperature uniformity because an object is heated directly by exciting its particles and without the need for heat transfer through convection, conduction or radiation. However, some materials cannot be heated effectively with microwaves because of the simple fact that they do not contain (large amounts of) molecular dipoles.

Microwave heating has many practical applications. Microwaves can be found in almost every kitchen, using the dipole arrangement of H_2O molecules to heat any food item that contains water. The heating technique has also been studied for its potential to de-ice and self-heal asphalt. Self-healing is a technique in which asphalt is heated up and the bitumen becomes liquid again, filling the cracks which the pavement has acquired after years of vehicle loads and harsh weather conditions. [14] [15]

This research has shown that some stone aggregates such as limestone and quartz have low microwave heating susceptibility while others such as diorite and basalt are more susceptible. However, due to all rocks undergoing unique formation processes with their own peculiarities, susceptibility can vary within one material category and quantitative data is hard to come by. Metal aggregates such as steel slag have a higher microwave heating susceptibility but are (at the moment) not commonly used in asphalt production.

Although microwave heating has the advantages of high efficiency and high heating uniformity, the low microwave susceptibility of common stone construction materials makes it ill-suited for the heating and drying of aggregates in the asphalt production process.

INFRARED HEATING

All objects emit electromagnetic waves by their temperature. This energy is known as thermal radiation and consists of the infrared (IR), visible light and ultraviolet (UV) wavelengths. When an object absorbs thermal radiation, its temperature will increase.

Electric infrared heaters are built to exploit this phenomenon. They consist of a metal filament with a high electrical resistance and a high melting temperature through which a strong current is run. Due to the resistive losses, the filament becomes glowing hot, radiating visible light and infrared. A mirror which partially surrounds the filament helps project the infrared onto the workpiece, which absorbs the radiation and heats up. [20]

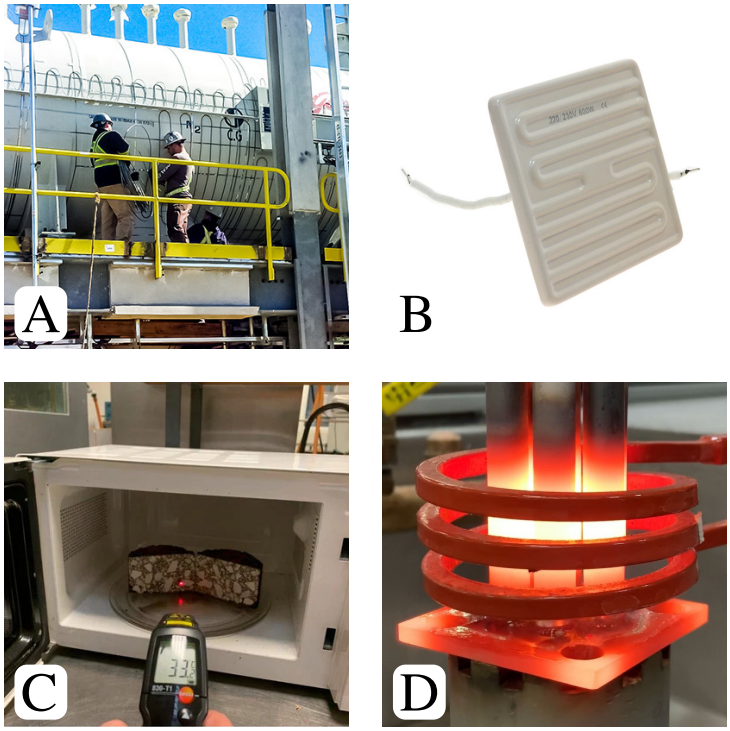

Figure 1.3: An overview of different electric heaters for industrial purposes. (A) Workers attach a resistance heating cable along the bottom side of a large industrial drum [16]. (B) A ceramic infrared heating panel [17]. (C) The temperature of an asphalt test sample is measured after it has been heated in a commercial microwave oven [18]. (D) Metal rods that have been heated by an induction coil to the point that they are glowing hot [19].

Alternatively, small strands of filament can be embedded in a ceramic material, heating the ceramic conductively with the resistive losses. In turn, the ceramic becomes glowing hot, shining radiation onto whatever objects need to be heated up. [21]

The advantages of infrared heating are that it does not heat the surroundings of the workpiece (air does not absorb thermal radiation), its efficiency and the uniform heating of the workpiece surface. The main disadvantage is that infrared heating is in practice a surface heating technique since the radiation does not penetrate beyond the top layer of the material. Furthermore, due to the extremely high temperature of the filament and the lack of environmental indications of the heating action, fire hazards and safety are of the utmost importance. [20] [22]

Infrared heating has been proposed as a heating and drying solution for reclaimed asphalt pavement (RAP), asphalt which has been scraped off the road and crushed

into small pieces to be reused in new asphalt mixtures. Since IR only heats the surfaces, the crushed asphalt must be arranged flatly. This is done by reusing the drum design, lining the inside wall with ceramic IR heating blocks and using a large screw to move the crushed asphalt over the infrared heaters, creating a shallow line which spirals along the inside of the drum. Therefore, IR heating can be used to heat aggregates if the heater is designed to arrange aggregates in a flat way [23].

Infrared heating could potentially be used to efficiently heat aggregates by making use of an inventive heater design. However, it will not be explored in this thesis because there was a greater research interest in induction heating.

INDUCTION HEATING

Induction heating is based on two fundamental principles of electromagnetics. First, a current running through a wire will create a magnetic field around it. This magnetic field is proportional to the strength of the current and its orientation is dependent on the current direction. Second, a conductor will develop an electrical potential difference if it is placed in a changing magnetic field. Therefore, if a metal object is placed close to a wire that carries an alternating current, the workpiece will develop a potential difference which drives a current in the workpiece that will heat it through resistance heating. Typically, the wire is wrapped into a coil to increase the strength of its magnetic field.

Any object made from a conducting material can be heated this way. Induction heating is best known to the general public as the heat source for induction cooking. Furthermore, it is used for a variety of industrial applications such as induction furnaces, inducting welding and heat treatment of workpieces.

The benefits of induction heating are its high efficiency, quick response time, consistency of its heating patterns and the availability of highly efficient solid-state converters which allow for the use of a large bandwidth of electrical frequencies. [20] However, induction heating is limited by its inability to heat non-conductive materials directly.

Induction heaters have been designed to heat and dry feedstocks for industrial purposes. [24] The design consists of a drum (such as the one used for heating asphalt) with a coil wrapped around it. The drum is heated by induction and in turn heats the material which flows through it. Some proponents of the technique have specifically envisioned it as a way to decarbonize the heating and drying process.[25] However, examples of induction heaters designed to heat construction materials are rare in the literature and this constitutes a research gap.

Induction heating has the advantages of high efficiency, consistent heating patterns and readily available solid-state converters. However, its disadvantage is that it cannot heat non-conductive materials directly. Induction heaters have been envisioned to replace fuel-powered heaters to heat and dry industrial materials, but there is a lack of research into to the design of induction heaters for use in industrial processes. This thesis aims to fill that research gap.

1.5. RESEARCH QUESTION

Induction heating is a possible solution for the problem of electrifying asphalt aggregate heating. This solution will be investigated based on the following research questions, scope and operational procedure.

1.5.1. RESEARCH QUESTION

Given that induction heating is the preferred method of electrical heating for this application, the goal of this report is to present a design procedure for an induction heater for asphalt aggregate. Therefore, the main research question of this thesis is as follows:

Main research question: What is a suitable mechanical and electrical design for an induction heater for asphalt aggregate that can be implemented in an existing asphalt production process?

To answer the main research question, several subquestions need to be tackled. Finding answers to the subquestions will lead to a solution for the main research question.

Subquestion 1: How can an induction heater for asphalt aggregate be modelled?

Subquestion 2: How can the model be experimentally verified?

1.5.2. SCOPE

The research scope is limited to the mechanical and electrical design of an induction heater for asphalt aggregate, the modelling of the heater and the design of a test setup to verify the quality of the model. Economic feasibility, safety considerations, environmental effects other than CO_2 emissions, and improvements on asphalt quality are not part of the scope. However, these subjects might be touched on in passing when they are relevant.

1.5.3. DESIGN AND TESTING PROCEDURE

To create and evaluate a design for an induction heater for asphalt aggregate, first, a general design will be made. Second, a model will be made to simulate the behaviour of the heater. Third, a scaled-down test setup will be built to verify the quality of the model. Finally, an optimal design will be created using the verified model.

1

1.6. THESIS OUTLINE

The physics of electromagnetism and heat transfer will be discussed in Chapter 2. Chapter 3 will discuss the design process 3, followed by Chapter 4 which lays out the models and model results. Chapter 5 discusses test setup and model verification and finally, Chapter 6 presents the thesis conclusions.

2

THEORETICAL ANALYSIS

This chapter will discuss the Theoretical background needed to model and design an induction heater for asphalt aggregates. In the first three sections, the physics of induction heating is discussed. Section 2.1 presents electromagnetic induction, the basic principle of induction heating. Section 2.2 follows up by explaining the two ways electromagnetic induction generates heat: through hysteresis and eddy currents. After the heat sources are discussed, Section 2.3 describes how this heat is transferred through an object. The remaining sections of this chapter discuss the additional Theoretical background needed to understand the modelling and design of an induction heater. Section 2.4 presents equations for the skin effect and proximity effect in wires. Following that, Section 2.5 explains the principle of a resonant power converter and the type of power converter used for induction heaters.

2.1. ELECTROMAGNETIC INDUCTION

Induction heaters work based on the principle of electromagnetic induction. This is a phenomenon where a time-varying electric current creates a magnetic field that changes in magnitude and direction in proportion to the current. When a conducting object, such as a steel cylinder, is placed in the changing magnetic field, an electric field will be induced in the object. This voltage in turn drives a current in the object. Because the object has some electrical resistance, there are power losses which get dissipated in the object as heat. The following subsections will discuss equations that are used to describe electromagnetic induction and will introduce physical concepts, such as magnetic permeability, that are necessary to understand the phenomenon fully. Finally, the design principles for inductors, electrical devices made to produce magnetic fields, are discussed.

2.1.1. MAXWELL'S EQUATIONS

Electromagnetic induction is described mathematically through Maxwell's equations and Ohm's law. Maxwell's equations are a collection of coupled partial differential

equations that describe the behaviour of electromagnetic fields, they are given below in phasor notation.

$$\nabla \cdot \vec{E} = \frac{\theta}{\epsilon} \tag{2.1a}$$

$$\nabla \cdot \vec{H} = 0 \tag{2.1b}$$

$$\nabla \times \vec{E} = -j\omega\mu\vec{H} \tag{2.1c}$$

$$\nabla \times \vec{H} = j\omega\epsilon\vec{E} + \vec{J} \tag{2.1d}$$

Equation 2.1a is Gauss's law, which states an electric field is created by the presence of electric charges. Here, $\nabla\cdot$ is the divergence, an operator indicating the flow of a vector field towards or away from a point. $\vec{E}$ is the electric field in V/m, θ is the volume charge density in C/m^3 and ϵ is the electric permittivity of the medium in which the electric field is present in F/m. Electric permittivity is a measure of how much material can be polarized by an electric field. Permittivity can be expressed as a function of the permittivity of a vacuum ϵ_0 through a value called the relative permittivity ϵ_r of the material. The corresponding Equation is $\epsilon = \epsilon_r\epsilon_0$. Because it is a scaling factor, ϵ_r is dimensionless.

Equation 2.1b is Gauss's law for magnetism, which states that the magnetic field lines coming into a surface must be equal to the magnetic field lines coming out of that surface. Here, $\vec{H}$ is the magnetic field strength in A/m.

Equation 2.1c is the Maxwell-Faraday law, which states that an electric potential is induced in an electrically conductive material when it is placed in a time-varying magnetic field. Here, $\nabla\times$ is the curl, an operator indicating the degree to which a vector field rotates around a certain point. $j\omega$ is the phasor notation for the derivative concerning time with ω being the angular frequency in rad/s. The angular frequency is related to the ordinary frequency f through the formula $\omega = 2\pi f$, with the unit of f being Hz or s^{-1}. j is the imaginary number. μ is the magnetic permeability in H/m, a measure of how easily a material is magnetized by an external magnetic field. Permeability can be expressed as the permeability of a vacuum μ_0 through a value called the relative permeability μ_r of the material. The corresponding Equation is $\mu = \mu_r\mu_0$. Like the relative permittivity, the relative permeability is dimensionless.

Equation 2.1d is the Maxwell-Ampere law, which states that a magnetic field is induced by a current or a time-varying electric field. Here, $\vec{J}$ is the displacement current density in A/m^2.

2.1.2. PERMEABILITY

Because of its importance to electromagnetic inductance, it is worth exploring the concept of permeability in depth. Anywhere a magnetic field $\vec{H}$ is present, it creates a magnetic flux density $\vec{B}$. However, the magnitude of this flux density differs for different materials placed in the magnetic field. An object made of wood or rubber

will have a much smaller flux density for the same magnetic field than an object made of iron or nickel. Magnetic permeability μ then, is the measure of how easily a material acquires magnetic flux density, i.e. how easily it is magnetised. This relationship is shown in Equation 2.2. The unit of $\vec{B}$ is Tesla or T.

$$\vec{B} = \mu \vec{H} \tag{2.2}$$

The value and behaviour of permeability differ strongly between materials. The permeability of empty space, of a vacuum, is $\mu_0 = 4\pi \times 10^{-7} H/m$. Since there is no matter in a vacuum that can be magnetized, this essentially comes down to a conversion of units between $\vec{H}$ and $\vec{B}$.

Some materials are paramagnetic, meaning they are weakly magnetised by an external magnetic field. Their permeability is constant and very close to μ_0.

On the other hand, ferromagnetic materials are metals which below a certain critical temperature T_c have a high permeability μ and develop a large flux density $\vec{B}$ when placed in an external magnetic field $\vec{H}$. However, the relationship between magnetic field and magnetic flux density for a ferromagnetic material is not constant. When increasing the external magnetic field in which a ferromagnetic object is placed, the magnetic flux density in the object will first rise slowly. Then the flux density will rapidly increase until it hits its limit and the flux density stops increasing, at this point the material is saturated.

Permeability is therefore a function of $\vec{H}$, $\mu = \mu(\vec{H})$. The non-linear relationship between an external magnetic field and the material's flux density is shown by a BH-curve. Figure 2.1 presents a generic BH-curve for a ferromagnetic material showcasing saturation. The derivative of the curve with respect to $\vec{H}$ is the permeability.

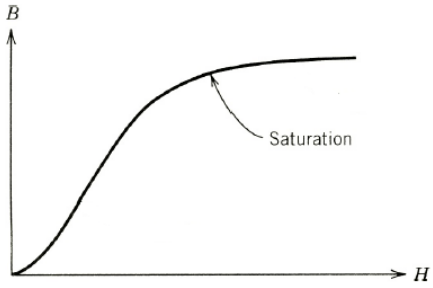

Figure 2.1: Generic BH-curve for a ferromagnetic material (after [26]).

In the middle region of the BH-curve, the function is nearly linear. Therefore, the permeability can be approximated as a constant. Iron is the most common component of ferromagnetic materials and has a relative permeability of 200000 [27]. Carbon steel, which is the material that is used for the induction heater discussed in this thesis, has a relative permeability of 100 to 400.

The magnetic saturation of a ferromagnetic object can be reversed by simply lowering the intensity of the external magnetic field $\vec{H}$. However, the B-field will decrease along the same path it increased. More specifically, it will decrease slowly at first and retain magnetic flux density even when the external magnetic field has dropped to zero. This phenomenon is called hysteresis and will be discussed further in section 2.2.1.

2.1.3. OHM'S LAW

Ohm's law states that the strength of the electric current in a medium relates proportionally to its voltage and inversely to its electrical resistance. Ohm's law is given below.

$$I = \frac{V}{R} \tag{2.3}$$

Equation 2.3 is the well-known formulation of Ohm's law. Here I is the current in A, V the voltage in V and R the electrical resistance in Ω.

The electrical resistance R of a conductor with a uniform cross-section is given by Equation 2.4.

$$R = \rho \frac{l_R}{A_R} \tag{2.4}$$

In the Equation above ρ is the resistivity of the material in Ωm, l_R is the length of the conductor (i.e. the length of the current path) in m and A_R is the cross-sectional area of the conductor m^2. It stands to reason that given a certain voltage, the generated current is smaller when the path it has to travel is longer. Additionally, it intuitively makes sense that current travelling through a larger cross-section encounters less resistance than current travelling to a smaller cross-section. Finally, resistivity ρ quantifies the inherent resistance of the material to electrical current. Conducting materials such as copper or silver have a low resistivity of $1.59 \times 10^{-8}\,\Omega m$ and $1.68 \times 10^{-8}\,\Omega m$ respectively, while insulators such as glass or Teflon have a high resistivity of $10^{11}\,\Omega m$ to $10^{15}\,\Omega m$ and $10^{23}\,\Omega m$ to $10^{25}\,\Omega m$ respectively.

Although Equation 2.4 is rudimentary, anyone who has completed high school physics will have encountered this formula, it is worth discussing here because it will be compared to the Equation for equivalent resistance R_{eq}, a concept used for calculating the heating power of induction heaters which will be introduced in Section 2.2.2.

2.1.4. INDUCTION

The phenomenon of induction is described by equations 2.1c, 2.1d and 2.4. When a current $\vec{J}$ is run through a wire, a magnetic field is created around that wire by Equation 2.1d. The strength of the magnetic field is proportional to the strength of the current. The wire is curled into a coil, and the magnetic fields around each loop will add up, creating a strong magnetic field running along the longitudinal axis of the coil. The magnetic field can be varied by simply changing the direction and

magnitude of current through the wire or coil. When a conducting object is then placed within a time-varying magnetic field, an electric field by Equation 2.1c will be induced in the material. Electromagnetic induction is thus the generation of an electric field through a varying magnetic field which was itself created by a varying current. Finally, the voltage drives microscopic circular currents called eddy currents in the conducting object, following Equation 2.4. Their name is derived from their circular current path, which is reminiscent of a whirlpool. An example of eddy currents is shown in Figure 2.2.

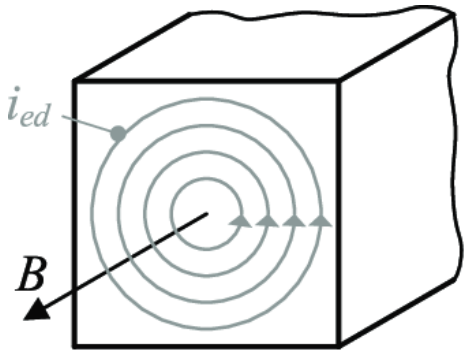

Figure 2.2: Eddy currents in a solid block of metal (after [28]).

2.1.5. INDUCTOR DESIGN

An electrical device that is designed to generate a magnetic field by running a current through it is called an inductor. As mentioned in the previous section the simplest type of inductor, called a solenoid, consists of a wire curled into a coil. The measure of how effectively an inductor creates a magnetic field is called its inductance L, which is defined as the generated flux linkage λ per unit of current I. Flux linkage is the magnetic flux produced by the inductor multiplied by the number of turns of the inductor. These relationships are shown in Equations 2.5a and 2.5b [26].

$$\lambda = N\Phi \tag{2.5a}$$

$$L = \frac{\lambda}{I} \tag{2.5b}$$

In equation 2.5a, N is the number of turns of the coil producing the magnetic field, which is dimensionless, λ is the flux linkage and Φ is the magnetic flux, both in Wb or Vs. In equation 2.5b, L is the inductance in H or Wb/A.

Based on definitions 2.5a and 2.5b, a simple expression for the inductance of a solenoid inductor can be derived, it is shown in Equation 2.6a. The inductance of a solenoid inductor can be improved by inserting a ferromagnetic core into the coil. As discussed in Subsection 2.1.2, ferromagnetic materials have a high relative

permeability μ_r. Because of this, the produced magnetic field will be higher and the flux lines will be closely bound to the core. The expression for the inductance of a solenoid with a solid, cylindrical ferromagnetic core is given by Equation 2.6b [29].

$$L_{air} = \frac{N^2 \mu_0 A_L}{l_L} \tag{2.6a}$$

$$L_{iron} = \frac{N^2 \mu_0 \mu_r A_L}{l_L} \tag{2.6b}$$

Here, N is again the number of turns of the coil, A_L is the cross-sectional area of the inductor in m^2 and l_L is the length of the inductor in m. L_{air} refers to the inductance of an inductor without a core, also known as an air core inductor, while L_{iron} refers to the inductance of an inductor with a ferromagnetic core. Although the induction heater design discussed in this thesis has a hollow core and therefore differs from the design described by Equation 2.6b, useful observations can still be made from these expressions. Firstly, using a core with a higher relative permeability will result in a higher inductance. Therefore, material choice is not trivial when designing an inductor. Secondly, the geometry of the solenoid influences its inductance. Inductance is quadratically proportional to the number of coil turns and linearly proportional to its intersectional area. At the same time, the inductance is inversely related to its length. A high but short coil with many tightly wound turns will therefore lead to a high inductance.

These expressions for inductance have multiple limitations. First of all, Equation 2.6b assumes a linear relationship between flux and current. In other words, it is presumed that the permeability of the material μ_r is constant with respect to the external magnetic field. However, as will be discussed in Section 2.2, the permeability of ferromagnetic materials is a function of the external magnetic field. Secondly, it is assumed that the leakage flux is negligible, which is almost always not the case [30]. Finally, these expressions assume that there are no eddy current and skin effect losses generated in the core. Since the goal of the inductance heater is to generate these losses, this assumption will not hold.

Based on these formulas, the air core inductance of the inductance heater discussed in this thesis is 149.17 μH while the steel core inductance is 99.60 mH.

2.2. ELECTROMAGNETIC HEAT SOURCES

Electromagnetic induction generates heat through 2 different mechanisms: (a) eddy currents and (b) hysteresis. First, this section will discuss hysteresis, the weakest of the two phenomena. While describing hysteresis, the concept of magnetic permeability will be investigated more in-depth. Following that, eddy currents are explained. Since they are the dominant mechanism for heat production, equations will be given to estimate the eddy current heating power based on the electrical properties of the circuit and the design of the coil and workpiece.

2.2.1. HYSTERESIS

When a material is repeatedly magnetised and demagnetised a phenomenon occurs known as hysteresis. Hysteresis causes power losses which get dissipated in the material as heat. This section will describe hysteresis and give basic equations to model the related heat generation.

It is assumed an unmagnetized ferromagnetic material is placed in a rising external magnetic field $\vec{H}$. The magnetic flux density $\vec{B}$ in the material would rise accordingly until saturation is reached. If the strength of the $\vec{H}$-field is now lowered, the $\vec{B}$-field will decrease along a different path. When the $\vec{H}$-field reaches zero there will be a residual flux density left in the magnetic material. If the $\vec{H}$-field is reversed until it reaches an equal but opposite value of what it was before, the $\vec{B}$-field will first drop to zero and then become negative. Increasing the $\vec{H}$-field again to its original positive value will increase the value of the $\vec{B}$-field along a different path until it reaches its maximum saturated value again. This phenomenon of the $\vec{B}$-field lagging behind the $\vec{H}$-field and following a different curve depending on the direction of the change in the $\vec{H}$-field is called hysteresis and the path it describes is called the hysteresis loop. A generic hysteresis loop is shown in Figure 2.3

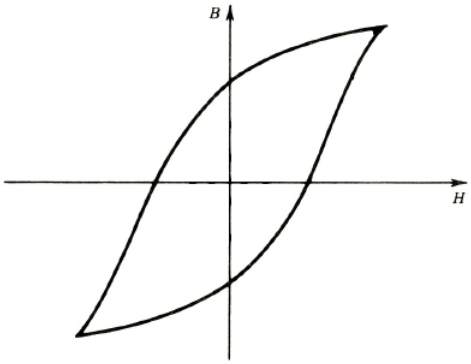

Figure 2.3: Generic hysteresis loop for a ferromagnetic material (after [26]).

When cycling through a hysteresis loop, energy is used to magnetize the core. However, more energy is absorbed than is given back. This power loss is dissipated as heat in the core. Its value is given by Equation 2.7.

$$Q_M = V_m W_h f \tag{2.7}$$

In the equation above, Q_M is the heat generated by hysteresis losses in W, V_m is the volume of the magnetized object in m^3, W_h is the energy density in the core in J/m^3, which is equal to area of the hysteresis loop in the BH-graph, and f is the frequency by which the $\vec{H}$-field is varied in Hz. The area of the hysteresis loop is difficult to calculate. Therefore it is often estimated by Equation 2.8.

$$W_h = K B_{max}^m \tag{2.8}$$

Here, B_{max} is the maximum flux density in T, while m and K are empirically determined constants. m is dimensionless, while K is in m/A

2.2.2. EDDY CURRENTS

Heat is generated by the electrical losses of the eddy currents. As previously explained, eddy currents are microscopic currents that are induced in a metal object by a changing magnetic field. The metal has some resistance and the power needed to overcome this resistance is dissipated as heat. This phenomenon, described in terms of the current density vector by Equation 2.9, is called the Joule effect. It is the main mechanism by which an induction heater generates heat.

$$Q_E = \int_V \frac{|\vec{J}|^2}{\sigma} dV \tag{2.9}$$

Here, Q_E is the heat dissipated by eddy current losses in W, $\int_V$ is the volume integral over the metal object, J is the current density of the eddy currents in A, and σ is the electrical conductivity of the metal in $1/\Omega m$. Conductivity is merely the inverse of resistivity ρ described in Section 2.1.3.

SKIN EFFECT

The eddy currents created by the induction voltage are concentrated near the surface of the metal object. This is because these currents, which are time-varying, generate their own magnetic field, which in turn induces a new voltage which tries to counteract the change in the current which created the magnetic field, a phenomenon known as Lenz's law. The new voltage pushes the currents away from the centre of the workpiece and towards its surface. The concentration of current density at the surface of an object is called the skin effect. It is seen in electrical wires as well as workpieces heated through induction heating. Skin effect is also present in wires carrying alternating current, this is discussed further in Section 2.4.

A common way to think of the skin effect in cylindrical workpieces is by imaging a cylinder that is divided into many concentric layers. A changing magnetic field in the cylinder will generate a current in the outer layer. This current will generate its magnetic field which counteracts the change in the external field. Because of this, the current generated in the second layer will be weaker than the current in the first layer. The same thing applies to the third layer and so forth until very little current is generated in the centre of the cylindrical workpiece.

Skin effect is a fundamental phenomenon of electromagnetic induction. Although the intensity of the effect will vary between situations, the principle that current density is the highest at the surface and decreases exponentially towards the centre will always hold. Since the current concentrates near the surface, the heat generation occurs there as well with the heat spreading to the rest of the object through conduction. Therefore, when investigating the heating power generated through induction it is useful to quantify the skin effect.

SKIN DEPTH

The intensity of the skin effect is indicated by the skin depth δ, this is the depth in m at which the current density equals $1/e$ times, or roughly 37%, the current density at the surface. The definition of skin depth is given by Equation 2.10.

$$\delta = \sqrt{\frac{\rho}{\pi \mu f}} \tag{2.10}$$

It can be seen that skin depth is dependent on two material properties. Firstly, it is proportional to the square root of the resistivity ρ. Secondly, it is inversely proportional to the square root of the magnetic permeability μ. It is intuitive that if a material can be magnetised more strongly, the counteracting effect of the induced magnetic fields will be stronger as well, thereby leading to a more intense skin effect. Since the resistivity and permeability of materials are given, a designer is limited in influencing this aspect of the induction heater. Finally, the skin depth is inversely proportional to the square root of the frequency f of the external field, and therefore the frequency of the induced currents. The constant π is included to convert between frequency f and angular frequency ω. Modern transistor-based electrical converters allow system designers to easily change the current's frequency, and thus change the skin depth, based on the needs of the application.

EQUIVALENT RESISTANCE

Now that skin depth is defined, a new concept can be introduced to model heating power for a hollow metal cylinder. The heating power that is developed in a workpiece can be quantified using the equivalent resistance R_{eq}. The equivalent resistance is hypothetical electrical resistance with such a value that if it were placed in series with the induction coil, it would dissipate as much heat as the eddy currents in the workpiece. In other words, it specifies how much heating power is produced in the workpiece for a given value of coil current. Like any electrical resistance, R_{eq} uses the unit Ω. For a tube, the equivalent resistance is given by Equation 2.11.

$$R_{eq} = N^2 \rho \frac{\pi a K_{R2}}{\delta w} \tag{2.11}$$

Equation 2.11 is similar in structure to the standard formulation for electrical resistance, given in Equation 2.4. Firstly, $\pi a K_{R2}$ is the analogue for the length of the current path. a is the tube diameter in m, meaning πa is the tube circumference in m. However, since eddy currents do not follow the circumference but circulate throughout the cross-section of the material, mostly staying within the skin depth, the dimensionless correction factor K_{R2} is introduced to give the representative current path length. For a tube K_{R2} depends on the ratio between the tube diameter and the skin depth a/δ, as well as on the ratio between the tube wall thickness and the tube diameter d/a. Values for K_{R2} for these parameters are shown in Figure 2.4. It can be seen that for tubes with thicker walls K_{R2}, and therefore the equivalent resistance, at first increases with an increasing skin depth but drops off after a

while. The correction factor tubes with thinner walls rise more slowly but peak later and only start decreasing again for very shallow skin depths. The decrease in K_{R2} happens because, at a certain point, the resistance of the workpiece becomes so high that the eddy currents are strongly inhibited and therefore power generation per unit of coil current becomes lower.

]

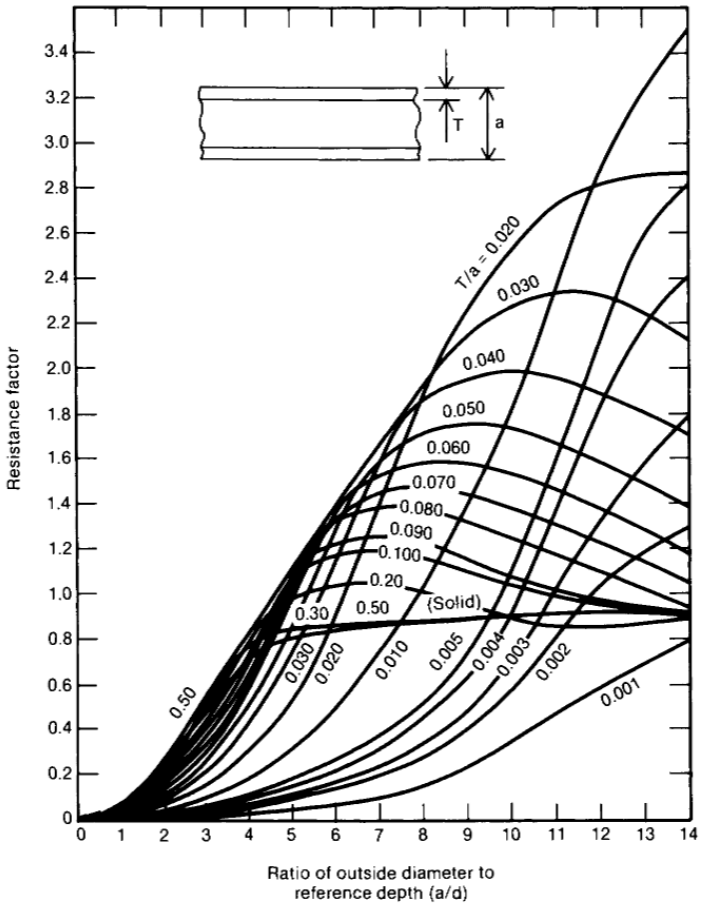

Figure 2.4: The resistance factor K_{R2} as a function of the ratio between the tube diameter and the skin depth. Different characteristics are given for different ratios between wall thickness and tube diameter. In general, the resistance factor becomes larger with increasing skin depth, after which it drops off.

Secondly, the product of skin depth δ and workpiece length w, which is given in m, in the denominator corresponds to the conductor cross-section area. A larger

skin depth and longer workpiece allow for more area for the current to flow through and therefore result in a lower equivalent resistance. Through the skin depth, R_{eq} is proportional to the square root of the material's permeability and the square root of the current frequency.

Thirdly, ρ is the resistivity of the workpiece material. However, since ρ is also present in the numerator of the equation for skin depth, R_{eq} is only proportional to the square root of ρ.

Finally, N refers to the number of coil windings. It might be counter-intuitive that the coil windings influence the equivalent resistance since they are not part of the workpiece. However, it is known that the magnetic field strength increases linearly with the number of turns. Therefore, the voltage and current induced in the workpiece both increase to the same degree. Since the heating power in the workpiece is the product of the induced voltage and current, the equivalent resistance is quadratically proportional to the number of coil turns.
Now that R_{eq} is defined and the parameters it depends on are understood, one can model the heating power of the coil and workpiece setup. At the same time, when the desired heating power is known, one can work backwards from Equation 2.11 to find a suitable heater design.

COIL EFFICIENCY

The quality of an induction heater design is not judged by its power generation alone. The induction heater should also be maximally efficient, using as little electrical power to produce as much heating power as possible. Using R_{eq}, the electrical efficiency of the induction heater can be defined, as shown in Equations 2.12a, 2.12b and 2.12c.

$$\eta_e = \frac{Q_E}{P_c + Q_E} \tag{2.12a}$$

$$\eta_e = \frac{I_c^2 R_{eq}}{I_c^2 R_c + I_c^2 R_{eq}} \tag{2.12b}$$

$$\eta_e = \frac{R_{eq}}{R_c + R_{eq}} \tag{2.12c}$$

In Equation 2.12a, Q_E refers to the heat generated by eddy current losses in the workpiece and P_c refers to the losses in the in the induction coil, both in W. The sum of these two equals the total electrical power input in the system. As shown in in Equation 2.12b, the efficiency can now rewritten in terms of coil current I_c, equivalent resistance R_{eq} and coil resistance R_c. By cancelling the I_c terms, it is found in Equation 2.12c that η_e is entirely a function of R_{eq} and R_c. Therefore, given a certain coil resistance, the efficiency can be improved by increasing the value of the equivalent resistance. R_{eq} is already defined by Equation 2.11, while the procedure to calculate R_c will be discussed in Section 2.4 [31] [32]. When heating

carbon steel, it is possible to reach very high efficiencies of more than 95% [33].

Figure 2.4 demonstrates that resistance factor K_{R2}, and therefore R_{eq}, is largest when the ratio between the tube diameter and the skin depth has a specific value. Since skin depth is defined by frequency, this means that there is a certain critical frequency f_c for which R_{eq} is maximized.

2.3. HEAT TRANSFER

The goal of the thesis is to design an inductively heated drum which can heat construction aggregate to the temperature which is appropriate for the manufacturing of asphalt.

To this end, the drum induction heater must be analyzed to determine the aggregate output temperature which results from a certain heat input, or the necessary power input to attain a certain aggregate output temperature. This analysis will be done by creating a thermodynamic model of the system: an accounting of the energy transfer between the heater and the aggregate. To perform this accounting the heat transfer mechanisms that are active in the drum need be to understood. Therefore, this section opens by describing the three fundamental heat transfer mechanisms: conduction, convection and radiation. Following that, the thermodynamic analysis is drawn up.

2.3.1. CONDUCTION

The temperature of an object is a measure of the kinetic energy of particles that make up the object. Molecules of cold solids lightly vibrate in place while the particles of hot gasses wildly shoot around at high speeds. Conduction is a heat transfer mechanism by which a particle with high kinetic energy (hot) bumps into a neighbouring particle with a lower kinetic energy (cold) thereby transferring some of its kinetic energy to the low-energy particle. The newly energized particle then bounces into the particles next to it and this chain reaction spreads the kinetic energy through the material. Conduction can take place in any type of material as well as on the border between 2 different materials.

Conduction in an object is proportional to the temperature difference across the object and the area of the material, while it is inversely proportional to the thickness of the object. Finally, conduction is dependent on the material of the object. Based on these relationships, the formula for one-dimensional conduction is given by Equation 2.13.

$$\dot{Q}_{cond,1} = kA\frac{\Delta T}{\Delta x} \tag{2.13}$$

Here, A is the area through which conduction takes place, ΔT is the temperature difference over the object and Δx is the thickness of the object. Finally, k is the conductivity of a material, this is a property which indicates the ability of the material to conduct heat. Materials with a high conductivity are good thermal conductors, while materials with a low conductivity are insulators. Conductivity varies with

temperature. The conductivity of steel decreases slightly at higher temperatures, while the conductivity of air increases significantly at higher temperatures. However, for most problems, it is sufficient to take the conductivity of the material at its average temperature.

For the purpose of the analysis, it is beneficial to use the derivative version of equation 2.13. Furthermore, this thesis will study objects whose temperature in real life varies in three dimensions, although this will be simplified to two dimensions to simplify calculations. The formulas for two-dimensional and three-dimensional heat conduction in cylindrical coordinates are given by Equations 2.14a and 2.14b.

$$\dot{\dot{Q}}_{cond,2} = k(A_r \frac{dT}{dr} + A_z \frac{dT}{dz}) \tag{2.14a}$$

$$\dot{\dot{Q}}_{cond,3} = k(A_r \frac{dT}{dr} + A_\varphi \frac{dT}{d\varphi} + A_z \frac{dT}{dz}) \tag{2.14b}$$

In Equation 2.14a, A_r is the area perpendicular to the r-direction and A_z is the area perpendicular to the z-direction. This equation is used for problems where it can be assumed that the temperature does not change with the angular position. In Equation 2.14b, A_φ is the area perpendicular to the angular direction.

Finally, conduction alone does not indicate how fast temperature propagates through an object. Some materials can absorb a lot of heat without undergoing a significant temperature increase, while other materials become hot very quickly after only a small increase in thermal energy. Thermal diffusivity α_{cond} is used to indicate how quickly heat spreads through a material, its formula is given by Equation 2.15. Heat spreads more quickly in materials with a large α_{cond}.

$$\alpha_{cond} = \frac{k}{\rho C_p} \tag{2.15}$$

ρC_p is the product of a material's specific heat and its density, known as the specific heat per unit volume in $\frac{J}{m^3 \cdot K}$. By dividing the conductivity of a material by its specific heat per unit volume, we find its thermal diffusivity.

2.3.2. CONVECTION

Convection is a method of heat transfer from an object to a flowing liquid or gas. Simply put, the heat from the object is conducted to a section of the fluid. Because of the movement of the fluid, the heated section flows along and a new cooler section of the fluid comes into contact with the object, gets heated through conduction and flows along as well, making space for a new cooler section still.

Convection can be split into two different types: forced convection and natural convection. In forced convection, the movement of the fluid is externally enforced, e.g. coolant being pumped through a hot car engine. In natural convection, the movement of the fluid is caused by the temperature difference between the hot object and the cool fluid (or vice versa). For example, a pastry taken out of the oven heats the air above it, which then rises due to its lower density and cold air rushes in to fill the space above the hot pastries.

The heat transferred through convection is proportional to the temperature difference and can be calculated from Equation 2.16, also known as Newton's law of cooling.

$$\dot{Q}_{conv} = h\, A_s\, (T_s - T_1) \tag{2.16}$$

Here, A_s is the heat transfer surface area, T_s is the temperature of the surface, T_0 is the temperature of the fluid moving over the surface and h is the heat transfer coefficient.
The heat transfer coefficient is different between cases of natural convection and forced convection and depends on many factors, including the material properties of the surface and fluid and the orientation of the surface. Due to the complexity of describing fluid flow, there are not many situations for which a formula for the heat transfer coefficient can be derived analytically. In most cases, the formula for the heat transfer coefficient is an empirical relationship found through experimentation. These empirical formulas can result in heat transfer coefficients that differ 10% or more from the actual value.

A common formula empirical for the heat transfer coefficient for natural convection depends on the relation between different dimensionless numbers. First, the relation between the heat transfer coefficient and the Nusselt number is given. This is followed by an investigation of the Nusselt number and a practical equation for the heat transfer coefficient of a horizontal cylinder undergoing natural convection.

First, the Nusselt number for a heat transfer problem is the ratio between the total heat transfer and the heat transfer by conduction. It is given by equation 2.17.

$$Nu = \frac{hL_c}{k} \iff h = \frac{kNu}{L_c} \tag{2.17}$$

Here, L_c is the characteristic length of the object undergoing convection.

This relationship means that if the Nusselt number is known, the heat transfer coefficient is known. As it turns out, the Nusselt number can be expressed as a function of a different dimensionless number: the Rayleigh number, or $Nu = f(Ra_L)$. The Rayleigh number is defined as the product of two different dimensionless numbers which are succinctly described below: the Grashof number and the Prandtl number.

The Grashof number is a dimensionless number that governs natural convection, given by Equation 2.18. It represents the ratio between two important fluid forces: the buoyancy force, the force that denser fluids exert on less dense objects or fluids in a gravitational field, and the viscous force, the force associated with the fluid's resistance to deformation. The buoyancy force drives natural convection while the viscous force decides the limits on fluid motion.

$$Gr_L = \frac{g\beta(T_s - T_0)L_c^3}{\nu^2} \tag{2.18}$$

Here, g is the gravitational constant, β is the fluid coefficient of volume expansion, T_s is the surface temperature of the object undergoing convection, T_0 is the ambient

temperature, L_c is the characteristic length of the object and ν is the kinematic viscosity of the fluid, or the viscosity corrected for inertial effects.

Another dimensionless number governing natural convection is the Prandtl number. The Prandtl number is the ratio between the diffusivity of momentum in a fluid and the diffusivity of heat in a fluid. Heat diffusivity α_{cond} was discussed before. Diffusivity of momentum is a measure of how easily momentum spreads in a fluid, in other words, how quickly the movement of particles in one section of the fluid influences the movement of particles in another section of the fluid. The formula for the Prandtl number is shown in Equation 2.19.

$$Pr = \frac{\nu}{\alpha} \tag{2.19}$$

Here, α_{cond} is the thermal diffusivity and ν is the kinematic viscosity of the fluid.

For a given problem, the Prandtl number and Grashof numbers can be found from known material and geometrical properties and thus the Rayleigh number can be calculated. Once the Rayleigh number is known the corresponding Nusselt number can be calculated. The relationship between Ra and Nu is empirically established and differs per geometry. The Nu-Ra relationship for natural convection with laminar flow over a horizontal cylinder is given by Equation 2.20.

$$Nu = (0.6 + \frac{0.387 Ra_d^{1/6}}{[1 + (0.559/Pr)^{9/16}]^{8/27}})^2 \tag{2.20}$$

The empirical nature of the equation is clear from the exponents, which are difficult to attribute any physical meaning to.

2.3.3. RADIATION

Thermal radiation refers to electromagnetic waves that are emitted by bodies as a result of the energy transitions of their particles. Other forms of electromagnetic radiation exist and although they can be highly energetic (e.g. X-rays contain much more energy than thermal radiation), they do not change the kinetic energy of particles and therefore they do not affect temperature.

Radiation is a volumetric phenomenon: all parts of an object, inside and outside, emit radiation. However, radiation originating from inside opaque objects does not reach the surface and radiation incident on opaque objects gets completely absorbed by the first few layers of particles. Since this thesis concerns opaque objects, for example, steel drums and crushed stones, the radiation discussed here is considered a surface phenomenon. Radiation from an object is therefore proportional to the surface area of that object. Next to temperature and area, the heat from radiation is dependent on the properties of the surface.

A blackbody is an object of an idealized material and idealized surface that emits the maximum possible amount of thermal radiation for a given area and temperature. However, real materials never emit this maximum amount of radiation, but instead some fraction of it. The heat rate from radiation is given by Equation 2.21.

$$\dot{Q}_{rad,ideal} = \epsilon_s \sigma A_s T_s^4 \tag{2.21}$$

Here, A_s is the surface area which emits radiation, T_s is the surface temperature, $\sigma = 5.67 \times 10^{-8}$ is the Stefan-Boltzmann constant, the constant of proportionality which relates temperature to radiation power, and ϵ is the emissivity, a measure of how much heat radiation the surface emits in comparison to a blackbody. The value of ϵ ranges from 0 to 1, with blackbodies having $\epsilon = 1$. ϵ is a surface property and depends on the material and the surface finish.

To properly describe radiation heat transfer, the effect of radiation striking a body needs to be discussed. When an opaque body is hit by thermal radiation, part of it is absorbed and part of it is reflected. Absorptivity α_{rad} is a measure of what fraction of the radiation incident on a body is absorbed and reflectivity ρ_{rad} is a measure of what fraction is reflected away. Since opaque bodies cannot transmit radiation, the Equation must hold.

$$\alpha_{rad} + \rho_{rad} = 1 \tag{2.22}$$

Modelling heat loss of the drum through radiation is not trivial, since the surfaces on which the radiation is incident will reflect part of that radiation to the drum. However, for small bodies that are surrounded by a large space, the heat loss formula is rather simple and given by Equation 2.23.

$$\dot{Q}_{rad} = A_s \sigma \epsilon_s (T_s^4 - T_0^4) \tag{2.23}$$

Here, T_0 is the ambient temperature of the surrounding space. Note that the heat transfer does not depend on the emissivity of the surrounding space. For this thesis, this simplification will be used to describe the heat lost in radiation by the drum to the outside world. This simplification has important shortcomings: the drum is surrounded by a coil, it is held in place by structural components and it is close to the ground. In actuality, the drum is not surrounded by an empty space. However, these shortcomings are accepted as modelling radiation heat transfer for complex geometries becomes difficult quite quickly.

2.3.4. INDUCTION HEATER AS THERMODYNAMIC SYSTEM

A thermodynamic model of the aggregate drum induction heater is created by using the principle of conservation of energy for an open system. It states that the change in the energy of the system is equal to the net energy being transported to the system by heat generation, by heat transfer and by mass transfer. Since heat problems deal more with power than with energy, it is convenient to use the rate form of conservation of energy which is shown by Equation 2.24a.

$$\dot{Q}_{in} - \dot{Q}_{out} + \dot{U}_{in} - \dot{U}_{out} + \dot{W} = \frac{dE}{dt} \tag{2.24a}$$

$$\dot{Q}_{in} - \dot{Q}_{out} + \sum_i \dot{m}_i C_p, i \Delta T_i + \dot{W} = \frac{dE}{dt} \tag{2.24b}$$

Here, $\dot{Q}_{in}$ is the heat into the system, $\dot{Q}_{out}$ is the heat out of the system, $\dot{U}_{in}$ is the internal energy of the mass entering the system, $\dot{U}_{out}$ is the internal energy of the mass exiting system and $\dot{W}$ is the heat generation; all of these quantities have unit W.

The change in internal energy of the mass which flows through the system happens through two mechanisms: change in temperature and change in phase. The change in internal energy that results from a change in temperature is calculated by $\dot{Q}_T = \dot{m}C_p\Delta T$. In this formula, $\dot{m}$ is the mass flow rate in kg/s, which is equal for the mass entering the system and the mass exiting the system, C_p is the specific heat of the material in $\frac{kJ}{kg \cdot K}$, a measure of how much energy is needed to increase 1 kg of a material by 1 degree Kelvin, and ΔT is the temperature difference between the material and the inlet and the material at the outlet in K. C_p is a function of temperature but to simplify calculations it is typically assumed to be constant. The heat associated with phase change is called latent heat, as it does not contribute to temperature rise. The formula for the heat absorbed or released by a flowing material which undergoes phase change is $\dot{Q}_L = \dot{m}C_L$, where C_L is the specific latent heat in $\frac{kJ}{kg}$. The change in internal energy then equates to $\Delta U = \dot{Q}_T + \dot{Q}_L$.

The evaporation of the aggregate's moisture content is an important aspect of the heating and drying process. However, the evaporation and the associated latent heat will be ignored when constructing a thermodynamic model to simplify the analysis and calculations. The impact of this simplification will be discussed in section 2.3.5.

If evaporation is ignored, the change in internal energy can be rewritten as a change in temperature for each mass flow through the system. The updated version of the first law is given by Equation 2.24b.

For a system at steady state, the energy of the system is constant and therefore its rate of change is equal to zero, as shown by Equation 2.25. Furthermore, in this thesis, the rate of heat transfer will be referred to as heat, with unit W.

$$\dot{Q}_{in} - \dot{Q}_{out} + \sum_i \dot{m}_i C_p, i\Delta T_i + \dot{W} = 0 \tag{2.25}$$

The principle of conservation of energy allows the engineer to draw up a power balance for a steady state system: an accounting of all power entering and leaving the system which in the end has to add up to zero.

GENERAL THERMODYNAMIC MODEL

To this end, the drum induction heater is divided into three control volumes and the power entering or leaving the volumes in the form of heat generation, heat flows or mass flows are accounted for, with the conversion of electrical energy into heat through induction being treated as heat generation.

A diagram of the model is shown in figure 2.5. The dark blue top and bottom layers are drum walls, the brown layer at the bottom of the drum is the aggregate and the light blue layer is the air inside the drum. These three sections also constitute the three different control volumes of the drum, for which the heat balances will be drawn up.

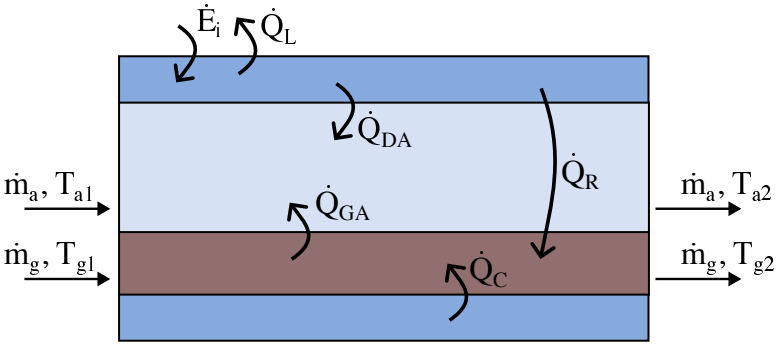

Figure 2.5: Heat balance of inductively heating asphalt aggregate in a drum.

In Figure 2.5 the aggregate stream with mass flow $\dot{m}_g$ enters the drum at temperature T_{g1} and leaves the drum at temperature T_{g2}, while the air moving through the drum has mass flow $\dot{m}_a$, inlet temperature T_{a1} and outlet temperature T_{a2}. The heat generated by induction in the drum wall is $\dot{W}_i$, the heat losses from the drum wall to the outside world by convection and radiation are $\dot{Q}_L$, the heat transferred from the drum to the aggregate by convection is $\dot{Q}_C$ and the heat transferred from the drum to the aggregate by radiation is $\dot{Q}_R$, finally, the heat losses from the aggregate to the air in the drum are $\dot{Q}_{GA}$ and the losses of the drum to the air inside it are $\dot{Q}_{DA}$.

The specific heat of the aggregate $C_{p,g}$ includes the specific heat of the dust and, depending on the level of simplification, can include the specific heat for liquid water.

Based on these control volumes, the heat balance for the drum is given by Equation 2.26a, the balance for the air is given by Equation 2.26c and the balance for the aggregate is given by Equation 2.26b.

$$\dot{W}_i - \dot{Q}_L - \dot{Q}_C - \dot{Q}_R - \dot{Q}_{DA} = 0 \tag{2.26a}$$

$$\dot{Q}_C + \dot{Q}_R - \dot{Q}_{GA} - \dot{m}_g C_{p,g}(T_{g2} - T_{g1}) = 0 \tag{2.26b}$$

$$\dot{Q}_{DA} + \dot{Q}_{GA} - \dot{m}_a C_{p,a}(T_{a2} - T_{a1}) = 0 \tag{2.26c}$$

The next paragraph will give a qualitative description of the heat streams in the system. $\dot{Q}_L$ consists of radiation and convection to the outside world. In the case of natural convection and moderate temperatures, the convective and radiative losses are usually of similar size. $\dot{Q}_C$ is the convection from the drum to the aggregate. Since the aggregates are fed into the drum by a conveyor belt and then pulled down by gravity, it can be seen as forced convection. It is the main heat transfer mechanism of the heater. $\dot{Q}_R$ is the thermal radiation from the drum to the aggregate. Since there is forced convection present, the share of heat transfer from radiation is typically negligible. Finally, $\dot{Q}_{DA}$ and $\dot{Q}_{GA}$ are convection from respectively the drum and aggregate to the air. In an industrial use drum heater, air

is blown through the drum at high speed by a fan to separate the aggregate dust from the aggregate, since the dust is detrimental to the binding of the aggregate and the bitumen. When air rushes through the drum at high speeds, the heat transfer by convection would be significant. However, in the lab setup which will be discussed later in the thesis, the air in the drum is not moved externally and the natural convection resulting from this is expected to be insignificant.

As part of this thesis, a test setup will be made for the drum. The thermal characteristics of the drum without aggregate will be measured and compared to simulation results. Referring to the model in Figure 2.5, this means that the aggregate layer and its related heat transfer phenomena are absent. Taking into account that the natural convection inside the drum is negligible, this results in $\dot{m}_a$, $\dot{m}_g$. $\dot{Q}_C$, $\dot{Q}_R$, $\dot{Q}_{DA}$ and $\dot{Q}_{GA}$ all being equal to zero. Now, only the drum control volume remains and the heat balances reduce to Equation 2.27a.

Using Equations 2.16 and 2.23 to model the heat loss to the environment, Equation 2.27b is obtained as a workable formula for the heat balance in the drum without aggregate.

$$\dot{W}_i - \dot{Q}_L = 0 \tag{2.27a}$$

$$\dot{W}_i - A_D h_D (T_{D,avg} - T_0) - A_D \epsilon_D (T_{D,avg}^4 - T_0^4) = 0 \tag{2.27b}$$

In Equation 2.27b, h_D is found by using Equation 2.20 for the Nusselt number of a horizontal cylinder in natural convection.

SIMPLIFIED THERMODYNAMIC MODELS

Later on in this thesis, a numerical analysis of the heat transfer will be done. To limit the calculation time of the numerical analysis, a simplified model of the aggregate drum induction heater is used. Instead of modelling the aggregate as a stream at the bottom of the drum, it is modelled as a layer which sticks to the inside circumference of the drum. Visually, it looks like a concentric cylinder which has an outside diameter equal to the inside diameter of the drum. The simplified model is shown in Figure 2.6.

As with any simplification, there is a trade-off between computational resources and model accuracy. Some of the heat transfer dynamics have changed. Specifically, there is no radiation from the drum to the aggregate and there is no convection from the drum to the air on the inside. These changes result in new heat balances for each control volumes, given for the drum, the air and the aggregate by respectively Equation 2.28a, Equation 2.28c and Equation 2.28b.

$$\dot{W}_i - \dot{Q}_L - \dot{Q}_C = 0 \tag{2.28a}$$

$$\dot{Q}_C - \dot{Q}_{GA} - \dot{m}_g C_{p,g} (T_{g2} - T_{g1}) = 0 \tag{2.28b}$$

$$\dot{Q}_{GA} - \dot{m}_a C_{p,a} (T_{a2} - T_{a1}) = 0 \tag{2.28c}$$

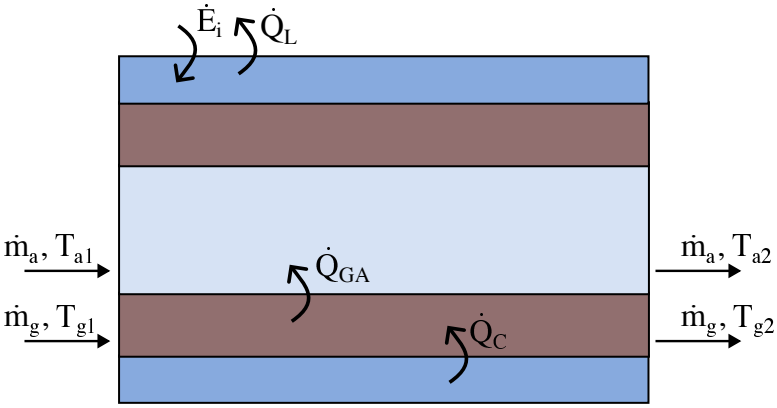

Figure 2.6: Heat balance of inductively heating asphalt aggregate in a drum based on a simplified model.

2.3.5. HEATING OF WATER

Although the drying of aggregates is an important function of the drum heater, the effects of the evaporation of water are simplified in this analysis.

The evaporation of water must be accounted for in two ways. Firstly, the latent heat which is absorbed by the water during evaporation. The value of the specific latent heat of water is $C_{L,w} = 2256 kJ/kg$. Secondly, the specific heat of water changes significantly between its liquid and its solid state. The specific heat of liquid water is $C_{p,w} = 4187 kJ/kgK$ while the specific heat of steam is $C_{p,s} = 1996 kJ/kgK$ [34].

To account for latent heat and the specific heat change between phases, the simplified specific heat for water $C'_{p,w}$ is defined by Equation 2.29.

$$C'_{p,w} = \frac{C_{p,w} \cdot (100°C - T_{g,1}) + C_{L,w} + C_{p,s} \cdot (T_{g,2} - 100°C)}{T_{g,2} - T_{g,1}} \tag{2.29}$$

Here, the moisture is assumed to have the same start and end temperature as the aggregate.

To include the heat necessary to increase the water temperature in the analysis, an enhanced aggregate specific heat $C'_{p,g}$ is defined through the moisture content X. Moisture content is the percentage of the aggregate mass flow which is taken up by moisture. It is defined by equation 2.30a while the enhanced specific heat of aggregate is defined by Equation 2.31.

$$X = \frac{\dot{m}_w}{\dot{m}_g} \tag{2.30a}$$

$$1 - X = \frac{\dot{m}_s}{\dot{m}_g} \tag{2.30b}$$

$$\dot{m}_g = \dot{m}_g + \dot{m}_s = X\dot{m}_g + (1 - X)\dot{m}_g \tag{2.30c}$$

$$C'_{p,g} = (1 - X) \cdot C_{p,g} + X \cdot C'_{p,w} \tag{2.31}$$

In Equation 2.30a, $\dot{m}_w$ is the mass flow of moisture while in Equation 2.30b $\dot{m}_s$ is the mass flow of solid particles.

In this thesis it is assumed that $T_{g,1} = 20°C$, $T_{g,2} = 180°C$, $C_{p,g} = 920$ and $X = 0.05$. This results in $C'_{p,w}$ = 3105.60 and $C'_{p,g}$ = 1029.3. Given that $C'_{p,g}$ is almost 10% higher than $C_{p,g}$, it is worth considering in the analysis.

2.3.6. TRANSIENT HEAT ANALYSIS

The previous paragraphs describe a thermodynamic analysis used for determining the thermal steady state of the drum heater. However, it is also useful to analyze the transient or time-varying state of the drum heater.

To analyze transient problems, the first law of thermodynamics as shown by Equation 2.24b is used. There, $\dot{U}$ is the change in internal energy over time, which corresponds to a change in the temperature of the mass in the control volume over time. Difficulty arises from the fact that the temperature is not constant throughout space and therefore $\dot{U}$ cannot be directly evaluated. This is solved by dividing the control volume into sufficiently smaller volumes which can be approximated to be of constant temperature with respect to space. For such a small volume of constant temperature with respect to space, the first law of thermodynamics is rewritten as Equation 2.32.

$$\dot{Q}_{in} - \dot{Q}_{out} + \dot{W} + \dot{m}C_p\Delta T = mC_p\frac{dT}{dt} \tag{2.32}$$

Here, $\frac{dT}{dt}$ is the derivative of temperature with respect to time. The above equation states that for a volume which has constant mass with respect to time and has constant temperature with respect to space, the heat transported by the volume heat transfer Q_in, heat generation E_i and mass transfer $\dot{m}C_p\Delta T$ will equal the losses Q_out and the change in temperature of the mass in time $mC_p\frac{dT}{dt}$. It is important to note that a volume of constant mass w.r.t. time can still be subject to mass transfer if $\dot{m}_{in} = \dot{m}_{out}$ and that ΔT is defined by the difference in temperature at the boundaries of the volume, while the temperature within the volume is constant w.r.t. space. For the control volume around a solid, $\dot{m}$ will be zero.

The numerical method which is discussed in Chapter 4 essentially uses this model to do a transient thermal simulation of the drum heater.

2.4. SKIN EFFECT AND PROXIMITY EFFECT IN WIRES

Alternating current that runs through a wire encounters a higher electrical resistance than direct current would. This is the case because the changing magnetic field that is created by the alternating current causes two physical phenomena that increase the resistance: the skin effect and the proximity effect. In this section, the skin effect and proximity effect will be explained. Since the skin effect was already discussed in section 2.2.2 to explain the behaviour of eddy currents in a metal workpiece, the

explanation in this section will be brief and focus on the manifestation of the skin effect wires. Furthermore, equations will be given to model the increase in resistance caused by these effects in both solid wires and Litz wires.

2.4.1. SKIN EFFECT IN SOLID WIRES

As explained in section 2.2.2, the skin effect is a phenomenon where an alternating current is concentrated in the outer layer of its conductor due to the voltage it generates. For a metal workpiece, the voltage is created by the alternating eddy currents (which were themselves induced by an external alternating magnetic field) that created this voltage, causing the eddy currents to be pushed away towards the outer layer of the workpiece and increasing the resistance of their current paths, allowing them to generate heat through electrical losses. Therefore, the skin effect is not a problem that needs to be overcome to improve the induction heating performance. It is instead the main mechanism through which induction heating is possible.

However, for an alternating current running through a copper wire, the skin effect is a problem. Because it causes the current to concentrate within the outer layer of the wire, the effective area of the wire becomes smaller and the effective resistance of the wire becomes larger. To calculate this increase in resistance it is necessary to know the skin depth. Since the relative permeability of copper μ_r is very nearly 1, the skin depth can be approximated as in Equation 2.33, which is a slight variation of Equation 2.10.

$$\delta = \sqrt{\frac{\rho}{\pi \mu_0 f}} \tag{2.33}$$

Further simplifying the skin effect, it is assumed that all the current is concentrated in an outer layer of thickness δ and has a constant current density. The skin effect losses can then be calculated as shown in Equation 2.34 [35].

$$P_s = R_{DC} \cdot F_R(f) \cdot \hat{I}^2 \tag{2.34}$$

Here, P_s is the skin effect loss per unit of wire length in W/m, R_{DC} is the DC resistance of the wires per unit length in Ω/m, $F_R(f)$ is a dimensionless factor to scale from the DC resistance to the AC resistance because of the skin effect, in effect $F_R(f) = R_{AC}/R_{DC}$, and $\hat{I}$ is the amplitude of the AC running through the wire. Since this ratio is dependent on the skin depth, F_R is a function of frequency f. For a round wire which has a diameter that is much smaller than its length, the formulas for R_{DC} and $F_R(f)$ are given in Equations 2.35a, 2.35b and 2.35c.

$$R_{DC} = \frac{4\rho}{\pi d^2} \tag{2.35a}$$

$$F_R = \frac{\xi}{4\sqrt{2}} \left(\frac{ber_0(\xi)bei_1(\xi) - ber_0(\xi)ber_1(\xi)}{ber_1(\xi)^2 + bei_1(\xi)^2} - \frac{bei_0(\xi)ber_1(\xi) + ber_0(\xi)bei_1(\xi)}{ber_1(\xi)^2 + bei_1(\xi)^2} \right) \tag{2.35b}$$

$$\xi = \frac{d}{\sqrt{2}\delta} \tag{2.35c}$$

R_{DC} is in accordance with Equation 2.4 and uses wire diameter d in m to calculate the cross sectional area of the conductor. Because the dimensionless term $F_R(f)$ scales R_{DC} to R_{AC}, it must take into account the relationship between wire diameter d (which defines the original conducting area) and the skin depth (which defines the new conductor area). The ratio between them, scaled by $\frac{1}{\sqrt{(2)}}$, is represented by ξ. Furthermore, ber_V and bei_V are Kelvin Functions, which are respectively the real and imaginary parts of the vth order Bessel function $J_V\left(xe^{\frac{3\pi i}{4}}\right)$. The equation for skin effect losses per unit length uses 0th and 1st order Kelvin functions. The derivation for $F_R(f)$ is beyond the scope of this thesis.

Because of the Kelvin functions, the influence of wire diameter and skin depth on the losses may not immediately clear from looking at Equations 2.34, 2.35a and 2.35b. However, if P_S is plotted as a function of d for a constant Î and f (and therefore a constant δ), it can be seen that the skin effect losses decrease with increasing wire diameter. This makes sense, because for a constant δ the effective conductor area still increases if the wire diameter d increases.

2.4.2. PROXIMITY EFFECT IN WIRES

The other loss mechanism specific to alternating current-carrying wires is the proximity effect, which will be explained using an example. Wire 1 carrying an alternating current lays parallel to wire 2, which also carries an alternating current. The current in wire 1 generates a time-varying magnetic field, which in turn induces eddy currents in the horizontal plane of wire 2. These eddy currents cause the current at one side of wire 2 to increase while the current on the other side of wire 2 to decrease, thus concentrating the total current in a specific spot in the cross-section of the wire. Because of this the effective area of the conductor decreases and the resistance increases.

The proximity effect is therefore similar in mechanism to the skin effect, with the difference being that the redistribution of current is caused by an external magnetic field instead of an internal magnetic field.

In a coil, the windings act as parallel wires. Although all windings carry the same current, each winding still has its magnetic field that acts on the other windings externally.

Equation 2.36 approximates the proximity effect losses per unit of length in a solid wire that is penetrated by an external magnetic field H_e [35].

$$P_P = R_{DC} \cdot G_R(f) \cdot \hat{H}_e^2 \tag{2.36}$$

Here, P_P are the proximity losses per unit of length in W/m and $\hat{H}_e$ is the amplitude of the alternating magnetic field in A/m. Since the eddy currents are linearly proportional to the changing magnetic field, they are represented by H_e. $G_R(f)$ is a dimensionless factor that represents the electric field and the DC resistance to the actual proximity effect losses. It takes into account the wire geometry and skin depth. $G_R(f)$ is shown in Equation 2.37.

$$G_R = \frac{\xi\pi^2 d^2}{2\sqrt{2}} \left(\frac{ber_2(\xi)ber_1(\xi) + ber_2(\xi)bei_1(\xi)}{ber_0(\xi)^2 + bei_0(\xi)^2} + \frac{bei_2(\xi)bei_1(\xi) - bei_2(\xi)ber_1(\xi)}{ber_0(\xi)^2 + bei_0(\xi)^2} \right) \quad (2.37)$$

$G_R(f)$ consists of Kelvin functions of the 0th, 1st and 2nd order. δ, R_{DC} and ξ are described by equations 2.33, 2.35a and 2.35c respectively.

Again, due to the Kelvin functions it is not obvious how the proximity effect changes with wire diameter. The proximity losses increase with increasing wire diameter. This makes sense intuitively since a larger wire diameter means the wire will have a stronger coupling with the external magnetic field, thus increasing the strength of the eddy currents.

2.4.3. SKIN EFFECT AND PROXIMITY EFFECT IN LITZ WIRES

The skin effect and proximity effect losses are very prominent in solid wires that operate at high frequencies. Litz wires are used to counteract these phenomena and minimize the losses. A Litz wire consists of a large number of small strands that are individually insulated and twisted in a helical pattern to form a bundle. A bundle can serve as a Litz wire in and of itself, or multiple bundles can be again twisted together into a larger wire. Figure 2.7 pictures a Litz wire which consists of multiple bundles.

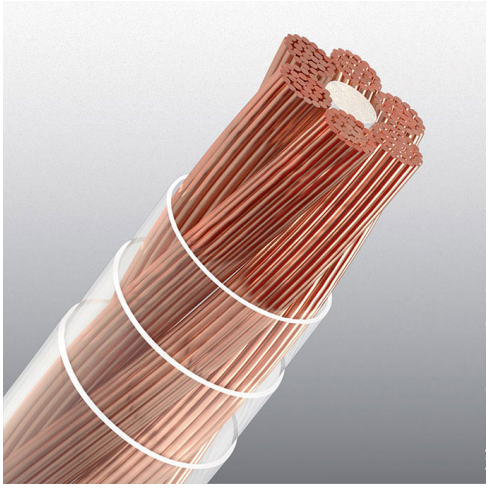

Figure 2.7: Litz wire with a transparent sheath. The strands are twisted into bundles according to a specific pattern. Multiple bundles are woven together to form the wire. [36]

A Litz wire diminishes the influence of the skin effect and the proximity effect in two ways. Firstly, because the skin effect applies individually to each strand, its effect will be much weaker if the strand diameter is close to or smaller than one skin depth. In that case, the effective area of the strand will stay practically unchanged.

Secondly, all the strands are twisted in such a way that to move from the centre of the wire to the exterior back to the centre. This is done because strands in the centre experience stronger changes in the magnetic field than the strands on the outside, which causes the strands in the centre to have a higher resistance. By making each strand move through the centre for the same length, the resistance of all strands is the same ensuring an equal current distribution.

For the skin effect losses in Litz wires, Equation 2.34 is adapted into Equation 2.38b [35].

$$P_{S,L} = n \cdot R_{DC,i} \cdot F_{R,i}(f) \cdot \left(\frac{\hat{I}}{n}\right)^2 \tag{2.38a}$$

$$R_{DC,i} = \frac{4\rho}{\pi d_i^2} \tag{2.38b}$$

For this adapted equation, n refers to the number of strands and d_i refers to strand diameter in m. The dimensionless parameters $F_{R,i}(f)$ and ξ_i are calculated by using Equations 2.35b and 2.35c respectively, only substituting d for d_i. By studying Equation 2.38b, it can be seen that increasing the number of strands and decreasing the strand diameter decreases the skin effect losses per unit length. This makes sense because as explained above the skin depth will take up a larger part of the strand cross section.

For the proximity effect losses in Litz wires, Equation 2.36 is adapted into Equation 2.39.

$$P_{P,L} = P_{P,L,e} + P_{P,L,i} = n \cdot R_{DC,i} \cdot G_{R,i}(f) \cdot \left(\hat{H}_e^2 + \frac{\hat{I}^2}{2\pi^2 d_a^2}\right) \tag{2.39}$$

As explained earlier, the proximity effect is a consequence of the wires being exposed to a changing magnetic field. However, since a Litz wire consists of many strands, to calculate the effect on one strand both the external magnetic field produced by the other strands $\hat{H}_e^2$ as the internal magnetic field of the one strand $\frac{\hat{I}^2}{2\pi^2 d_a^2}$ should be taken into account. The power losses related to the external magnetic field and the internal magnetic field are respectively written as $P_{P,L,e}$ and $P_{P,L,i}$, both given in W/m. Finally, $G_{R,i}$ is calculated as 2.37 but using the strand diameter instead of the wire diameter.

2.5. RESONANT CONVERTER

The resonant heating of steel workpieces such as the drum requires alternating current with frequencies in the 10 kHz range. However, the European mains power is 50 Hz. Therefore, an inverter is needed to generate an alternating current with a higher frequency. To this end, the resonant H-bridge converter is used.

This section will first explain the mechanisms of a series resonant circuit. Both the series LC circuit and the series RLC circuit will be described. Secondly, these concepts are used to study the working of a resonant converter and the predicted current and voltage waveforms are shown.

2.5.1. SERIES RESONANT CIRCUIT

A resonant circuit is a circuit that contains a capacitor and an inductor that exchange energy and together create a sustained alternating current with a resonant frequency f_r. This is the frequency at which the impedance of the capacitor and the inductor cancel each other out. The idealized circuit which only consists of an inductor and a capacitor is called an LC circuit. However, since all circuits contain some electrical resistance, some energy is lost and if the circuit is not fed by an external power source the alternating current will slowly decay until all the energy is dissipated in the resistor. This circuit which includes a resistance is called an RLC circuit and it is shown in Figure 2.8.

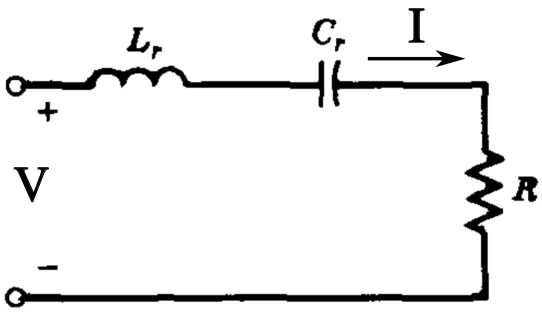

Figure 2.8: RLC series resonant circuit. [30]

The series LC circuit is analyzed to explain the principle of resonance. A charged capacitor with a capacitance C and a voltage v_c is placed in series with an inductor with inductance L. In this example, the current at the start of the experiment is assumed to be zero, $i_L = 0$. Because the circuit is closed, the capacitor will start to discharge and current i_L will flow in the circuit. The current will cause the inductor to generate a changing magnetic field that is proportional to the current. The magnetic field in turn induces a voltage in the inductor that opposes change of the current direction, thereby adhering to Lenz's law. At first, when i_L starts to flow, the inductor voltage is opposite to the capacitor voltage, slowing the current rise. Because the current rises more slowly, the inductor voltage itself starts dropping and becomes zero once the current has reached its peak and the capacitor is completely discharged. After the current has reached its peak and starts to fall, the inductor voltage will reverse, now driving the current to keep going in the same direction it was before. The current, kept going by the reversal of the inductor voltage, recharges the capacitor with opposite polarization. As the capacitor recharges, the inductor voltage decreases, and once the capacitor is fully recharged the cycle can begin anew. The waveforms are shown without magnitude in Figure 2.9.

After an initial transient period, the current and voltage of the circuit will naturally achieve its resonance frequency f_r. At the resonance frequency, the impedance of the inductor and the capacitor cancel each other out. This leads to the definition for

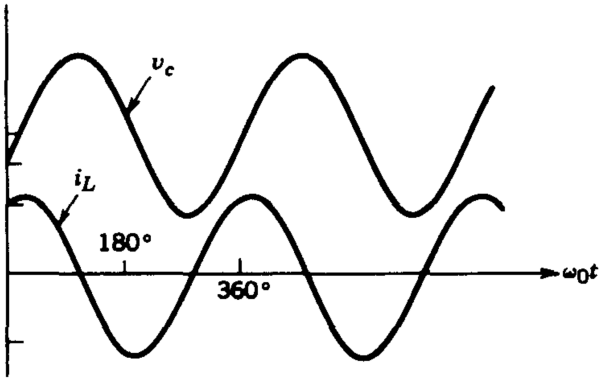

Figure 2.9: Generic waveforms for inductor current and capacitor voltage in a resonant circuit. Note how the waveforms are perfect sinusoids. [30]

resonance frequency shown in Equation 2.40.

$$\omega_r = 2\pi f_r = \frac{1}{\sqrt{L_r C_r}} \tag{2.40}$$

Here, ω_r is the angular resonant frequency, f_r is the resonant frequency, L_r is the inductance in the resonant circuit and C_r is the capacitance in the resonant circuit. The definition of resonant frequency in Equation 2.40 applies to LC circuits and RLC circuits.

2.5.2. SERIES RESONANT CONVERTER FOR INDUCTION HEATING

An inverter is a power converter which takes a direct current as input and delivers an alternating current as output. Modern inverters typically consist of an array of solid-state switches such as MOSFETs. These switches turn on and off in specific patterns to create an alternating current. When a switch turns off, the current through it will drop to zero while the voltage that stands over it will rise to a higher constant value. However, these changes in current and voltage do not happen instantaneously and there is a short time during which both the current and the voltage are high, leading to a small loss of power in the switch. When switches turn on and off at high frequencies, these losses add up to a significant power which heats the switch, potentially damaging it, and results in inefficiency. To reduce the losses, one should change the state of the switch when the current through the switch is zero. Because resonant circuits naturally produce sinusoidal currents which fall to zero at specific intervals, they are used to build such a low-loss inverter.

A series resonant inverter consists of an H-bridge and series resonant circuit as shown in Figure 2.10. The H-bridge is connected to a constant voltage power supply and creates a voltage square wave by opening and closing the diagonally positioned switches. This voltage square wave stands over the induction heater and a capacitor bank, which together can be described as a series RLC circuit. The resistor in this

circuit does not only represent the coil resistance but also the equivalent resistance of the heating action. By opening and closing the switches in the H-bridge at the resonant frequency of the circuit, the switching losses are minimized and a sinusoidal current is achieved. A resonant converter based on an H-bridge is also called a full-bridge converter, while a resonant converter based on two switches is called a half-bridge converter. Half-bridge converters are preferable for applications that require a small footprint and low cost, while full-bridge converters are used for applications which need high power and better control.

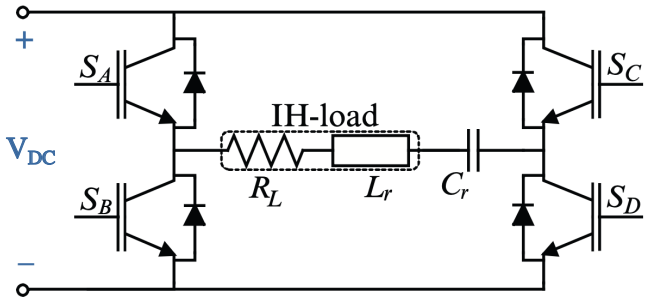

Figure 2.10: Full-bridge resonant converter.

In practical situations, the resonant frequency of a circuit can be calculated by measuring the values of the capacitor and the inductor and applying Equation 2.40. This frequency can then be used as the switching frequency of the circuit. However, it is difficult for the switching frequency to exactly match the resonant frequency because of measurement errors or because the capacitance and inductance change when the components are under operating conditions. When the switching frequency is higher than the resonant frequency, the current wave will be interrupted before it reaches zero at the end of its half-period, resulting in a piecewise pattern of partially complete sine waves as shown in Figure 2.11. Such a wave can be described mathematically by a recurrence relation system, although mathematical analysis of the electrical waveforms is outside the scope of this thesis. [37]

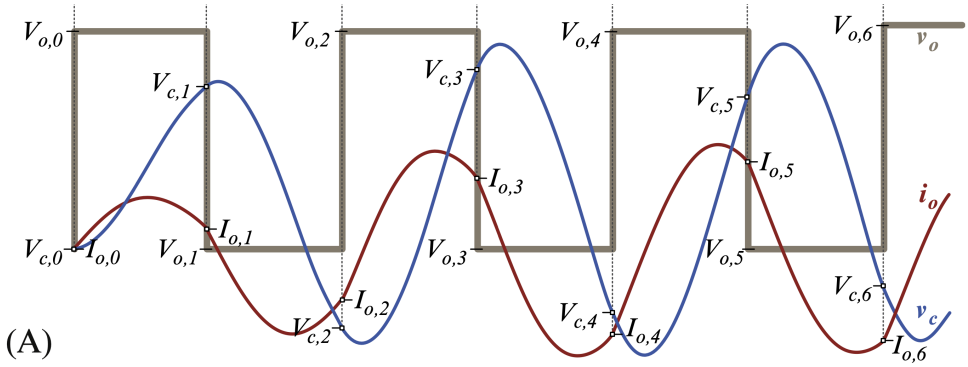

Figure 2.11: Electrical waveforms for a resonant converter in which the switching frequency is higher than the natural frequency. Coil current i_o consists of pieces of incomplete sinewaves. Furthermore, capacitor voltage V_c and switch voltage V_o are pictured. Note that the graph depicts the transition from transient state to steady state behaviour. [37]

3

DESIGN

The goal of this thesis is to come up with the design of an induction heater, create a model of it, and validate the model by designing and testing a scaled-down setup. This chapter discusses the general design of the induction heater and the specific design of the test setup.

First, the gas-fired heater is discussed. This serves as the basis for the induction heater design. Once the general design of the induction heater is presented, the design process for the test setup is laid out. The design process consists of defining the design criteria (which also reflect the criteria for a full-sized heater), a parameter investigation, and a parameter space search. Finally, the test setup design is present.

It is worth noting that not all aspects of the drum heater will be accounted for in this analysis. Specifically, the filtering of aggregate dust and the steam from the evaporated moisture is not part of the design, and neither are any adaptions for the use of reclaimed asphalt aggregate. Only the heating itself will be considered.

3.1. GAS-FIRED HEATER DESIGN

A heater should be designed to maximize the efficiency of the heat exchange between the source and the material. In the standard asphalt production process described in Section 1.2, aggregate is heated and dried by burning oil or gas in a rotating drum and moving the aggregate along the length of the flame. It is heated directly through radiation from the flame and through convection from the hot gasses produced by the combustion. The drum keeps the combustion confined to the space where the aggregate is, making it more efficient than an open-air flame. Furthermore, the drum is equipped with flights, metal fins running along the drum wall that scoop up the aggregate and drop it once they reach the top of the circle. When the aggregate falls it forms a curtain along the middle of the drum where the radiation and convection are the strongest, therefore improving the heat exchange between the combustion and the aggregate. The goal of this design is to maximize the time the aggregate spends in the middle of the drum where the heat exchange effects are the strongest. Over the years, variations on this basic design have been patented to increase the time the aggregate spends in the flame or to direct the heat

from the flame more efficiently to the surface of the drum where the aggregate lays.

Common values for the dimensions of the gas-fired drum heater and for the process variables of the heating and drying process are given in Table 3.1. The last column lists the reference values which will be used throughout the rest of the thesis.

Table 3.1: Reference values for the geometric and process variables of a gas-fired drum heater. [38]

Variable	Range	Reference
Drum diameter (m)	1.5 to 3	2
Drum length (m)	6 to 12	10
Output (tonne/h)	40 - 320	300
Inlet temperature (°C)	0 - 35	20
Outlet temperature (°C)	150 - 200	180
Moisture content in (%)	1 - 7	5

3.2. INDUCTION HEATER DESIGN

For the induction heater, the heat exchange mechanism is conduction between the inductively heated metal and the flowing granular aggregate. Since this is conduction with bulk fluid motion, it can be described as convection.

Either as conduction or convection, the heat transfer to the aggregate happens through contact with the metal, and therefore the time spent in direct contact with the metal should be maximized.

The principle of maximizing contact time holds when heating metals directly, the electromagnetic losses in the surface of the metal act as a heat source from which the inside of the metal is heated through induction, as well as when heating a non-metal in a metal container, e.g. when heating soup on an induction stove the pot is heated directly and this heat is transferred to the soup through conduction. Since conduction is dependent on surface area contact between the heat source and the material, an aggregate induction heater should be designed such that the contact between the heated metal and the aggregate is maximized. Additional design requirements are that the heater should be easily implemented in the complete asphalt production process, the leakage flux between the coil and metal should be minimized, the discharge rate of the aggregate should be controllable, the design should be simulated at relatively low computational cost and the design should interface well with the research previously done at this university. A diagram of this design is shown in Figure 3.1.

It is intuitive to transform the standard design for a fired aggregate heater into an induction aggregate heater by removing the burner and adding a coil around the outside of the drum. The drum wall is then heated through induction which in turn heats the aggregate via conduction. There are several obvious limitations to this design.

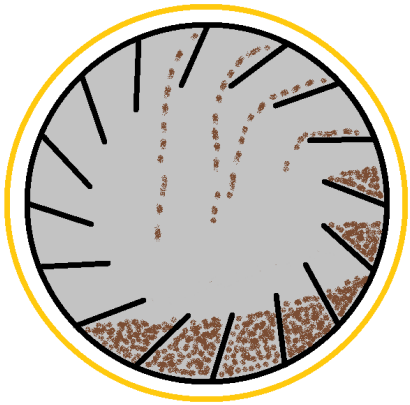

Figure 3.1: Standard aggregate heater design. The coil is shown as a gold ring around the drum. The flights pick up the aggregate and drop it once they reach the top. The aggregate curtains out over the middle of the drum.

Firstly, in a drum without flights, the aggregate will travel only along the bottom of the drum and thus most of the drum wall area is not used for heat exchange leading to low efficiency.

Secondly, the aggregate will pile up, with the aggregate towards the middle and the top of the heap receiving much less heat than the aggregate close to the wall. Even in a drum with flights, the aggregate uses at most half of the available area for heating and is dropped through the middle of the drum where it is only heated by radiation from the inside surface. T

his design can be improved by separating the drum into different compartments along the circumference and leaving a hollow space in the middle. These compartments provide more surface area for the aggregate to come into contact with and be heated through. Furthermore, a coil can be run both outside the drum and through a hollow space inside the drum, increasing the area that is actively heated. A diagram of this design is shown in Figure 3.2.

Finally, a different design can be conceived by drawing inspiration from induction cooking. The heater consists of a wide and flat rectangular metal bin that stands under a slight inclination. Flat spiral coils are placed directly under the bin to heat the bottom surface, similar to how an induction cooking pot is heated. Aggregate is inserted in an opening at the top of the bin, is heated up as it rolls down, and comes out the other end. The path of the aggregate may be obstructed with small metal fins to increase surface area contact and slow down the aggregate, giving it more time to heat up. The bin could be moved up and down to further control the aggregate travelling speed, operating the heater as an inclined vibrating screen. A diagram of the design can be seen in Figure 3.3. This design ensures good surface area contact between the aggregate and the heated metal. Furthermore, the discharge rate is controllable and due to its simple shape it could be integrated into the current asphalt production process without many problems. Finally, the design

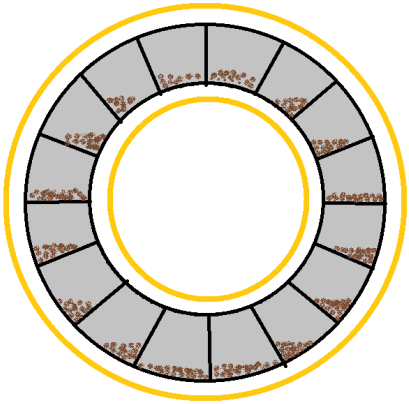

Figure 3.2: Aggregate heater with a ring of compartments. Two coils run along the outside and the inside of the drum respectively. The compartments allow for the aggregate to be heated maximally through conduction from the heated drum surface.

would have low leakage flux. However, this design would have to be simulated using a three-dimensional model and does not have any previous research associated with it. These last two points make it unattractive from a research perspective.

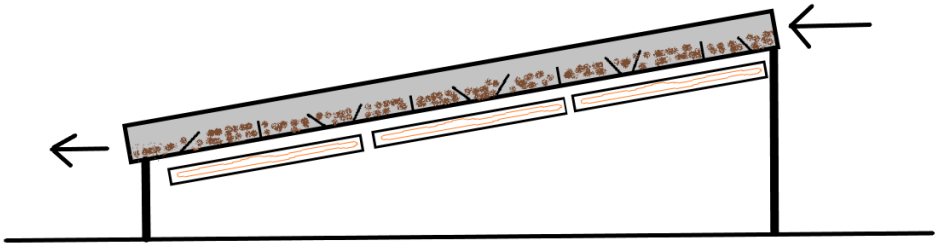

Figure 3.3: Tray aggregate heater design. Flat spiral coils can be seen under the inclined tray.

Because of its simplicity in modelling as well as building a test setup, and continuity with previous research, the simple drum design without flights or compartments is chosen.

3.2.1. DESIGN GEOMETRY

Figure 3.4 displays a stylized diagram of the induction heater. The geometrical properties of the induction heater are shown in the diagram. The steel drum, shown in blue, has length l_d, diameter d_d and wall thickness z_d. The copper coil that surrounds the drum, shown in orange, has wire diameter d_w, coil length l_c, and pitch p. The distance between the centre of the coil wire and the outside surface of the drum is z_h. The aggregate is shown as a layer that sticks to the drum wall because it is modelled as such in the COMSOL model, which will be discussed in detail in Chapter 4. The aggregate layer has thickness z_a. The front face of the aggregate cylinder is shown in brown, while its inside surface is shown in taupe. The aggregate moves with flow velocity v_a in m/s. Finally, a current of strength I_c in A flows through the coil, inducing a magnetic field. All geometrical dimensions are in m.

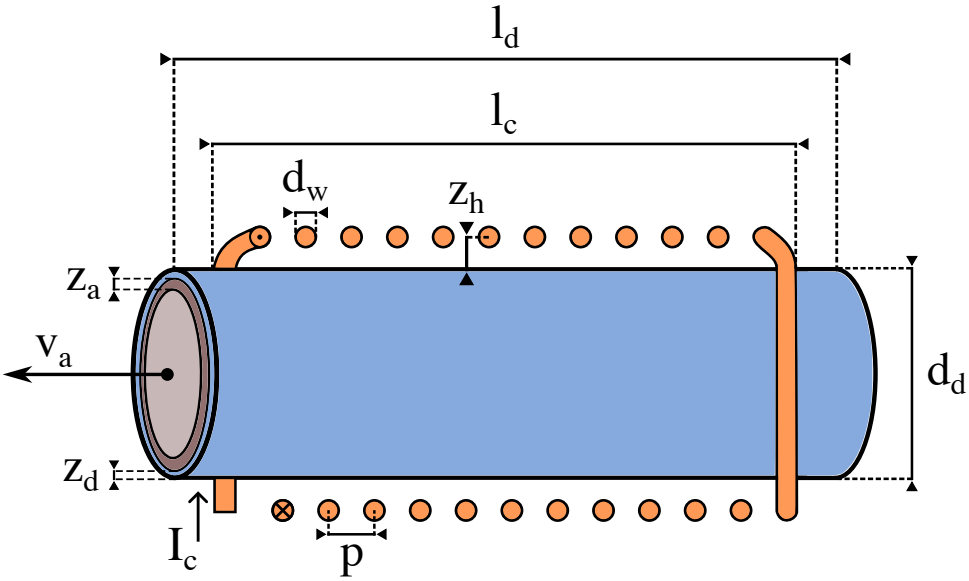

Figure 3.4: Stylized diagram of the induction heater based on the model description in COMSOL Multiphysics. The geometrical properties of the induction heater are indicated in the figure. Note the aggregate layer alongside the inside circumference of the drum.

3.3. TEST SETUP DESIGN

The test setup should heat aggregates to the same temperature as needed in the asphalt production process but with the mass flow scaled to the size of the test setup.

The test setup design procedure will be discussed in this section. The following paragraphs will highlight the underlying considerations of the test setup design and

serve as an example of the design process that can be applied to a full-sized heater.

First, the design criteria will be discussed. Following that, the design parameters and process variables are highlighted. Then, rudimentary relationships between the design parameters and criteria are established. Finally, a parameter space search is done and the test setup design is presented.

3.3.1. DESIGN CRITERIA

The first step in the design process is to translate the overall design goal into specific design criteria.

The goal is to heat the aggregates to production temperatures. From Table 3.1, it is known that the temperature range for aggregates in asphalt production is 150 °C to 200 °C. The test setup will be designed to work in the more narrow band of 165 °C and 185 °C. Ideally, the design is made such that the current can be varied to change the temperature within this range. Therefore the maximum current should not correspond to an aggregate temperature equal to or lower than 185 °C.

Secondly, the cost of the test setup should be minimized. The test setup cost is decided by the cost of the drum and the copper coil. Because of price differences between copper and steel, the cost of the coil is the dominant factor here.

Finally, the system efficiency should be maximized. System efficiency can be split up into power converter efficiency η_{con}, coil efficiency η_{coil}, and heater efficiency η_h. Converter efficiency η_{con} is typically over 90% due to advances in converter design and solid-state switch quality. The converter efficiency will not be discussed further in this thesis. Coil efficiency η_{coil} describes how much of the power used by the coil heats the workpiece and how much is lost in the coil resistance. η_{coil} can reach high values if there is good magnetic coupling between the coil and the drum, which can be assumed here, and if wires with low AC resistance (such as Litz wires) are used. This was previously discussed in section 2.2.2. Finally, η_h refers to the efficiency of the heat exchange between the drum and the aggregate. This is influenced by the thermal conduction between the drum and the aggregate, convection between the drum and the outside world and radiation from the drum to the outside world. Table 3.2 shows a list of the design criteria of the heater.

Table 3.2: Design criteria and goal values.

Design criteria	**Values**
Aggregate output temperature	165 - 185 °C
Cost	Minimize
η_{coil}	Maximize
η_h	Maximize

3.3.2. MATERIALS OF TEST SETUP

The material choice for the drum heater is based on conventional engineering knowledge and experience.

The drum is made out of carbon steel because of its high magnetic permeability and good thermal characteristics. Due to its strength and hardness steel is very commonly used for industrial machines, such as the gas-fired drum heater.

The coil is made out of copper since it has excellent electrical conductance. Copper is almost universally used as the conducting material in applications for which weight is not an important consideration, e.g. the stationary coil in an industrial heater.

The structural elements of the test setup were made out of MDF, an engineered wood that consists of pressure-treated pulp. MDF is chosen because it can be easily laser-cut into custom-designed parts. Furthermore, its burning temperature is high enough to withstand the temperatures which will be reached during testing.

As a final note on material choice: steel tubes and copper Litz wires are relatively easily available. While some exotic materials might be better suited to serve as the drum or coil, practical limitations demand the use of available materials.

3.3.3. DESIGN PARAMETER INVESTIGATION

Design parameters are the variables of the induction heater which can be changed when creating the design. In principles, design parameters can include material properties, since the engineer is free to choose the materials which he or she sees fit. However, as described in Section 3.3.2, the materials of the test setup were chosen based on common engineering knowledge and the material's availability.

This leaves the geometric properties of the heater as the design parameters which the engineer can change. The design parameters of the heater are:

- Drum length l_d
- Drum diameter d_d
- Coil length l_C
- Wire diameter d_w
- Drum-wire distance z_h
- Number of coil turns N or pitch p

Process variables are parts of the heating process which can be controlled. The process variables considered in this analysis are:

- Coil current I_C
- Frequency f
- Aggregate flow velocity v_a

The process variables must be taken into account when designing the machine since it should be able to produce the desired results while operating within an acceptable

range of the process variables.

Basic relationships between the design parameters and the criteria were established through COMSOL modelling as part of the design process. This is done by varying the design along one geometrical parameter while keeping the others constant. Below the parameter relationships for the aggregate output temperature and the heater efficiency are discussed.

AGGREGATE OUTPUT TEMPERATURE

Figure 3.5 shows the aggregate temperature along the length of the drum, for drums of different lengths which all use a coil with N = 64 windings. Given the same amount of windings, a longer drum results in a lower aggregate end temperature. The longer drum will have less heating power generated in it because workpiece length is inversely proportional to inductance and equivalent resistance, as previously shown in Equations 2.6b and 2.11. Furthermore, a longer drum has a larger area through which heat losses occur, meaning that for the same input heating power, it will have a lower temperature. The lower drum temperature also results in less heat transfer to the aggregate and a lower final aggregate temperature.

However, from Equation 2.11 it is also known that the equivalent resistance can be increased by increasing the number of coil windings. From a practical standpoint, this means increasing the length of the drum. Therefore, it is valuable to investigate how these opposite effects, an expected increase in heating power for a higher number of turns but a decrease in heating power for a longer workpiece, come together. Figure 3.6 shows the aggregate temperature along the length of the drum, for drums of different lengths, each with a different number of turns. The coil length is $l_c = l_d - 150\text{mm}$ and the number of coil turns is $N = (l_c - p)/p$ rounded up to the nearest integer. It can be seen that the aggregate temperature rises linearly with the increase in the length of the drum and the number of windings. Notably, the increase in temperature is not quadratic because the increase in barrel length works to decrease the heating power. This leads to the conclusion that increased barrel length can lead to achieving higher aggregate temperatures if the extra space is used to apply more coil windings.

Finally, it is notable that the aggregate temperature flattens out when it reaches the drum outlet. This is around the point where the induction coil, and therefore the region of heat generation, ends. From this observation also follows that the induction coil should cover as much of the drum as possible.

The relationship between aggregate temperature, drum diameter and aggregate flow velocity is investigated below. The volumetric flow rate $\dot{V}$ in m^3/m is constant in steady state conditions since the mass flow rate $\dot{m}$ and the density ρ are constant. Volumetric flow rate is $\dot{V} = v_a A$, where v_a is the flow velocity of the aggregate and A is the cross-sectional area of the aggregate stream.

Figure 3.7 plots the aggregate output temperature as a function of the drum diameter. The simulated aggregate temperature rises steadily with an increasing drum diameter. This is because it the aggregate stream has a constant cross-sectional

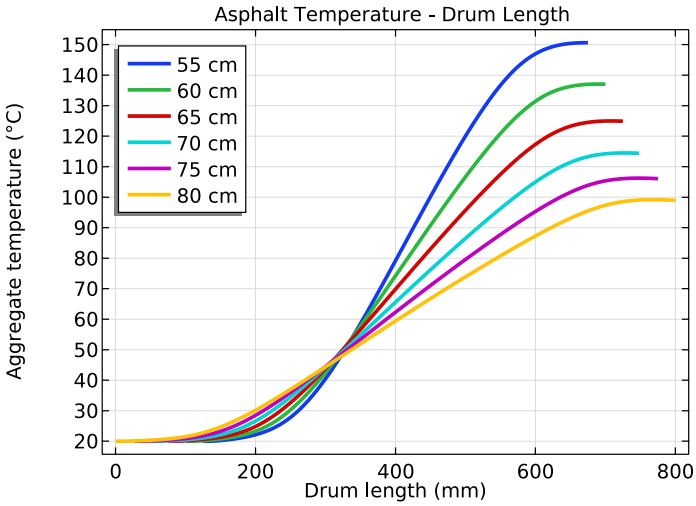

Figure 3.5: Relationship between aggregate temperature T_a and drum length l_d for heater with drum diameter d_d = 159mm, copper wire diameter d_w = 5mm, drum-wire distance z_h = 10 mm, current I = 20A, frequency f = 10 kHz and number of turns N = 64.

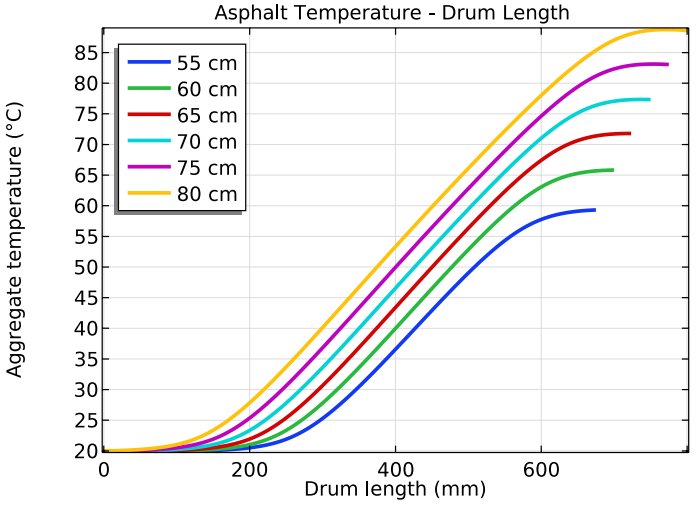

Figure 3.6: Relationship between aggregate temperature T_a and drum length l_d for heater with drum diameter d_d = 159mm, copper wire diameter d_w = 5mm, drum-wire distance z_h = 10 mm, current I = 20A, frequency f = 10 kHz and a variable number of turns.

area A and is modelled in COMSOL to stick to the circumference of the drum. As the drum diameter gets larger, the aggregate layer becomes thinner to maintain the same area. The thinner asphalt layer is less resistive to conductive heat transfer. Furthermore, a larger area of aggregate is now in contact with the drum, allowing for higher heating power and a corresponding higher aggregate outlet temperature. However, the rate of decrease in aggregate layer thickness slows down once the drum approaches very large diameters and the aggregate temperature flattens out accordingly. Although the assumption that the aggregate sticks to the circumference of the drum is an obvious simplification, the general principle that the aggregate layer becomes thinner and the contact area becomes larger for drums with a larger diameter is correct.

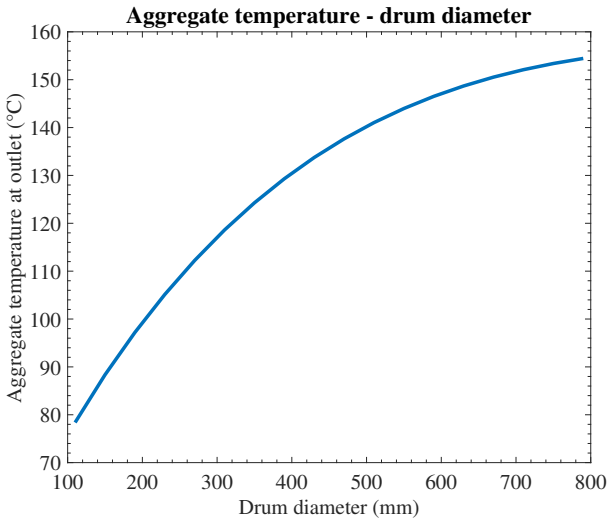

Figure 3.7: Relationship between aggregate temperature T_a and drum diameter d_d for heater with drum diameter l_d = 700 mm, copper wire diameter d_w = 4 mm, drum-wire distance z_h = 10 mm.

EFFICIENCY

The quality of a heater design is partially judged by its efficiency. The efficiency of the induction heater can be thought of in multiple ways. In this thesis, the coil efficiency and the heater efficiency will be studied. The coil efficiency η_c is the efficiency with which electromagnetic energy from the coil is transformed into heat energy in the drum. It is expressed in Chapter 2 by Equation 2.12. The heater efficiency η_h expresses how much heating power generated in the drum is used to heat the aggregates from their start temperature T_1 to their end temperature T_2. To calculate these efficiencies, Q_E and Q_{in} are calculated in COMSOL and P_c is calculated by combining outputs from COMSOL with the skin effect and proximity effect equations presented in Section 2.4.

It is important to note that the efficiency calculations and the parameter space search were done with an older version of the COMSOL model which did not use the enhanced aggregate specific heat to take into account the presence of moisture and which assumed much higher losses to the outside world. Due to these higher losses, the calculated efficiency values are lower than what is actually to be expected. However, after recalculating efficiencies for solid wire coils, it is found that the general trend of the efficiency calculations still holds. Since it is not trivial to recalculate the Litz wire efficiencies, it is decided to keep the old figures in the thesis to portray the differences in efficiency between the solid wire and the Litz wire design.

The coil efficiency that is calculated from the simulation is stable and high within the range of practical values for most of the design parameters, consistently reaching 95% or higher. This is in agreement with the literature cited in section 2.2. The wire diameter is the only design parameter for which the coil efficiency varied significantly, as shown in Figure 3.8. For a specific design using a solid wire for the coil, the efficiency is low for diameters under 1 mm and increases quickly for larger diameters, until it stabilizes at 97%. This makes sense, as both AC and DC resistance decreases with increasing wire diameters.

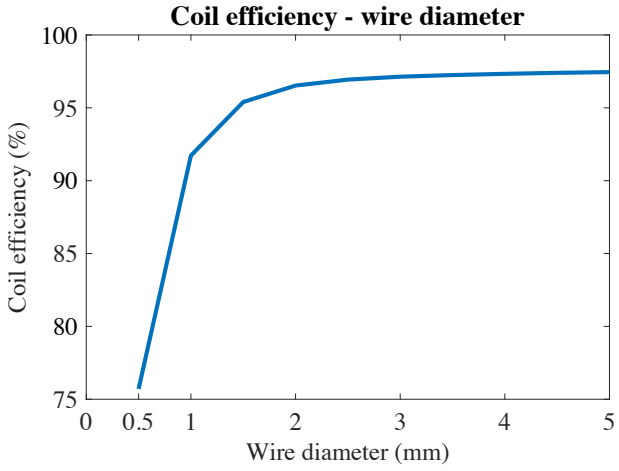

Figure 3.8: Relationship between coil efficiency η_c and wire diameter d_w.

The heater efficiency that is calculated from the simulation is more varied within the practical ranges of the design parameters. The heater efficiency for the heater designs considered in this thesis ranged from 35.0% to 55.2%. It is much lower than coil efficiency because the drum design is not optimized for this heat transfer.

As shown in Figure 3.9, heater efficiency is inversely proportional to drum diameter. The increasing drum diameter results in a larger outside area through which radiative and convective heat loss occurs. Furthermore, in the previous section, it was discussed that a larger drum diameter leads to a higher drum temperature for the same coil current. This increase in drum temperature leads to

higher losses, as the radiative loss is proportional to the 4_{th} power of the drum temperature.

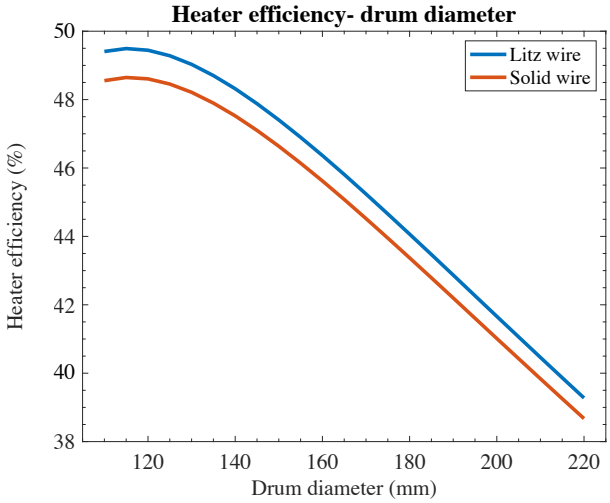

Figure 3.9: Relationship between heater efficiency η_H and drum diameter d_d for heater with length l_d = 700mm, number of turns N = 79, copper wire diameter d_w = 3 mm and drum-wire-distance z_h = 21.5 mm

Furthermore, the efficiency is inversely proportional to drum length 3.10. In the simulation, the number of coil windings is proportional to the drum length, meaning efficiency drops even as the heating power and aggregate temperature increase. This can also be attributed to a larger surface area and higher temperature, leading to higher (radiative) losses.

3.3.4. PARAMETER SPACE ITERATION

A parameter space search is done to find a drum heater design that fits the design criteria. The COMSOL model of the heater is varied along the design parameters and process variables. Following that, a simulation is run for each design to find its steady-state thermal behaviour. Finally, the outcomes of the thermal simulation were compared against the design criteria, to find the optimal design.

As with the efficiency calculation, the COMSOL model used for the parameter space search did not take into account the moisture content in the aggregate specific heat and assumed much higher convective and radiative losses. Due to the higher assumed losses, the designs found in this process were rather over-designed.

The varied parameters were drum length, drum diameter, wire diameter, frequency, and current. Along each axis the design is iterated upon and all designs that satisfy the aggregate output temperature requirement were compared. Between these designs, the efficiencies are compared and the most efficient is chosen as the final

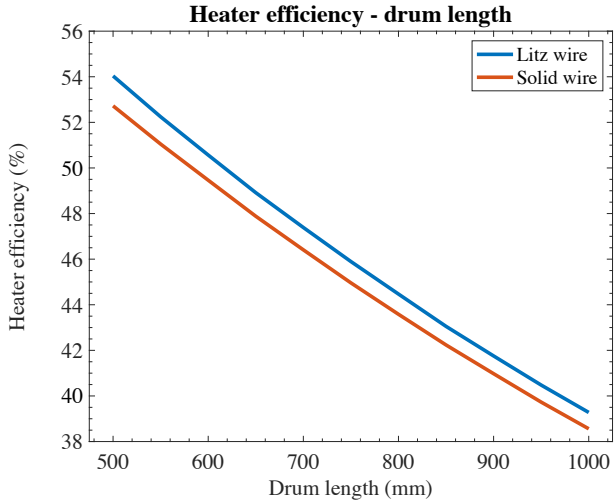

Figure 3.10: Relationship between heater efficiency η_H and drum length l_d for heater with drum diameter d_d = 150mm, copper wire diameter d_w = 4 mm, drum-wire distance z_h = 21.5 mm.

design.

The drum length, drum diameter, and wire diameter together define the physical design of the heater. The coil length is found by subtracting the amount of space that is used for the drum support from the drum length. For the test setup, this is 75 mm at each side. The number of turns is defined as $N = (l_c - p)/p$.

The current and frequency indicate the operating conditions at which the desired temperatures can be reached.

The design parameters were varied between the values shown in table 3.3. This resulted in 800 different designs which were each simulated in COMSOL.

Table 3.3: Design parameters and values of the induction heater

Design parameter	**Values**
drum diameter	12 cm, 14 cm, 16 cm, 18 cm, 20 cm
drum length	50 cm, 60 cm, 70 cm, 80 cm, 90 cm
Wire diameter	3 mm, 4 mm
Current	20 A, 25 A, 30 A, 35 A
Frequency	5 kHz, 10 kHz, 15 kHz, 20 kHz

3.3.5. DESIGN RESULTS

Of the 800 designs, 71 produced the desired aggregate output temperature. The coil efficiency changed little between the satisfactory designs, ranging from 96.66 % to 98.36 %. The heater efficiency varied more widely, starting at 36.10% and reaching

55.15%. Finally, the coil cost calculated as the price for the weight of the required copper ranged from 10.03 euro to 52.53 euro.

Based on these results, the provisional design described in Table 3.4 is chosen because it has the highest efficiency and lowest cost while still meeting the aggregate temperature criteria.

Table 3.4: Provisional test setup heater design

Design parameters				
L (cm)	**D (cm)**	**d (mm)**	**I (A)**	**f (kHz)**
70	16	3	25	5
Results				
T (°C)	**Coil cost (€)**	η_h	η_{coil}	η_{tot}
167	20	47.71%	98.10%	46.20%

FINAL DESIGN

To limit the options further, the availability of material had to be taken into account. Since no drums with a diameter of 12 cm, 18 cm, or 20 cm were readily sold, these designs had to be discarded. Finally, the wire diameter proved a practical limitation.

However, two practical considerations drove the design to be changed. Firstly, the only available Litz wire to build the test setup is a diameter of 4.8 mm. The large wire diameter increased the usable current range to a comfortable level but decreased the number of turns that could fit on the drum. To keep the necessary current at a reasonable level, which is important for limiting the size of the switches and capacitors on the power converter, the drum length had to be increased to achieve the same aggregate temperature.

Secondly, due to the size of the drum supports the drum length had to increase further, otherwise the drum openings would be partially covered by the support structure. Given these changes, the final geometrical design of the drum heater is presented in table 3.5.

Table 3.5: Final test setup heater design

Design parameters			
L (cm)	**D (cm)**	**d (mm)**	**N**
80	15.9	4.8	64

A test setup with these properties is designed using Siemens Solid Edge. The drum is made from a steel tube with 159 mm diameter and 5 mm wall thickness. The steel type is unknown. The coil is made out of Litz wire with a 4.8 mm total diameter consisting of 2200 strands of 0.071 mm diameter. The wooden support structure is made out of MDF. The different wood pieces were cut using a laser cutter and fit together like a puzzle. The induction heater test setup without the coil is shown in

Figure 3.11. The completed heater test setup with the coil is shown in Figure 3.12.

The simulated electrical and thermal behaviour of this design will be discussed in Chapter 4. The test setup and electrical and thermal tests will be discussed in Chapter 5.

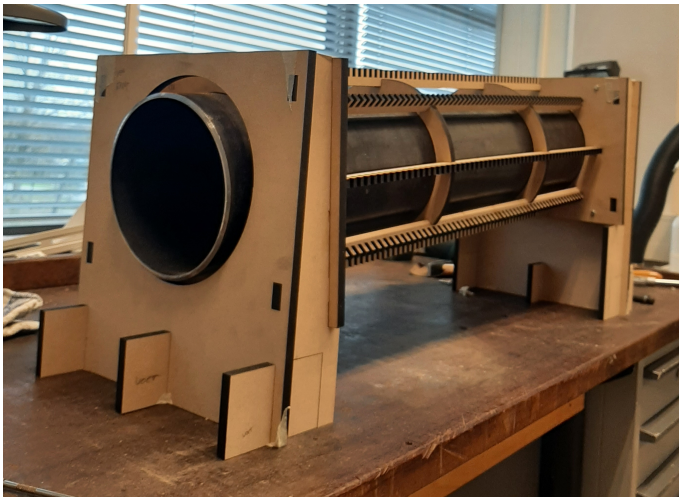

Figure 3.11: Induction heater test setup without the coil. Note the puzzle piece design of the support structure and the winding guards.

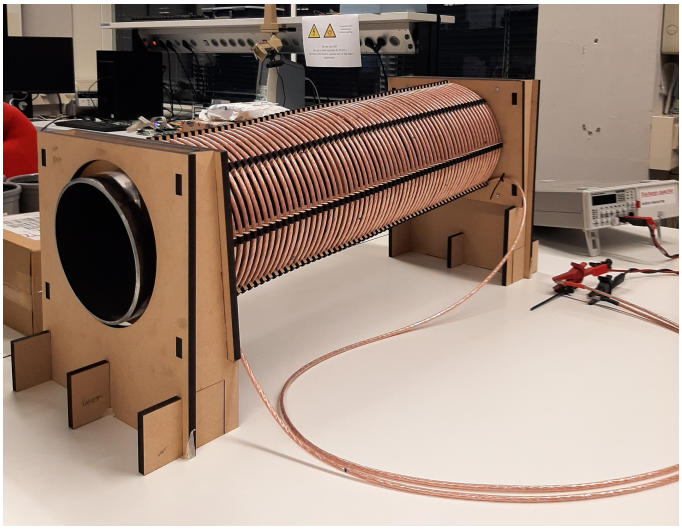

Figure 3.12: Completed induction heater test setup with the coil.

3.4. RESONANT CONVERTER

In the following section, the design of the resonant converter will be concisely described. The choice of the resonant capacitors will be highlighted.

The design for the resonant converter was provided by members of the electrical power engineering research group. The resonant converter is shown in Figure 3.13. It consists of two half-bridge converters stacked on top of each other. The wires feeding the coil and capacitor bank can be seen on the left (A), the large capacitors which stabilize the DC voltage can be seen in the middle (B), and the gate drivers which control the MOSFETs shown on the right (C) and the wires which come from the DC power source are shown on the far right (D). The MOSFETs for the resonant converter were chosen based on their footprint and their switching losses.

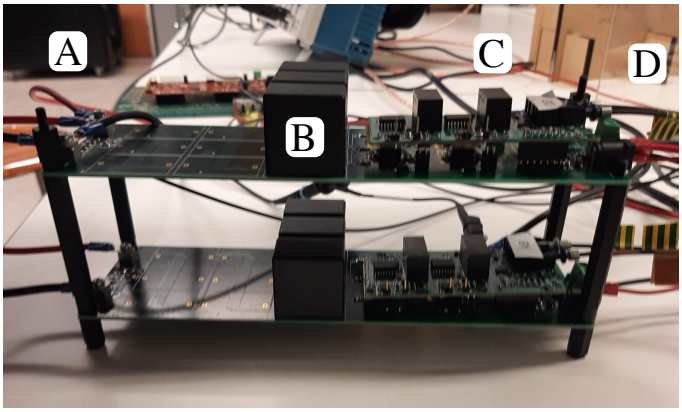

Figure 3.13: H-bridge used in the test setup. (A) Wires that connect to the coil and capacitor bank. (B) DC capacitors to stabilize the output voltage. (C) Gate drivers to control the MOSFETs. (D) Wires that connect to the DC power supply.

A capacitor bank had to be designed as part of the resonant converter. The total capacitance is calculated according to 2.40 and is therefore a function of the inductance of the coil and the frequency at which the induction heater is intended to be operated. The coil inductance is measured for a range of frequencies. At f = 10 kHz the inductance is measured to be L_r = 126.72 μH. This results in a total capacitance of C_r = 1.999 μF which is rounded up to At f = 10 kHz the inductance is measured to be L_r = 126.72 for practical purposes. The capacitor bank consists of two parallel rows of eighteen capacitors of C = 0.222 μF. The extra row is used because capacitors have a maximum operating voltage and multiple capacitors should be used in series to keep the voltage at a safe level. However, putting two capacitors with the same value in series halves the total series capacitance and therefore extra capacitors had to be added in parallel, resulting in the 2x18 configuration. The maximum capacitor voltage during operation is determined with the COMSOL model, discussed in Section 4.3.

The converter is controlled with a simple open loop PWM controller created in Simulink and run on a Launchpad TI C2000. The controller produced a square wave in the switching frequency which toggled an optical signal on and off. In turn, the optical signal served as input for the gate drivers, which directly control the switches of the H-bridge.

4

MODELLING

The induction heater's behaviour is simulated with a model of the heater, consisting of a COMSOL simulation describing the electromagnetic heat generation and MATLAB script describing proximity and skin effect losses in the coil.

4.1. HEATER MODEL DESCRIPTION

The COMSOL model aims to simulate the electromagnetic heat generation in the drum through FEM. The material properties and geometry of the heater are described in the model. Additionally, the structural and governing equations for the physics are defined. Finally, the characteristics of the mesh and study are given. In this section, each aspect of the model will be discussed.

4.1.1. GEOMETRY

The geometry of the COMSOL model is shown in Figure 4.1. The model is two-dimensional (2D) axisymmetric, meaning its geometry is drawn in a flat plane, which is then rotated along an axis of rotational symmetry to achieve the three-dimensional geometry. This model type is chosen because it allows for a reasonably accurate geometrical representation of the heater while ensuring limited simulation time. A three-dimensional (3D) model would be more accurate but would require significantly more computational resources.

In the model, the static outside world is defined as a large rectangular area named Outer air. It is bordered by an infinite element domain, which i.e. sets the boundary of the outside world to infinity, ensuring the simulation outcomes are not influenced by the boundaries of the model geometry. The heater itself is defined as a group of parallel rectangles of the same length. The thin, outer rectangle is the drum wall, the middle rectangle is the aggregate and the wide, inner rectangle is the inside of the drum, which is filled with slow-moving air. Because the model is 2D axisymmetric, the aggregate is modelled as a cylindrical layer moving along the inside of the drum wall. This aspect of the model is not realistic, since in actuality the aggregate would form a pile at the bottom of the drum. The model therefore assumes more efficient heat transfer from the drum to the aggregate, as the contact surface between

aggregate and the drum wall through which conductive heat transfer happens, is larger in the model. Finally, the coil is modelled as a column of circles, separated from the drum by a small gap. The axisymmetric model would interpret these circles to be distinct rings instead of the unbroken windings of a single coil. However, the model properties can be set to interpret the circles as belonging to a single continuous coil. Note that the coil is modelled as a solid wire instead of as a Litz wire to minimize model complexity and computation time. The loss-reducing effects of the Litz wire are modelled separately using the equations described in section 2.4.

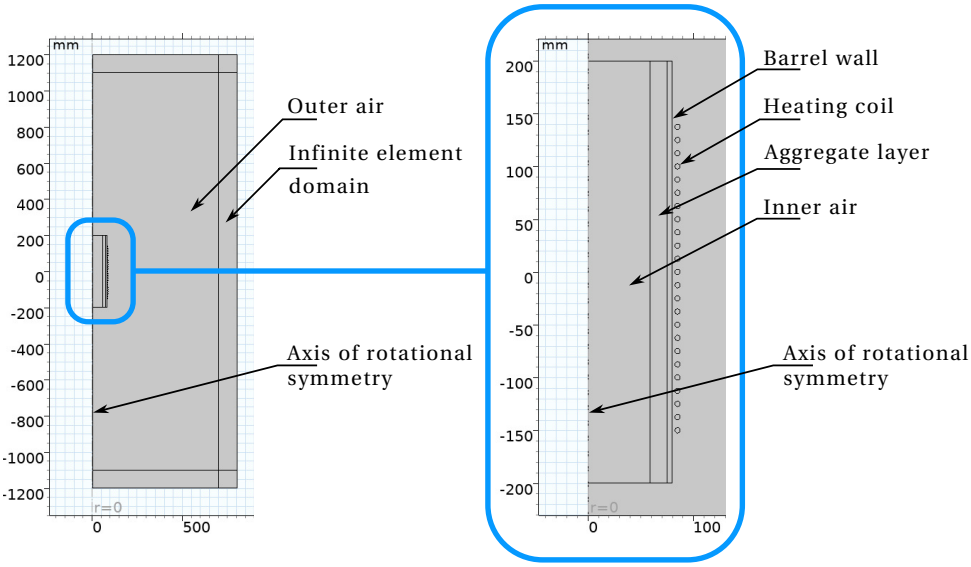

Figure 4.1: Geometry in COMSOL.

A stylized diagram of the induction heater is shown in Figure 3.4.

4.1.2. PHYSICS

The electromagnetic and thermal phenomena that underpin the working of the induction heater are described by partial differential equations (PEDs), which are discussed in Chapter 2. It is not practical to solve these PEDs analytically and instead, numerical methods are used. COMSOL is a simulation software which uses the finite element method (FEM) to solve PEDs numerically. In this thesis, COMSOL is used to simulate the behaviour of the induction heater.

Numerical methods are powerful and can solve a wide range of physical problems. However, as the complexity of the model increases, the time and computational resources required to find a solution increase as well. Because of this, it is in the interest of the engineer to apply simplifications to the model. In the following

paragraphs, the modelling of the electromagnetic and thermal phenomena will be described and the most significant simplifications will be highlighted.

Firstly, the electromagnetic behaviour is simulated by solving Maxwell's equations and Ohm's law as given by Equations 2.1 and 2.3. A current is applied to the coil and the resulting magnetic and electric fields in the coil and drum are calculated from that. The inside of the drum is defined to be magnetically insulated from the rest of the model, as it is assumed that the magnetic field completely couples with the drum itself.

The magnetic hysteresis of steel is not modelled. Hysteresis models are often complex and therefore significantly add to the computation time of a simulation. For example, it is often modelled by using the Jiles-Atherton method, which involves solving 2 extra differential equations and determining the values of 5 different model parameters whose values are not readily available in material databases [39]. At the same time, the contribution of hysteresis losses to the overall heating power is usually less than 10 per cent. Because of this, the average BH-curve for low-carbon steel is used instead. The average BH-curves for common materials are included in COMSOL. They lack hysteresis but include saturation [40]. The average BH-curve for low carbon 1010 steel used in the model is shown in Figure 4.2. Because of this simplification, the additional heat generated by hysteresis losses is not modelled and thus the total heating power for a given electrical input power will be lower.

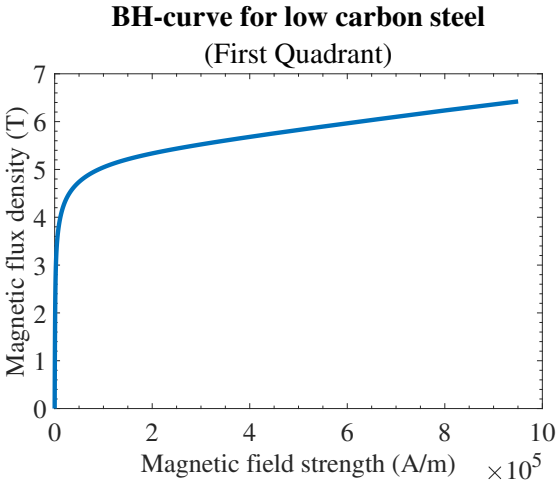

Figure 4.2: BH-curve for low carbon steel 1010 used in the COMSOL model. Note the saturation from H = 1.0×10^5 A/m onwards.

Secondly, the heat transfer is calculated using an energy balance and heat equations similar to those in Section 2.3. The heat transfer within the aggregate and the drum as well as the heat transfer between the two are modelled as conduction. The heat loss to the outside world is modelled in two steps as natural convection and as radiation by using Equations 2.16 and 2.23 respectively. The coefficient of

natural convection for the drum is calculated using 2.20 to be $h = 5.1248$. The emissivity of the drum is set to $\epsilon = 0.79$, which is the emissivity for oxidized steel.

An important simplification in the heat transfer calculations is that the aggregate is modelled as a fluid instead of as the granular flow of many solid particles. Describing the physics of granular matter is difficult because it exhibits both fluid-like and solid-like behaviour depending on the circumstances. Therefore there are no constituent equations which cover all situations [41]. There are numerical methods to describe granular flows such as the Discrete Element Method (DEM), which calculates the contact force interactions between all individual particles. However, DEM is computationally expensive and it is not trivial to combine it with thermal simulations [42] [43]. The aggregate flow is modelled as a fluid for these reasons.

4.1.3. MATERIALS

The materials properties used to describe thermal and electromagnetic behaviour in the COMSOL model are shown in Table 4.1. Some properties for steel and air are given as functions since they are not constant throughout the simulation.

Table 4.1: Material properties as defined in COMSOL. Note that some properties, most notably the relative permeability of steel, are not constant [44].

	Copper	Steel	Aggregate	Air
Density, ρ (kg/m^3)	8940	7850	2300	$\rho_{air}(T,P)$
Relative permeability, μ_r	1.0	$\mu_{r,steel}(\vec{H})$	1.0	1.0
Relative permittivity, ϵ_r	1.0	1.0	6.0	1.0
Electrical conductivity, σ_r (S/m)	4.25×10^7	5.41×10^6	1.0×10^{-6}	0
Heat capacity, C_p $(J/kg \cdot K)$	385	520	1029.3	$C_{p,air}(T)$
Thermal conductivity, k $(W/m \cdot K)$	400	54	1	$k(T)$

First, as was described in subsection 2.1.2, the relative permeability of steel is the derivative of steel's BH-curve. This means that μ_r is a function of the external magnetic field $\vec{H}$. In COMSOL, this relationship is defined as an interpolation of data points from a table of corresponding $\vec{B}$ and $\vec{H}$ values. Figure 4.2 shows the BH-curve for steel used in the simulation.

Second, the density of air is modelled with the ideal gas law, as described by Equation 4.1. Here p is the air pressure, v is the inverse of the density, also known as the specific volume, and R is the mass-specific ideal gas constant for air.

$$pv = RT \iff \rho = \frac{p}{RT} \tag{4.1}$$

Third, the heat capacity and thermal conductivity of air are functions of temperature. The COMSOL model describes both of these properties as 4^{th} degree polynomials, a common way to express heat capacity and thermal conductivity [45]. The coefficients are given in table 4.2.

Other values which could be modelled as functions are given as constants to minimize model complexity. Notably, the electrical and thermal conductivity of

copper and steel are modelled as constant but are in reality functions of temperature, and the thermal conductivity of aggregate is modelled as isotropic but actually varies throughout the volume of the aggregate.

Table 4.2: Coefficients for the fourth degree polynomial description of heat capacity $c_{p,air}(T)$ and thermal function $k_{air}(T)$ of the form $f(T) = a_1 + b_1 T + c_1 T^2 + d_1 T^3 + e_1 T^4$.

	a_1	b_1	c_1	d_1	e_1
$c_{p,air}$	1047.64	-0.373	9.45×10^{-4}	6.02×10^{-7}	1.29×10^{-10}
k_{air}	-0.00228	-1.15×10^{-4}	-7.90×10^{-8}	4.18×10^{-11}	-7.44×10^{-15}

4.1.4. MESH

The simulation is performed using a two-dimensional mesh consisting of 168520 elements. The mesh is calibrated for general physics and has the element size predefined as extremely fine, which is the highest level of detail. For the Free Triangular elements, the number of iterations and the maximum element depth to process were both set to 8. Furthermore, no sensitivity study is done because the simulation is able to be completed in a reasonable time at the highest detail setting.

The mesh geometry is shown in Figures 4.3, 4.4 and 4.5. Figure 4.3a displays the mesh geometry of the top half of the model. The infinite domain consists of rectangular elements, whilst the air outside and inside of the drum is made up of small triangular elements. The more detailed elements of the drum, coil and aggregate are not distinguishable from each other at this level of zoom which results in a large black area in the lower left. Figure 4.3b provides a more detailed look at the middle of the drum. From left to right one can see the inner air, the aggregate, the drum wall and the coil as distinct regions. The aggregate is rather detailed in comparison to the inner air and consists of both rectangular and triangular elements. The drum wall mesh is more clearly shown in Figure 4.4. It is defined as a boundary layer mesh, with the elements closest to the drum wall surface having a thickness of $\frac{\delta}{4}$. The elements increase in size by a factor of 1.2 towards the middle of the drum wall. By using this geometry, variations in current density and magnetic flux density which follow the skin effect can be captured very well. The boundary layers are applied to all sides of the drum wall to ensure the geometric consistency of the mesh and decrease the amount of anomalies in the simulation. The boundary layer elements can be seen for the top of the drum in Figure 4.4a whilst the smallest boundary layer elements are shown neatly in Figure 4.4b. The coil mesh is shown in Figure 4.5. Because coil skin depth is larger than the drum skin depth and the coil losses are of less interest for this thesis, the mesh for the coil is simply a detailed triangular mesh without the more computationally expensive boundary layer elements. To verify that this simpler model would still output representative results, the simulation was run with a coil mesh which did include boundary layer elements and it was found that the results only differed very little.

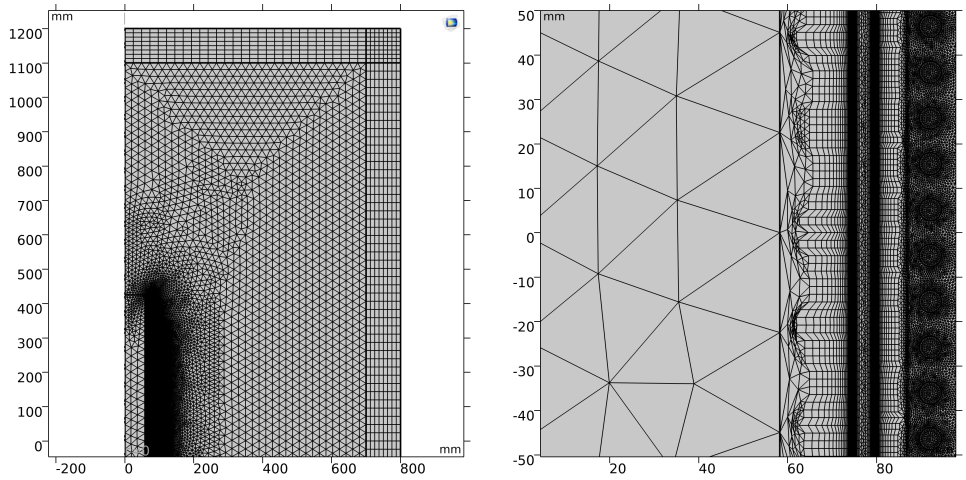

(a) Mesh of the top half of the model. Rectangular elements of the infinite boundary and the triangular elements of the air can be seen.

(b) Mesh of the drum and coil. The aggregate layer has detailed but individually recognisable elements, while the drum and coil are nearly black.

Figure 4.3: Mesh of the COMSOL model.

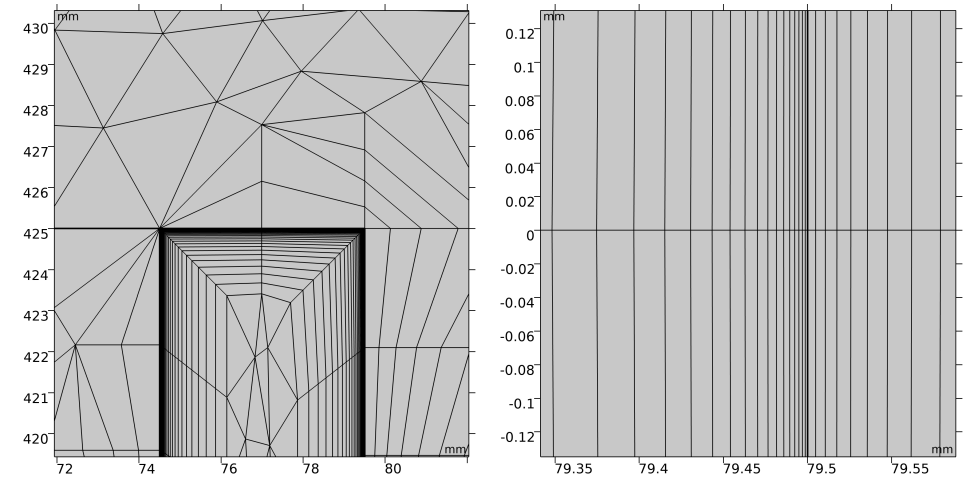

(a) Detailed image of the mesh at the top of the drum. The rectangular boundary layer elements along the drum wall can be seen.

(b) Very detailed image of the mesh at the middle of the drum wall. Note the increasing thickness of the boundary layer elements.

Figure 4.4: Mesh of the drum wall.

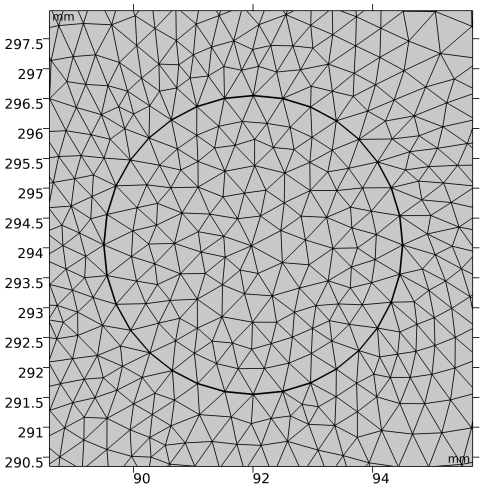

Figure 4.5: Mesh of the coil

4.1.5. STUDY

The desired output of the simulation is the temperature field of the heater at thermal equilibrium. The changing electromagnetic field is simulated with a frequency study, which then forms the input for a stationary study which computes the steady state temperature field [46]. This way, the aggregate output temperature can be found. Furthermore, a frequency-transient study was done to determine the time-dependent behaviour.

4.2. HEATER MODEL RESULTS

The COMSOL model serves two purposes. Firstly, it is used to determine the optimal heater design. This is done by investigating the relationship of the design parameters to the aggregate output temperature, as well as to the heater efficiency. The simulated heater design that can heat the aggregate to the desired temperature with the highest efficiency will be chosen as the basis of the mock-up. Secondly, the model is used to predict the thermal behaviour of the heater. Thermal simulations are run for different operating conditions to find the maximum and minimum temperatures and the temperature pattern on the heater.

In this section, the model results will be discussed. The drum behaviour is simulated for two different situations. First, the test described in Chapter 5 is simulated, with the same current and frequency being used. This simulation will be referred to as the Test scenario. Note that, although the test setup is designed to be run at 10000 Hz, the test was done at 8000 Hz because the induction of the coil increased at higher power. Second, a simulation is done of the test setup heating a stream of aggregates. This simulation will be referred to as the Aggregate stream scenario. The values for the process variables of both scenarios are shown in Table

4.3. Since for the Test scenario there is no aggregate in the drum, the flow variables are zero. The geometries and material properties are the same for both scenarios and are equal to the values discussed in the previous sections, unless otherwise noted.

Table 4.3: Process variable values for the Test scenario and the Aggregate Stream Scenario.

	Test scenario	Aggregate stream scenario
Current (A)	8.7	24
Frequency (Hz)	8000	10000
Aggregate mass flow (kg/h)	-	39.4
Aggregate flow velocity (m/s)	-	0.0007
Air mass flow (kg/h)	-	0.046
Air flow velocity (m/s)	-	0.001

4.2.1. ELECTRICAL RESULTS

The global electrical results of the simulation per scenario can be found in Table 4.4. Notably, in the Test scenario simulation, the expected power consumption of the coil during the test is 314.76 W and heating power is 309.90 W. The resulting coil efficiency is 98.5%, which in line with the earlier discussion on high coil efficiency. The coil power for the Aggregate stream scenario its 2285.4 W and the heating power is 2244.3 W.

Table 4.4: Global electrical simulation results for the Test scenario and the Aggregate Stream Scenario.

	Test scenario	Aggregate stream scenario
Coil voltage amplitude(V)	142.16	368.8
Coil resistance (Ω)	8.32	7.94
Coil power (W)	314.76	2285.4
Electrical losses/heating power (W)	309.90	2244.3
Coil efficiency (%)	98.5	98.2
Skin depth (mm)	0.053	0.047

It is of interest to investigate the induced eddy currents which generate the heating power in the drum. As discussed in Subsection 2.2.2, the induced current density is highest at the outside surface of the drum and decreases towards the centre of the drum. The skin depth δ is the distance from the surface at which the current density has decreased to $1/e$ or about 37%.

Table 4.4 lists the skin depth δ as calculated by Equation 2.10 from Section 2.2.2. To verify the agreement between the analytically calculated skin depth and the simulation, the normalized magnetic flux density and current density are plotted as a function of the depth from the drum surface in Figures 4.6 and 4.7 respectively.

The plots show the values for the middle of the drum and for the point along the length of the drum at which the coil starts, here called Drum top. The values for both positions are plotted to verify that the skin depth values are correct even as the magnetic flux density and the magnetic coupling change. The calculated skin depth for the Test scenario is $\delta = 0.053\ mm$. It is shown in the figures as a vertical dotted line, while $1/e$ is shown as a horizontal dashed line. The intersection between these lines is the theoretical value for the normalized magnetic flux density and the normalized current density at the skin depth. It can be seen that the graphs line up with the expected value. The actual values are $B = 2.04\ T$ and $J = 2.06 \times 10^7\ A/m^2$ for the middle of the drum and $B = 1.12\ T$ and $J = 1.13 \times 10^7\ A/m^2$ for the point at which the coil starts. Finally, it should be noted that the graphs for the magnetic flux density and current density have nearly the same shape, which is to be expected based on Faraday's law of induction.

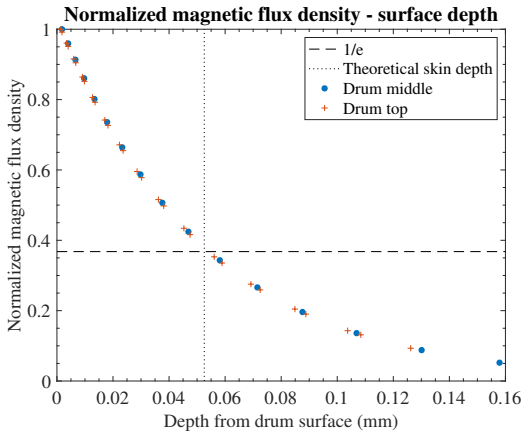

Figure 4.6: Normalized magnetic flux density from the surface depth.

The electromagnetic behaviour of the Aggregate Stream Scenario is essentially the same, although the skin effect is smaller due to the higher frequency and larger magnetic flux density and current density as a result of the increased coil current.

4.2.2. THERMAL RESULTS

The temperature profile of the drum for the Test scenario is shown in Figure 4.9b. It is symmetrical, with the middle of the drum reaching the highest temperature of 101.0 °C and the inlet and outlet of the drumming having the coldest temperature of 67.0 °C. It is expected that the ends have a lower temperature since they are not covered by the coil and are therefore not directly heated. The ends instead heat up through conduction from the drum middle, ensuring a temperature gradient towards the middle. Furthermore, it can be seen that the air temperature at the point of contact with the drum is equal to the drum temperature, but as one gets closer to the drum centre, the region of maximum air temperature gets more narrow.

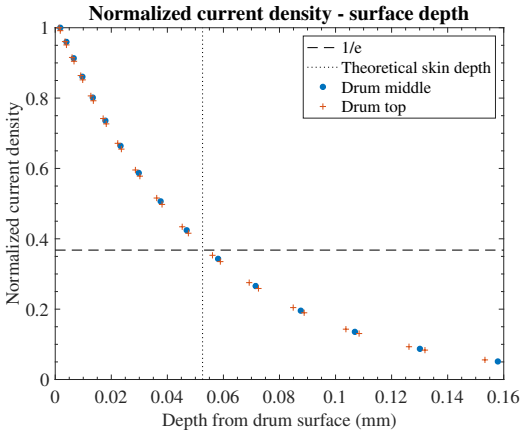

Figure 4.7: Normalized current density from the surface depth.

Table 4.5: Global steady-state thermal simulation results for the Test scenario and the Aggregate Stream Scenario.

	Test scenario	Aggregate stream scenario
Minimum drum temperature (°C)	67.0	24.9
Maximum drum temperature (°C)	101.0	184.2
Aggregate outlet temperature (°C)	-	166.0
Electrical losses/heating power (W)	309.90	2244.3
Heat transfer to aggregate (W)	-	1642.6
Heat loss to outside world (W)	309.90	596.7
Heater efficiency (%)	-	73.2
Total efficiency (%)	-	71.9

Figure 4.9a plots the surface temperature along the length of the drum. The observations discussed in the previous paragraph are again clearly visible. In the middle 20 cm of the drum, there is a high-temperature region with relatively little temperature difference. Moving away from the middle, the temperature drops nearly linearly, until it flattens out at the ends. The approximately linear temperature change and corresponding nearly constant temperature gradient between the middle and the end of the drum is an effect of the conduction within the drum, which reaches a steady state once a constant temperature gradient is achieved. Furthermore, the symmetric temperature pattern arises because there is no airflow in the drum, meaning there can be no temperature bias in the flow direction.

This symmetric temperature profile with the highest temperature in the middle is not the most desirable for a heat exchanger. Ideally, the temperature would be lowest at the barrel inlet and highest towards the barrel outlet to maximize the temperature difference between the drum and the aggregate, leading to maximum heat transfer. This might be achieved by using a coil that has staggered windings,

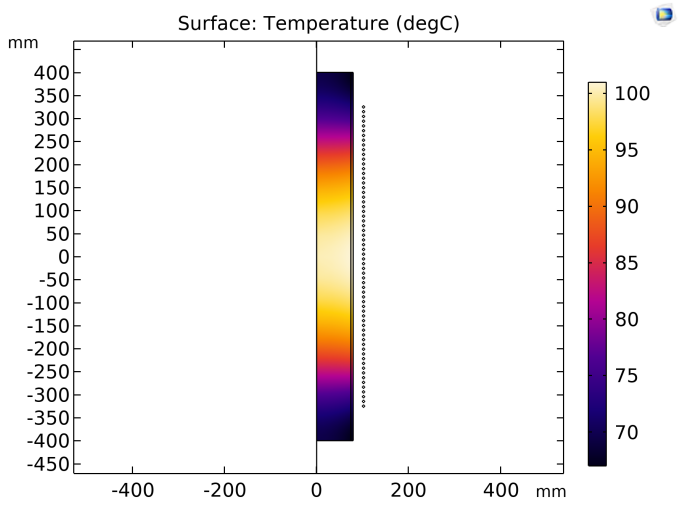

Figure 4.8: Temperature along the surface of the drum for the Test scenario.

with more windings being concentrated near the outlet and less near the inlet.

Figure 4.9a shows the heat flux from the drum to the outside world. As discussed in Subsection 4.1.2, all losses towards the outside world are modelled to occur through convection and radiation with respectively a constant heat transfer coefficient h and a constant emissivity ϵ. Because of this, the heat flux is determined by the temperature difference between the drum surface and the outside world and the heat flux graph follows the temperature graph very closely.

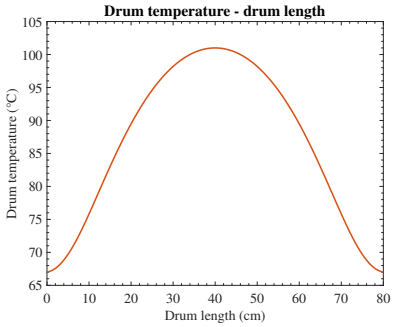

(a) Surface temperature along the length of the drum.

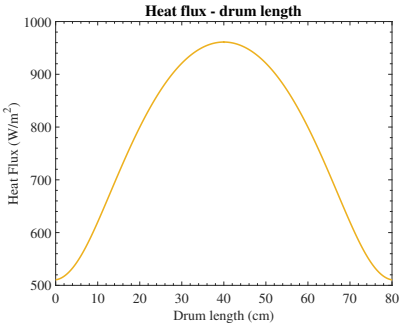

(b) Heat flux from drum surface to outside world along the length of the drum.

Figure 4.9: Drum temperature and heat flux to the outside world along the drum length.

The global thermal results for the steady-state simulation of the Aggregate stream scenario can be found in Table 4.5. The drum temperature varies between

24.9 °C and 184.2 °C, while the aggregate temperature temperature at the drum outlet is 166.0 °C. The temperature profile of the drum for the Aggregate stream scenario is shown in Figure 4.10. It can be seen that the drum temperature and aggregate temperature increase steadily along the length of the drum. The aggregate temperature at the ends of the drum is mostly homogeneous in the radial direction. However, in the middle of the drum, the aggregate temperature varies radially, which can be explained by the fact that the heat generation in the drum is higher in the middle than towards the ends.

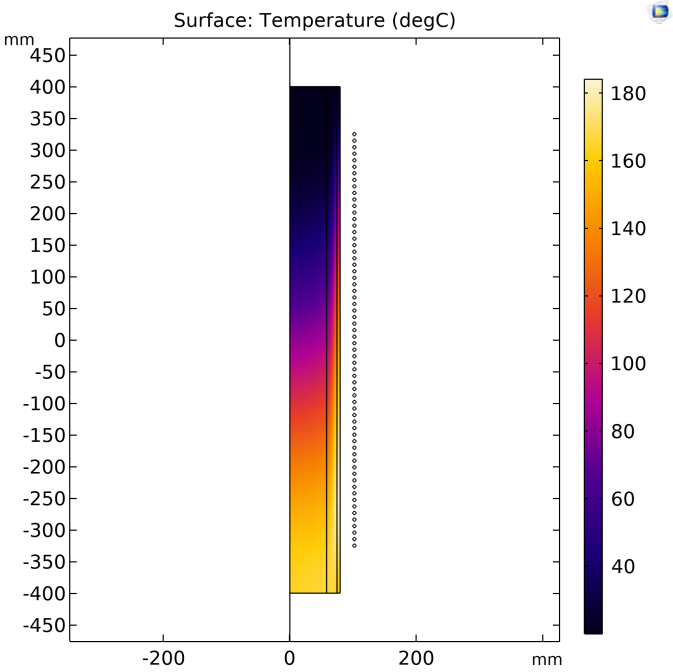

Figure 4.10: Temperature along the surface of the drum with aggregate flowing through it.

The temperature of the drum surface and the aggregate as a function of the length of the drum is more clearly shown by Figure 4.11. The middle of the centre of the aggregate stream was taken as the reference point for this graph. Both the drum and aggregate undergo only a small temperature increase in the first section of the drum which is not covered by the coil. Once the coil is reached, the drum temperature rises rapidly and the aggregate follows, its temperature rising as it is conductively heated through contact with the drum. In the second half of the drum, the drum and aggregate temperatures increase at nearly the same rate, until the end of the coil is almost reached. At the outlet, the drum is not actively heated anymore and it can only receive heat by conduction from the middle or lose heat to the outside world and the aggregate. The drum surface temperature thus reaches its peak and starts dropping, while the aggregate temperature stabilizes. Finally, the heat transfer

between the drum and the aggregate ends as the drum temperature drops under the aggregate temperature, because of its losses to the outside world.

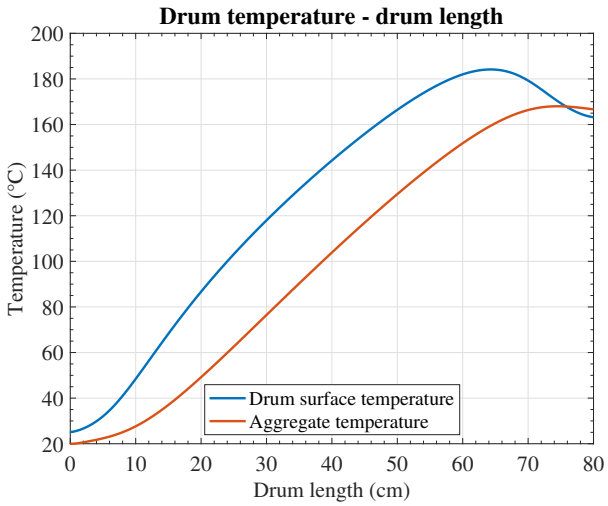

Figure 4.11: Temperature along the surface of the drum with aggregate flowing through it.

It can be read in Table 4.5 that the steady state heat transfer to the aggregate is 1642.6 W, while the heat loss to the outside world is 595.7 W. This results in a heater efficiency of 73.2% while the total efficiency is 71.9%. These efficiency scores are adequate, although not ideal.

The heat flux between the drum and the aggregate, and between the drum and the outside world is shown in Figure 4.12. The heat transfer from the drum to the aggregate rises within the first 20 cm, as the temperature difference between the drum inlet and the aggregate becomes larger. In the middle section, the heat transfer stabilizes but starts decreasing slowly as the heat loss to the outside world increases, until it drops rapidly within the last 20 cm of the drum. At the drum outlet, the heat flux reverses direction and the drum absorbs heat from the aggregate. Note that the point at which the drum starts absorbing heat from the aggregate does not exactly line up with the point at which the drum temperature equals the aggregate temperature in Figure 4.11, since there the outside drum surface is considered, while the heat transfer between the drum and the aggregate occurs to the inner surface, which has a slightly different temperature. The heat transfer from the aggregate to the drum is very undesirable, as it lowers the overall efficiency and is the exact effect for which the drum has been designed. Finally, because the model assumes that the aggregate forms a layer along the drum wall instead of a single stream at the bottom of the drum, the model likely overestimates the magnitude of heat transfer towards the aggregates and the heater efficiency.

Predictably, the loss to the outside world follows the drum surface temperature. The loss heat flux is notably much lower than the heat flux towards the aggregate for

nearly the full length of the drum, demonstrating the heater's adequate efficiency. The losses could be strongly reduced by thermally insulating the outside surface of the drum.

Figures 4.11 and 4.12 show that neither the heat flux nor the temperature is constant over the length of the drum. This indicates the limited use of an analytical approach for calculating the drum's thermal behaviour, as analytical equations assume constant temperature or constant heat flux as the boundary conditions of a problem. Therefore, the strength of the numerical approach is underscored.

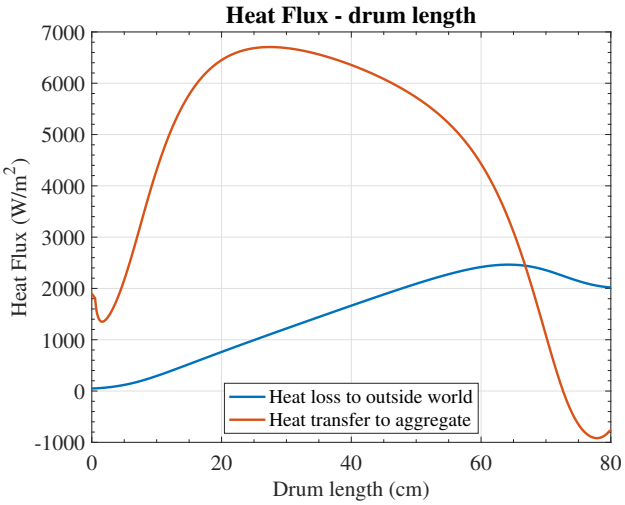

Figure 4.12: Temperature along the surface of the drum with aggregate flowing through it.

4.3. CONVERTER MODEL DESCRIPTION

The resonant converter is modelled in Simulink, a block diagram-based modelling tool. The Simscape library was used to simulate the electrical circuit.

The Simulink model is shown in Figure 4.13 and consists of a DC voltage source, DC Voltage source inductance, a DC capacitor, MOSFETs, gate signal blocks which drive the MOSFET, an inductor, a resistor, and a capacitor. The DC voltage source and the DC voltage source inductance together simulate the DC power supply, which serves as an input to the resonant inverter. In the MOSFET block one can set the drain-source resistance, the off-state conductance and the threshold voltage. These values were taken from the MOSFET data sheet. The parameters are used to accurately model the switch timing.

The Simulink model was used to predict the current and voltage waveforms that would be produced in the tests. Therefore, the inductance, capacitance, and resistance had to be accurately modelled. The inductance is taken from the

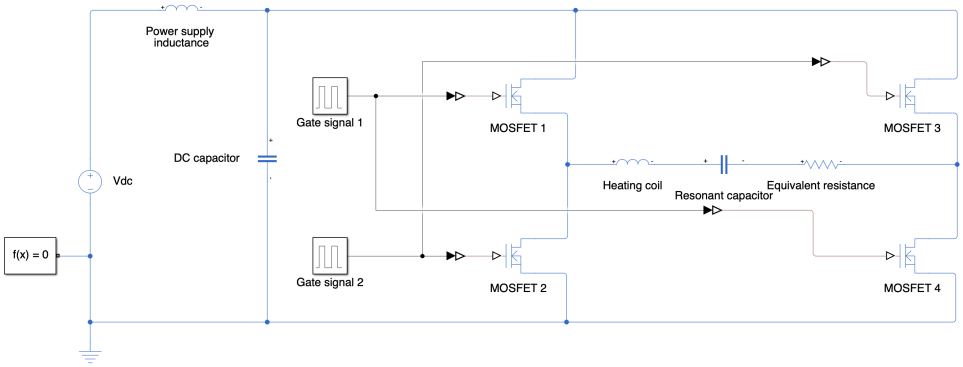

Figure 4.13: Model of the resonant converter in Simulink. The measurement blocks are not shown.

inductance measurement discussed in Section 5.2.1. At f = 10 kHz it was measured to be L_r = 126.72. The capacitance is C = 2.0 μF. Finally, the equivalent resistance was found by dividing the coil power by the square of the RMS current. In the design phase, the coil power was taken from COMSOL. After the tests were completed, there was measurement data available for the power and current values. For the measured coil power P = 274.09 W and measured RMS current I_{rms} = 6.16 A, the equivalent resistance is R = 7.23 Ω.

The model results are discussed as part of the analysis of the electrical test results in Section 5.2.2.

5

TESTING

A test setup of the aggregate induction heater was built to serve as a proof of concept and to confirm the validity of the electrical and thermal models. The complete mockup consists of the heater and an electrical power supply. The electrical and thermal behaviour of the device is measured to validate the models of the heater and the power supply. The first section of this chapter will discuss the test setup, the second section the electrical results and the third section of the chapter will discuss the thermal results.

5.1. TEST SETUP

The test setup is shown in Figure 5.1. It consists of the heater (A), the resonant capacitors (B), the inverter (C), the control board (D) and the H-bridge power supply (E). The oscilloscope (F) is used to measure the waveforms of the circuit voltage and current.

5.2. ELECTRICAL MEASUREMENTS

The electrical measurements consist of the impedance analysis of the heater, an analysis of the voltage and current waveforms and the calculation of the coil power.

5.2.1. COIL PROPERTIES

The inductance and resistance of the coil were measured for different frequencies with an impedance analyser. The measured inductance was used to determine the necessary capacitance to create a resonant circuit with resonant frequency $f = 10$ kHz, as was discussed in depth in Section 3.4. Furthermore, the measurements were used as the input for the Simulink model of the resonant converter. The resistance and inductance graphs are shown in Figure 5.2.

Coil resistance is proportional to the frequency, as shown by Figure 5.2a. This is expected, as the skin and proximity effect losses increase with a rising frequency. However, the measured resistance is significantly lower than the COMSOL model resistance noted down in Table 4.4. This is likely because the coil is modelled as

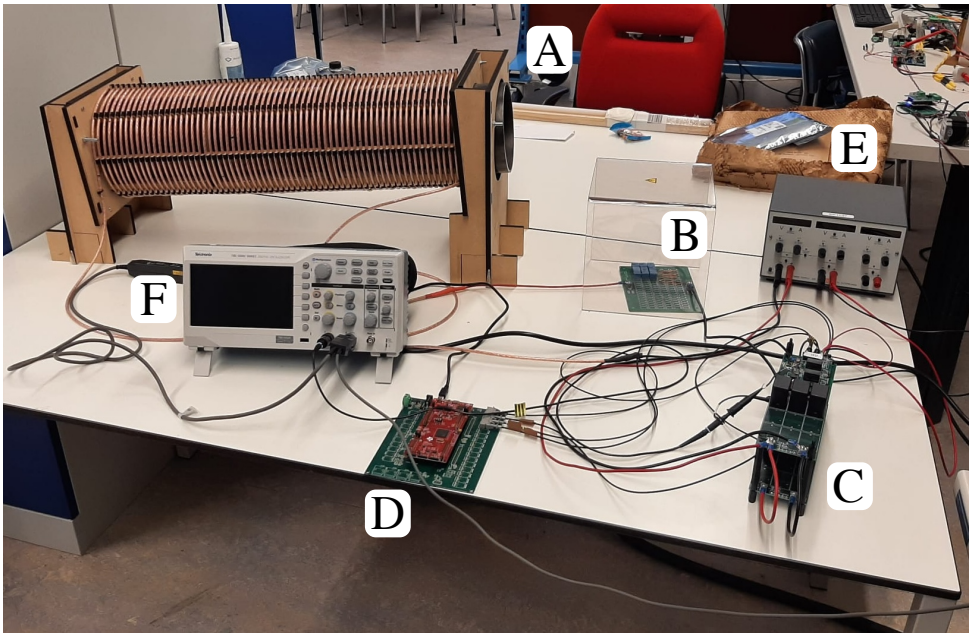

Figure 5.1: The test setup consists of the heater, the H bridge, the controller, the resonant capacitors and the H-bridge power supply. The oscilloscope is used to measure the voltage and current waveforms. The heater power supply is not pictured.

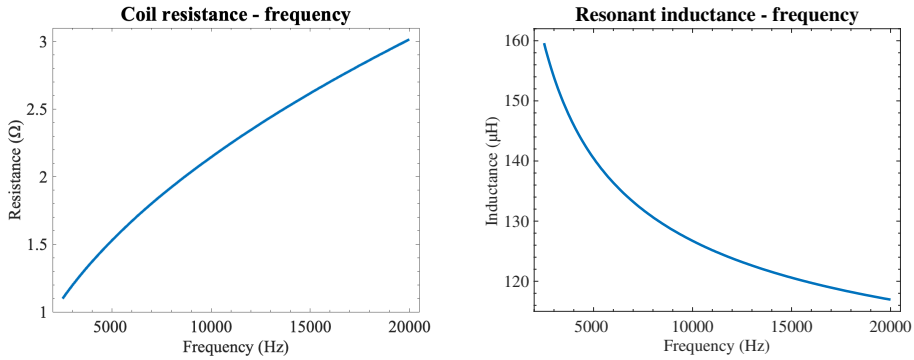

(a) Coil resistance as a function of frequency. (b) Coil inductance as a function of frequency.

Figure 5.2: Coil properties as a function of frequency.

a solid wire in COMSOL, while in actuality it is made of a Litz wire, which has a significantly lower AC resistance.

Figure 5.2b show that the coil inductance is inversely proportional to the frequency. This could be due to multiple factors. Z decrease in steel permeability at higher

frequencies has been observed in other research. A possible mechanism is that the magnetic domain walls cannot reorientate quickly enough to follow the changing external magnetic field, lowering the material's magnetisation. [47]

5.2.2. ELECTRICAL WAVEFORMS

The H-bridge voltage and coil current waveforms were measured to determine the electrical characteristics of the system. The voltage was measured using a simple hook probe and the current was measured with a current clamp, both of which were connected to an oscilloscope.

Because the system was designed to have resonant frequency f_r = 10 kHz, the first test was run for V = 50.2V and f = 10 kHz. Figure 5.3a displays a screenshot of the oscilloscope measurements: the coil current is shown in blue while the H-bridge voltage is shown in yellow. Immediately, it is clear from the current waveform that the switching frequency is higher than the resonant frequency of the RLC circuit. The current tries to follow a sinusoid according to the circuit's resonant frequency, but the voltage switches polarity before the current can complete its half cycle and reach zero, creating a jagged and non-sinusoidal current wave. Such a current is undesirable because it will lead to higher switching losses and inefficiency.

The resonant frequency of the RLC circuit was estimated by changing the switching frequency of the H-bridge and checking the shape of the current waveform. By this method, it was found that the resonant frequency is close to f = 8 kHz. Figure 5.3b shows the measurements for f = 8 kHz. The current has a nearly sinusoidal shape and switching happens when the current is close to zero. The lower switching frequency can be seen by the larger width of the voltage square wave.

The circuit was designed to have a resonant frequency of 10 kHz but instead the resonant frequency is 8 kHz, 20% lower than the design intention. This means that either the inductance or the capacitance is higher than expected. The capacitance-voltage and capacitance-frequency characteristics of the capacitor are known from the datasheets. The capacitors were chosen because of their stable value at high voltages and frequencies. Furthermore, the capacitance of a small amount of capacitors was measured and found to be the same as the value on the datasheet. Because of this, the capacitance is not expected to be significantly higher. The inductance of the coil and drum are known as a function of frequency, as shown in Figure 5.2b. However, the impedance measurement is done at a low voltage. At a higher power, the magnetic field will be stronger and the steel will move into a higher and steeper region of the the BH-curve. The steel's permeability is thus higher, which increases the inductance and lowers the resonant frequency. Note that the steel is not magnetically saturated, since that would lead to lower inductance and higher resonant frequency.

Assuming that f_r = 8000 kHz and C = 2 μF, the inductance is be L = 197.9 μH. The converter behaviour was simulated using these values. The simulated and measured coil current are plotted in Figure 5.4 and the simulated and measured coil voltage are plotted in Figure 5.5.

The simulated current is in good accordance with the measured current. The

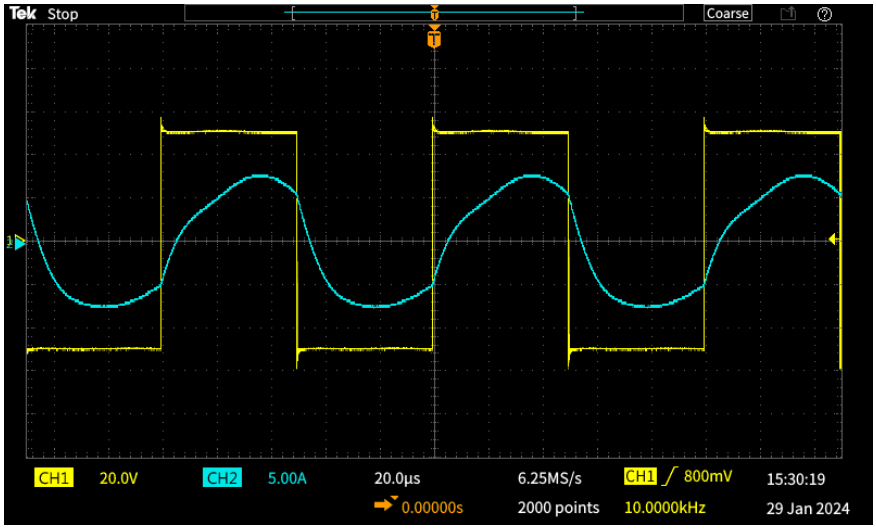

(a) Current and voltage waveforms for 50.2V and 10 kHz captured by the oscilloscope.

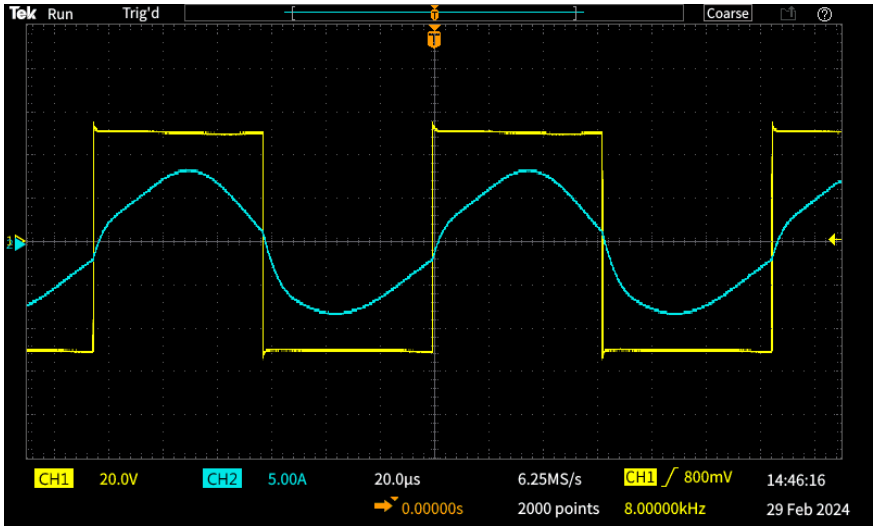

(b) Current and voltage waveforms for 50.2V and 8 kHz captured by the oscilloscope.

Figure 5.3: H-brdige voltage and coil current waveforms for a switching frequency of 10 kHz and a switching frequency of 8 kHz.

simulation has the same amplitude and reaches the same value at the switching point. However, the simulated current has fewer harmonics and more closely follows a sine wave while it is rising toward its maximum value. Remarkably, the current's amplitude changes between positive and negative half-cycles, being 8.7 A and -7.7 A respectively. This indicates a directional bias of the circuit's equivalent resistance.

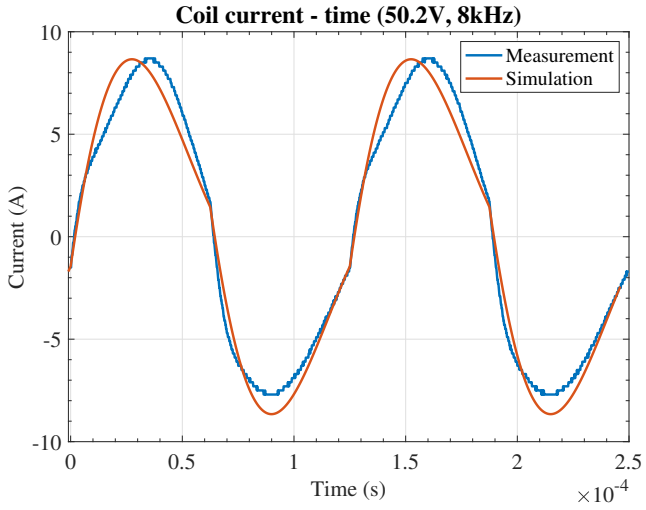

Figure 5.4: The current waveform of the electrical measurement and the simulation for 50.2V and 8kHz

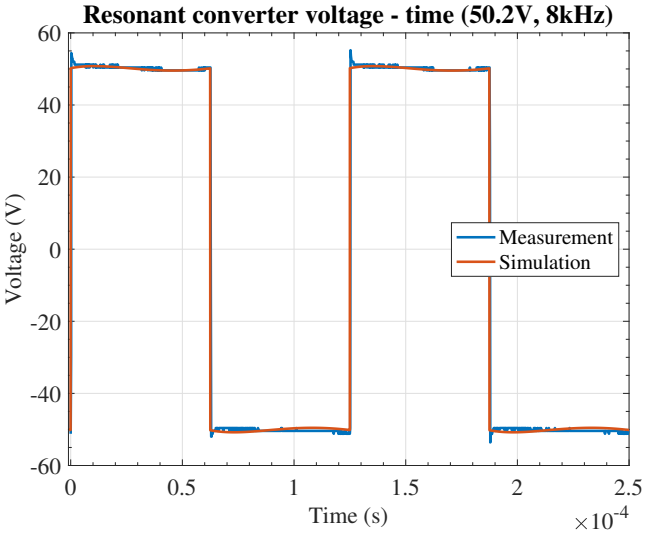

Figure 5.5: The voltage waveform of the electrical measurement and the simulation for 50.2V and 8kHz

The simulated voltage and the measured voltage are nearly identical. However, the measured voltage shows small spikes when switching, which is to be expected when using MOSFETs. The Simulink model does not simulate such spikes as the model is more idealized.

5.2.3. ELECTRICAL POWER

By numerically integrating the measured voltage and current, it is found that the average coil power for one switching cycle is 274.09 W. The simulated coil power of P_{coil} = 314.76 is therefore 14.8% higher than the measured power.

Since the modelled power is significantly higher than the measured value, some property that determines the coil power are not simulated correctly. The coil power is determined by its electrical input, by the geometry of the coil and the drum, and by the material properties of copper and steel. The input current in the model was taken directly from the measured value and the geometry of the setup was checked carefully, meaning the material properties are the most likely cause of the overestimated coil power. Since copper is a pure material, it can be assumed that the standard modelling values for its electrical conductivity and magnetic permeability are highly representative of the actual material value. In contrast, the electrical conductivity and magnetic permeability values for different types of steel are more varied. Since the steel pipe used as the drum in the test setup is of an unknown steel type, the assumptions made about the value of its material properties can introduce inaccuracies in the model. As explained in Section 4.1.2, the magnetic permeability of steel is modelled as an average BH-curve in COMSOL. The derivative of the linear part of this curve is taken as a value for the relative permeability of steel and equals μ_r = 2118.5. This estimation for relative permeability was used to determine the skin depth discussed in Section 4.2.1. However, reported typical values for the relative permeability of carbon steel range are in the order of μ_r = 100. [48] Therefore, it is likely that the model strongly overestimates the relative permeability of the steel pipe.

It would be best to measure the permeability of the steel in a laboratory setup. Instead, the relative permeability of the steel pipe has been approximated by varying the value in the simulation and checking the coil power. It is important to note that this is not a scientifically rigorous way to estimate the permeability and therefore the results found by using the updated relative permeability are of limited use. Other BH-curves which are available in COMSOL and have lower permeability and saturation values were not used because of time constraints and because the right COMSOL tooling was not available to convert these curves into the correct format.

Through iteration it was found that for μ_r = 1500, P_{coil} = 272.4 W. Because this is much closer to the actual coil power, a simulation done with this assumption can provide more insight into the thermal aspects of the model. Therefore, in the following section, the temperature measurements will be compared to both the model with the original average BH-curve and to a model with μ_r = 1500. It should be noted that μ_r = 1500 is still high for carbon steel and more in the neighbourhood of stainless steel, for which μ_r ranges from 750 to 1800. [48]

5.3. THERMAL MEASUREMENTS

The following experiment was done to compare the thermal behaviour of the induction heater test setup to the thermal behaviour of the induction heater model. The test consisted of turning on the induction heater and measuring the drum temperature at the inlet and the middle of the drum every 30 seconds. The input voltage of the resonant converter was 50.2V and the switching frequency was 8000 Hz. The amplitude of the resulting current was 8.7 A. The temperature was measured using thermocouples. One thermocouple was placed in the middle of the drum, as shown in Figure 5.6a, and one thermocouple was placed at the drum outlet, as shown in Figure 5.6b. Two other thermocouples were used to establish the reference temperature. The reference measurements came out an average of 21.3°C with a standard deviation of 0.2°C and an average of 21.6°C with a standard deviation of 0.2°C.

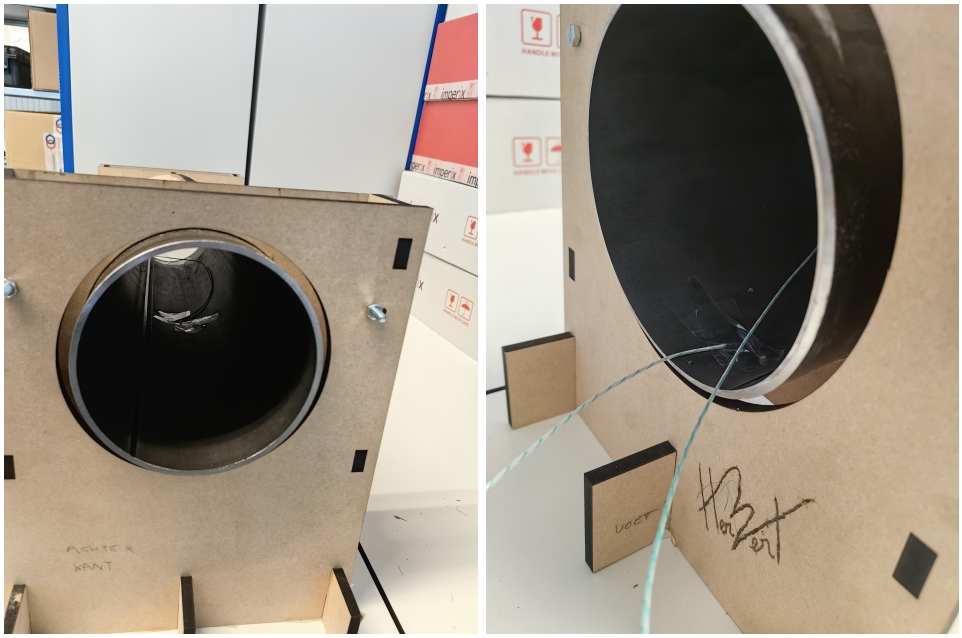

(a) Temperature measurement point at the drum middle.

(b) Temperature measurement point at the drum outlet.

At the start of the test, the power is turned on and a current starts running through the coil. As discussed previously, an electrical steady state is reached within a second. From that moment on, a steady heating power is generated in the drum, increasing the temperature of the drum over time. Every 30 seconds, the temperature measured by the thermocouples is recorded. The experiment was run for 5760 seconds in total, which equals 96 minutes or about an hour and a half. A transient study was run with the COMSOL model described in Chapter 4, simulating the state of the drum heater in the Test scenario every 30 seconds for 8760 seconds. Figure

5.7 displays the temperature plots from the test and from the simulation in the same graph. Furthermore, Table 5.1 shows the rise time (the time at which the temperature has reached 90% of its final value) of the temperatures for the test and the simulation.

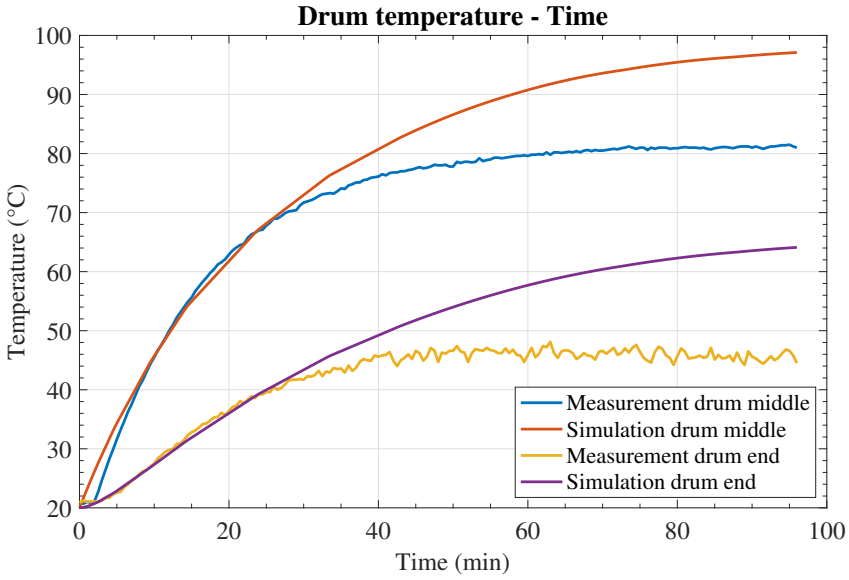

Figure 5.7: Drum temperature for the test setup and the simulation as a function of time when the heater is operated at 50.2V and 8 kHz. The steel permeability is defined as an average BH-curve.

The final temperatures measured in the test are lower than those simulated by the COMSOL model. The measured final temperature of the drum middle is 81.0°C while the simulated value at $t = 5860$ is 97.1°C, which is 21.1% higher than the measurement. The measured temperature of the drum middle is 44.5°C while the simulated value at $t = 5860$ is 64.1°C, which is 44.0% higher than the measurement. The measured temperature difference between the middle and the end is 36.5°C while the simulated difference is 32.7, a 10.4% difference. It should be noted that the temperatures and t = 5760 *s* are not the steady state temperatures for the simulation. The simulated steady state temperature for the drum middle is 98.4°C and for the drum end it is 65.6°, they are both reached after approximately 2 hours and 30 minutes. However, this difference does not influence the analysis.
Furthermore, the test setup reaches a steady state faster than is predicted by the model. The rise time from the drum middle in the measurement is 29.8 minutes while for the simulation the rise time is 47.2 minutes. The measured rise time for the outlet is 33.0 minutes but for the simulation, it is 59.4 minutes. These results indicate that the model is flawed and can be improved further, although the final temperature and rise time are within the correct order of magnitude.

As discussed in the previous section, the model overestimates the coil power and it is a reasonable assumption that the modeled permeability of the steel pipe is higher than its actual permeability. The high coil power value results in a higher heating power for the drum and therefore a higher final temperature. If the relative permeability is modelled as μ_r = 1500, the simulated coil power is nearly equal to the measured coil power. Based on this assumption, the thermal behaviour of the model can be investigated further. However, it is important to note that this is not a scientific way of determining the relative permeability. The temperature graph for the simulation with constant permeability and a more representative coil power is shown in Figure 5.8

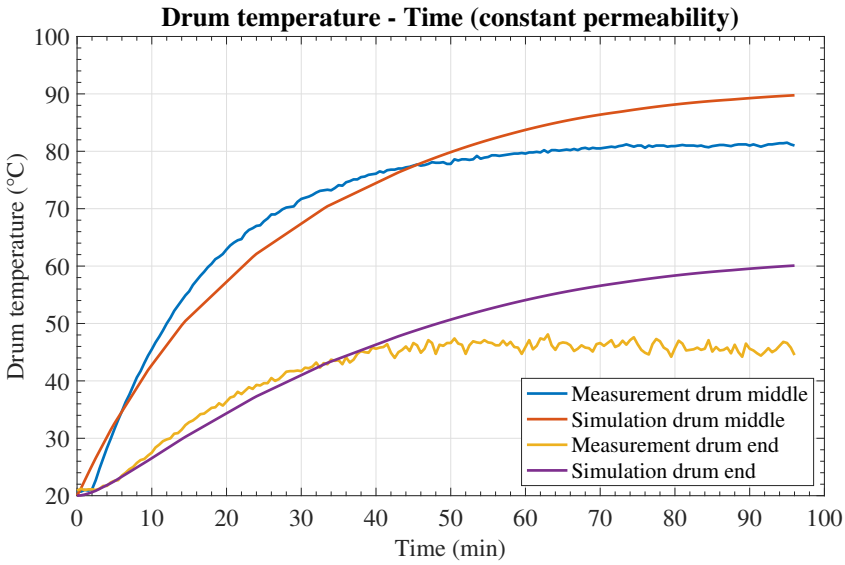

Figure 5.8: Drum temperature for the test setup and the simulation as a function of time when the heater is operated at 50.2V and 8 kHz. The steel permeability is constant μ_r = 1500.

The simulated final temperature for the drum middle is 89.8°C, 10.9% higher than the measured temperature, and the simulated final temperature for the drum end is 60.1°C, 35.1% higher than the measured value. The difference in temperature between the inlet and the middle is 29.1°C, 20.3% higher. Again, the temperatures and t = 5760 s are not the steady state temperatures for the simulation. The simulated steady state temperature for the drum middle is 91.1°C and for the drum end it is 61.6°, they are both reached after approximately 2 hours and 45 minutes. Finally, the rise times have changed very little. The rise time for the drum middle temperature is 47.4 minutes and for the drum end it is 59.9 minutes.

The simulated temperatures are still higher than the measured temperatures, although they have gotten closer to the measured temperatures due to the decrease

Table 5.1: Rise time for test and the simulation with the BH-curve model and the constant μ_r model.

	Drum middle	Drum end
Rise time Test (min)	29.8	33.0
Rise time Simulation (BH-curve model) (min)	47.2	59.4
Rise time Simulation (constant μ_r model) (min)	47.4	59.9

in simulated coil power. Specifically, the temperature in the middle of the drum is now modelled with an acceptable accuracy. At the same time, the temperature gradient in the simulation has become lower, which is less accurate. In the below paragraphs, the possible behaviour of the heater and the possible problems with the model are analyzed.

There are multiple possible reasons as to why the simulated temperatures at t = 5760 s are still higher than the measured values.

Firstly, the simulated heating power might still be too high. This is supported by the fact that both the temperature in the drum middle and at the drum end are higher than the measurement. Although the coil power is now accurate in the simulation, the conversion of energy between the coil and eddy current in the drum might be less efficient than modelled.

Secondly, the heat transfer coefficient for losses through natural convection and the emissivity for heat loss through radiation might be higher in the test setup than in the simulation. This could be the case, since a higher heat transfer coefficient and emissivity would lead to the same steady-state losses for a lower surface temperature. However, this does not seem likely. Although the heat transfer coefficient for natural convection is prone to inaccuracy, it is expected to be lower, not higher, given the geometry of the test setup. The coil and wooden support structure cover large sections of the drum. This creates an obstacle for the air to flow away from the drum, thereby limiting the effectiveness of convection. This would result in a lower heat transfer coefficient in comparison to an uncovered steel cylinder. As for radiation, the emissivity of the drum is assumed to be equal to that of oxidized steel: $\epsilon = 0.79$. This assumption was made because the steel pipe has a rather matte and imperfect surface. However, it is unlikely that the actual emissivity of the pipe, which does not show traces of rust, would be as high or higher than that of oxidized steel. Furthermore, the heat that is radiated away by the drum surface will be partially reflected back to the drum by the coil and its gleaming sheath, heating the drum further. Radiation will also be absorbed by the coil and the wooden supports which would lead to a slight increase in the temperature of the surrounding area. Because of this, it would seem that the actual losses are lower, not higher than found in the simulation.

The only situation for which losses would be higher in the test than in the simulation would be for radiation from the inside surface of the drum at the inlet and outlet. Since radiation flows away in all directions from each point on a surface,

radiation originating from the inside surface of the drum would be able to escape from the drum through the inlet and outlet. This loss mechanism has not been modelled and is specific to the ends of the drum, which show the highest difference in temperature to the test. Therefore, this simplification might contribute to the higher temperatures of the drum end.

Thirdly, the thermal conductivity of the steel might be different than assumed in the simulation. The temperature difference between the drum inlet and drum end is higher in the test than in the simulation. This could be explained by higher localized losses at the drum ends, as discussed in the previous paragraph. However, this also points towards a lower thermal conductivity. A less thermally conductive material would have a larger temperature gradient, especially when heat generation is concentrated near the middle of the workpiece such as in the drum. Simulating with a lower thermal conduction results in a lower drum end temperature and more representative temperature difference, but also leads to a higher drum temperature in the middle. It should be noted that such low thermal conductivity values are not representative of carbon steel and are more typically found in stainless steels, for which $k = 16.0 W/(mK)$.

The test setup reaches a lower temperature for the drum middle and the drum end than in the simulation, but has a higher temperature difference between the two. Based on the analysis above, it is proposed that this is due to a combination of lower overall heating power, lower thermal conductivity, and higher localized losses at the drum ends. The lower heating power is assumed to be due to a lower relative permeability of the steel in comparison to the model. The model improvements and research improvements that follow from this analysis will be discussed in Chapter 6: Conclusion.

6

Conclusion

This thesis focused on the design of an induction heater for asphalt aggregate. A basic design was created based on a drum surrounded by a large coil powered through a resonant converter. Models of the drum heater and the power converter were created to predict the machine's behaviour and serve as a design aid. A scaled-down version of the heater was designed to experimentally validate the model results.

In the Introduction, the following research question is posed.

> **Main research question:** What is a suitable mechanical and electrical design for an induction heater for asphalt aggregate that can be implemented in an existing asphalt production process?

Two subquestions were investigated to answer the main research question.

> **Subquestion 1:** How can an induction heater for asphalt aggregate be modelled?

The induction heater behaviour can be simulated by using a two-dimensional axisymmetric model in COMSOL Multiphysics. The resonant converter can be modelled using a block diagram model in Simulink.

The COMSOL model was able to predict the temperature in the middle of the drum fairly accurately. The COMSOL model quality is dependent on the accurate description of the material properties. If possible, the magnetic and thermal properties of steel should be measured beforehand. This would improve the simulation of the heat generation in the drum wall.

The COMSOL model can be improved further by describing the radiation losses in more detail. Specifically, the reflection and absorption of radiation by the coil could be added. Furthermore, modelling the localized radiation losses from the inner drum surface could make it more accurate.

Finally, a three-dimensional model is likely to predict aggregate behaviour more accurately.

The Simulink model was able to predict the electrical waveforms with great accuracy. The quality of the modelling of the coil current amplitude was dependent on the resistance value. Yet, the simulated current and voltage waveforms strongly resembled the measured waveforms.

Subquestion 2: How can the model be experimentally verified?

The model was experimentally verified by building a scaled down version of the aggregate induction heater and measuring the coil current, converter voltage, and the drum temperature in the middle and at the outlet.

The experiment could have been improved by measuring the magnetic field and measuring the skin depth. These tests would give insight into drums' magnetic behaviour and heat generation. Furthermore, an aggregate sample could have been heated up in a test, to verify the outcomes of the Aggregate stream scenario simulation.

By answering these subquestions, the main research question can be answered. A heater constructed from a drum with a coil wrapped around it which is powered by a resonant converter is a suitable design to heat asphalt aggregates. The design can likely be improved by increasing the contact area between the drum and the aggregate e.g. through the use of multiple channels, by insulating the drum to reduce heat loss, and by creating a stronger temperature gradient on the drum surface to ensure highly efficient heat transfer along the entire drum length.

A design process based on COMSOL and Simulink models could be effective if the material properties of the drum are accurately described e.g. by using high quality data from the material supplier or by experimentally measuring the properties. The influence of material properties on the accuracy of the model indicates that the design process for a full-sized heater should involve iteration between the model and experiments.

The creation of COMSOL and Simulink models that describe the aggregate induction heater, and the construction of a scaled-down heater to experimentally verify the model results are useful steps towards the realization of an industrial induction heater that can heat and dry aggregates without emitting greenhouse gasses.

BIBLIOGRAPHY

[1] S. Madeddu, F. Ueckerdt, M. Pehl, J. Peterseim, M. Lord, K. A. Kumar, C. Krüger, and G. Luderer. "The CO $_2$ reduction potential for the European industry via direct electrification of heat supply (power-to-heat)". In: *Environmental Research Letters* 15.12 (Dec. 2020), p. 124004. ISSN: 1748-9326. DOI: 10.1088/1748-9326/abbd02. URL: https://iopscience.iop.org/article/10.1088/1748-9326/abbd02 (visited on 05/02/2023).

[2] C. Hoffmann, M. Van Hoey, and B. Zeumer. *Decarbonization challenge for steel: Hydrogen as a solution in Europe*. Tech. rep. McKinsey and Company, Apr. 2020, p. 12. URL: https://www.mckinsey.com/industries/metals-and-mining/our-insights/decarbonization-challenge-for-steel (visited on 03/07/2023).

[3] J. Cresko. *Industrial Decarbonization Roadmap*. English. Tech. rep. Washington, DC 20585: U.S. Department of Energy, Sept. 2022, p. 241. URL: https://www.energy.gov/sites/default/files/2022-09/Industrial%5C%20Decarbonization%5C%20Roadmap.pdf (visited on 05/29/2023).

[4] M. Wei, C. A. McMillan, and S. De La Rue Du Can. "Electrification of Industry: Potential, Challenges and Outlook". en. In: *Current Sustainable/Renewable Energy Reports* 6.4 (Dec. 2019), pp. 140–148. ISSN: 2196-3010. DOI: 10.1007/s40518-019-00136-1. URL: http://link.springer.com/10.1007/s40518-019-00136-1 (visited on 05/02/2023).

[5] P. Sorknæs, R. M. Johannsen, A. D. Korberg, T. B. Nielsen, U. R. Petersen, and B. V. Mathiesen. "Electrification of the industrial sector in 100% renewable energy scenarios". en. In: *Energy* 254 (Sept. 2022), p. 124339. ISSN: 03605442. DOI: 10.1016/j.energy.2022.124339. URL: https://linkinghub.elsevier.com/retrieve/pii/S0360544222012427 (visited on 05/02/2023).

[6] "Construction Of Hot Mix Asphalt Pavements". English. In: *Construction Of Hot Mix Asphalt Pavements*. Second. Manual Series 22. Lexington, Kentucky: Asphalt Institute, 2001. ISBN: 978-1-934154-14-4.

[7] C. Oliveira and C. Xavier Silva. *Decarbonisation options for the Dutch asphalt industry*. English. Tech. rep. 4791. The Hague: PBL Netherlands Environmental Assessment Agency and TNO Energy Transition, 2022, p. 47. URL: https://www.pbl.nl/en/publications/decarbonisation-options-for-the-dutch-asphalt-industry (visited on 04/17/2023).

[8] M. L. Swanson. "Apparatus and method for dryer performance optimization system". US20140373385A1 (Chattanooga, Tennessee). July 2016.

[9] J. D. Brock, G. L. Catlett, and M. L. Swanson. “Method and apparatus for making asphalt concrete using aggregate material from a plurality of material streams”. US20150029809A1 (Chattanooga, Tennessee). Jan. 2015.

[10] Abra Service. *Mixer drum*. Nov. 2021. URL: https://www.abraservice.com/en-us/industries/asphalt-plants.

[11] S. Lupi. *Fundamentals of electroheat: electrical technologies for process heating*. Cham, Switzerland: Springer, 2017. 620 pp. ISBN: 978-3-319-46015-4 978-3-319-46014-7.

[12] A. Ibrahim and S. MacIntyre. “Failure analysis of Incoloy 800 water immersion heating element”. In: *Green Technology, Resilience, and Sustainability* 3.1 (Oct. 18, 2023), p. 5. ISSN: 2731-3425. DOI: 10.1007/s44173-023-00014-6. URL: https://link.springer.com/10.1007/s44173-023-00014-6 (visited on 08/17/2024).

[13] C. J. Erickson. *Handbook of electrical heating for industry*. Piscataway, NJ: IREE Press [u.a.], 1995. 629 pp. ISBN: 978-0-7803-0420-8.

[14] F. Gulisano and J. Gallego. “Microwave heating of asphalt paving materials: Principles, current status and next steps”. In: *Construction and Building Materials* 278 (Apr. 2021), p. 121993. ISSN: 09500618. DOI: 10.1016/j.conbuildmat.2020.121993. URL: https://linkinghub.elsevier.com/retrieve/pii/S0950061820339970 (visited on 08/16/2024).

[15] L. Zhang, Z. Zhang, W. Yu, and Y. Miao. “Review of the Application of Microwave Heating Technology in Asphalt Pavement Self-Healing and De-icing”. In: *Polymers* 15.7 (Mar. 29, 2023), p. 1696. ISSN: 2073-4360. DOI: 10.3390/polym15071696. URL: https://www.mdpi.com/2073-4360/15/7/1696 (visited on 08/16/2024).

[16] HI-TECH. *Mineral Insulated Trace Heating Cable*. Aug. 2023. URL: https://hi-techelements.co.za/products/trace-heating-elements.

[17] Gordak. *GORDAK 853 863 Heating Plate*. Aug. 2024. URL: https://nl.aliexpress.com/i/32998587919.html?gatewayAdapt=glo2nld.

[18] F. Gulisano, J. Crucho, J. Gallego, and L. Picado-Santos. “Microwave Healing Performance of Asphalt Mixture Containing Electric Arc Furnace (EAF) Slag and Graphene Nanoplatelets (GNPs)”. In: *Applied Sciences* 10.4 (Feb. 20, 2020), p. 1428. ISSN: 2076-3417. DOI: 10.3390/app10041428. URL: https://www.mdpi.com/2076-3417/10/4/1428 (visited on 08/17/2024).

[19] Radyne. *What Are The Advantages of Induction Brazing?* Aug. 2024. URL: https://www.radyne.com/blog-induction-brazing-advantages/.

[20] A. S. Mujumdar. *Handbook of Industrial Drying*. Third edition. Boca Raton (Fla.): CRC/Taylor & Francis, 2007. ISBN: 978-1-57444-668-5.

[21] Z. Pan and G. G. Atungulu. *Infrared heating for food and agricultural processing*. OCLC: 671655003. Boca Raton, FL: CRC Press, 2011. ISBN: 978-1-4200-9099-4.

[22] S. A. Aboud, A. B. Altemimi, A. R. S. Al-HiIphy, L. Yi-Chen, and F. Cacciola. “A Comprehensive Review on Infrared Heating Applications in Food Processing”. In: *Molecules* 24.22 (Nov. 15, 2019), p. 4125. ISSN: 1420-3049. DOI: 10.3390/molecules24224125. URL: https://www.mdpi.com/1420-3049/24/22/4125 (visited on 08/17/2024).

[23] W. B. Coe. “Apparatus and method for preparing asphalt and aggregate mixture”. US11186959B2 (Wrightwood, California). Aug. 2020.

[24] W. L. Hughes. “Induction heated rotary kiln”. US4931610 (Rapid city, South-Dakota). June 1989.

[25] N. Bhardwaj, S. Seethamraju, and S. Bandyopadhyay. “Decarbonizing rotary kiln–induction furnace based sponge iron production”. In: *Energy* 306 (Oct. 2024), p. 132516. ISSN: 03605442. DOI: 10.1016/j.energy.2024.132516. URL: https://linkinghub.elsevier.com/retrieve/pii/S0360544224022904 (visited on 08/17/2024).

[26] P. C. Sen. *Principles of electric machines and power electronics*. Third edition. Hoboken, New Jersey: John Wiley and Sons, Inc, 2014. ISBN: 978-1-118-07887-7.

[27] R. P. Feynman. *The Feynman lectures on physics. Volume 2: Mainly electromagnetism and matter*. eng. The new millennium edition, hardcover first published. New York: Basic Books, 2011. ISBN: 978-0-465-02416-2.

[28] D. Rommel, D. Di Maio, and T. Tinga. “Transformer hot spot temperature prediction based on basic operator information”. en. In: *International Journal of Electrical Power & Energy Systems* 124 (Jan. 2021), p. 106340. ISSN: 01420615. DOI: 10.1016/j.ijepes.2020.106340. URL: https://linkinghub.elsevier.com/retrieve/pii/S014206152030867X (visited on 09/26/2023).

[29] C. Lei, Y. Zhou, X.-Y. Gao, W. Ding, Y. Cao, H. Choi, and J. Won. “Fabrication of a solenoid-type inductor with Fe-based soft magnetic core”. en. In: *Journal of Magnetism and Magnetic Materials* 308.2 (Jan. 2007), pp. 284–288. ISSN: 03048853. DOI: 10.1016/j.jmmm.2006.06.002. URL: https://linkinghub.elsevier.com/retrieve/pii/S0304885306008948 (visited on 01/24/2024).

[30] N. Mohan, T. M. Undeland, and W. P. Robbins. *Power electronics: converters, applications, and design*. 2nd ed. New York: Wiley, 1995. ISBN: 978-0-471-58408-7.

[31] S. Zinn and S. L. Semiatin. *Elements of induction heating: design, control, and applications*. Palo Alto, Calif.: Electric Power Research Inst. [u.a.], 1988. ISBN: 978-0-87170-308-8.

[32] C. A. Tudbury. *Basics of Induction Heating*. New York: John F. Rider Publisher, Inc., 1960.

[33] B. Nacke, E. Baake, and S. Lupi, eds. *Induction heating: heating | hardening | annealing | brazing | welding*. eng. 1st edition. Edition heat processing. Essen, Germany: Vulkan Verlag, 2016. ISBN: 978-3-8027-3048-1 978-3-8027-2391-9.

[34] The Engineering ToolBox. *Water - Thermophysical Properties*. 2024. URL: https://www.engineeringtoolbox.com/water-thermal-properties-d_162.html.

[35] J. Muhlethaler. "Modeling And Multi-objective Optimization Of Inductive Power Components". PhD thesis. ETH Zurich, 2012.

[36] Deeter Electronics. *Litz Wire*. Sept. 2024. URL: https://www.deeterelectronics.com/product/litz-wire/litz-wire/.

[37] Ó. Lucía, A. Domínguez, H. Sarnago, and J. M. Burdío. "Induction Heating". In: *Control of Power Electronic Converters and Systems*. Elsevier, 2018, pp. 265–287. ISBN: 978-0-12-816136-4. DOI: 10.1016/B978-0-12-816136-4.00022-1. URL: https://linkinghub.elsevier.com/retrieve/pii/B9780128161364000221 (visited on 09/05/2024).

[38] D. Peinado, M. De Vega, N. García-Hernando, and C. Marugán-Cruz. "Energy and exergy analysis in an asphalt plant's rotary dryer". In: *Applied Thermal Engineering* 31.6 (May 2011), pp. 1039–1049. ISSN: 13594311. DOI: 10.1016/j.applthermaleng.2010.11.029. URL: https://linkinghub.elsevier.com/retrieve/pii/S1359431110005119 (visited on 08/18/2024).

[39] COMSOL Multiphysics developers. *Modeling Hysteresis Effects - solved with COMSOL Multiphysics 3.5a*. 2008.

[40] M. Olsson. *COMSOL 4.4: Magnetic Saturation Curves at your Fingertips*. https://www.comsol.com/blogs/comsol-4-4-magnetic-saturation-curves/. (Visited on 2013).

[41] *Granular Flows*. Vol. XIII. Institut Henri Poincaré. Paris, France, Nov. 2009, pp. 69–100.

[42] D. Fantin. "CFD-DEM Coupling for Systems of Fluid and Non-Spherical Particles". Available at: http://resolver.tudelft.nl/uuid:6ddce0bf-dc00-4f7a-bb07-040b9851a8e8. Master thesis. Delft University of Technology, Oct. 2018.

[43] A. Hobbs. "Simulation of an aggregate dryer using coupled CFD and DEM methods". en. In: *International Journal of Computational Fluid Dynamics* 23.2 (Feb. 2009), pp. 199–207. ISSN: 1061-8562, 1029-0257. DOI: 10.1080/10618560802680971. URL: https://www.tandfonline.com/doi/full/10.1080/10618560802680971 (visited on 05/01/2023).

[44] S. S. Hubbard, J. E. Peterson, E. L. Majer, P. T. Zawislanski, K. H. Williams, J. Roberts, and F. Wobber. "Estimation of permeable pathways and water content using tomographic radar data". In: *The Leading Edge* 16.11 (Nov. 1997), pp. 1623–1628. ISSN: 1070-485X. eprint: https://pubs.geoscienceworld.org/tle/article-pdf/16/11/1623/3069844/1623.pdf.

[45] M. J. Moran, H. N. Shapiro, D. D. Boettner, and M. B. Bailey. *Principles of engineering thermodynamics*. eng. Eighth edition, SI version. OCLC: 908412182. Singapore: Wiley, 2015. ISBN: 978-1-118-96088-2.

[46] COMSOL Multiphysics developers. *COMSOL Documentation: Frequency-Stationary*. https://doc.comsol.com/6.0/doc/com.comsol.help.comsol/comsol_ref_solver.32.055.html. 2021.

[47] N. Bowler. "Frequency-Dependence of Relative Permeability in Steel". In: *AIP Conference Proceedings*. QUANTITATIVE NONDESTRUCTIVE EVALUATION. Vol. 820. ISSN: 0094243X. Brunswick, Maine (USA): AIP, 2006, pp. 1269–1276. DOI: 10.1063/1.2184670. URL: https://pubs.aip.org/aip/acp/article/820/1/1269-1276/965515 (visited on 09/04/2024).

[48] LibreTexts Engineering. *10.2: Permeability of Some Common Materials*. 2024. URL: https://eng.libretexts.org/Bookshelves/Electrical_Engineering/Electro-Optics/Book%3A_Electromagnetics_I_(Ellingson)/10%3A_Appendices/10.02%3A_Permeability_of_Some_Common_Materials.